TURUN
YLIOPISTO
UNIVERSITY
OF TURKU

PARTICLE OBSERVATIONS IN NEAR-EARTH SPACE

Design and verification of particle instruments for CubeSat experiments

Philipp Oleynik

TURUN YLIOPISTON JULKAISUJA – ANNALES UNIVERSITATIS TURKUENSIS
SARJA – SER. AI OSA – TOM. 658 | ASTRONOMICA – CHEMICA – PHYSICA – MATHEMATICA | TURKU 2021

TURUN
YLIOPISTO
UNIVERSITY
OF TURKU

PARTICLE OBSERVATIONS IN NEAR-EARTH SPACE

Design and verification of particle instruments for CubeSat experiments

Philipp Oleynik

TURUN YLIOPISTON JULKAISUJA – ANNALES UNIVERSITATIS TURKUENSIS
SARJA – SER. AI OSA – TOM. 658 | ASTRONOMICA – CHEMICA – PHYSICA – MATHEMATICA | TURKU 2021

University of Turku

Faculty of Science
Department of Physics and Astronomy
Physics
Doctoral Programme in Physical and Chemical Sciences

Supervised by

Prof. Rami Vainio
University of Turku
Turku, Finland

Dr. Juhani Peltonen
University of Turku
Turku, Finland

Reviewed by

Dr. Petteri Nieminen
European Space Agency
Noordwijk, Netherlands

Prof. Dr. Viviane Pierrard
Royal Belgian Institute
for Space Aeronomy
Brussels, Belgium

Opponent

Prof. Catia Grimani
University of Urbino ”Carlo Bo”, Italy

The originality of this publication has been checked in accordance with the University of Turku quality assurance system using the Turnitin OriginalityCheck service.

ISBN 978-951-29-8704-7 (PRINT)
ISBN 978-951-29-8705-4 (PDF)
ISSN 0082-7002 (PRINT)
ISSN 2343-3175 (ONLINE)
Painosalama, Turku, Finland, 2021

UNIVERSITY OF TURKU
Faculty of Science
Department of Physics and Astronomy
Physics
OLEYNIK PHILIPP: Particle Observations in Near-Earth Space
Doctoral dissertation, 137 pp.
Doctoral Programme in Physical and Chemical Sciences
November 2021

ABSTRACT

This doctoral thesis presents the design, simulation, and calibration of two instruments developed to study energetic charged particles in low-Earth orbit. The near-Earth energetic charged particle populations include particles trapped by the Earth magnetic field, solar energetic particles, and galactic cosmic rays. Each population has its spatial distribution, energy spectra, and temporal dynamics that reflect the physical processes connected with the particle injection, acceleration, or removal.

The instruments discussed in the thesis aim to study the most abundant and dynamic particle population, i.e., electrons and protons in the Van Allen radiation belts. In addition, with one of the instruments we endeavour to detect energetic neutral atoms originating in the solar corona. Solar energetic neutral atoms carry direct information on particle acceleration mechanisms occurring in the solar corona, which are challenging to analyse using in-situ observations of charged particles.

The first instrument described in this work is RADMON, a miniature radiation monitor onboard the first Finnish CubeSat Aalto-1. We have simulated the instrument and re-calibrated it using data obtained in space. We present the response functions for each instrument channel. We discuss the issues of contamination of electron channels of the instrument by high-energy protons. We use the response functions to convert instrument counts to physical units and present the data obtained by RADMON in 2017-2019.

The second instrument described in the doctoral thesis is PATE, a particle telescope that is a part of the payload of the Finnish CubeSat mission Foresail-1, scheduled to be delivered for launch in 2021. We have simulated the instrument under development and verified its design by using a precise simulation model. We present the instrument construction, particle classifier rules, and instrument response functions.

An essential part of the work presented in the thesis is Monte Carlo simulations within the Geant4 framework. We have used Geant4 modelling to study particle detector responses, to calibrate instrumental gains and offsets, and to verify the designs of particle classifiers. We conclude that this simulation framework offers an efficient way of assessing several aspects of charged particle instruments and that such simulations should be an integral part of the design and verification process of charged particle instruments flown in space.

KEYWORDS: particle observation, satellite instrument, CubeSat.

TURUN YLIOPISTO
Matemaattis-luonnontieteellinen tiedekunta
Fysiikan ja tähtitieteen laitos
Fysiikka
OLEYNIK PHILIPP: Particle Observations in Near-Earth Space
Väitöskirja, 137 s.
Fysikaalisten ja kemiallisten tieteiden tohtoriohjelma
Marraskuu 2021

TIIVISTELMÄ

Tämä väitöskirja käsittelee kahden suurienergiaisten varattujen hiukkasten havainnointiin kehitetyn satelliitti-instrumentin suunnittelua, simulointia ja kalibrointia. Maan lähiavaruuden varattujen hiukkasten populaatiot ovat Maan magneettikenttään loukkuuntuneita hiukkasia, Auringossa kiihdytettyjä hiukkasia ja galaktista kosmista säteilyä. Jokaisella populaatiolla on oma spatiaalinen jakaumansa, energiaspektri ja ajallinen dynamiikka, jotka kuvastavat hiukkasten injektioon, kiihdytykseen tai häviöihin liittyviä fysikaalisia prosesseja.

Instrumenteilla on tarkoitus tutkia näistä runsainta ja dynaamisinta hiukkaspopulaatiota, eli elektroneja ja protoneja Van Allenin säteilyvöissä. Lisäksi toisella instrumenteista pyritään havaitsemaan Auringon koronasta peräisin olevia suurienergiaisia neutraaleja hiukkasia. Nämä antavat suoraa tietoa Auringon varattujen hiukkasten kiihdytysprosesseista, joita in situ -tutkimuksella on varsin haastava tutkia.

Ensimmäinen tässä työssä kuvattu laite on RADMON, miniatyrisoitu säteilymonitori Aalto-1 -kuutiosatelliitissa, joka on Suomen ensimmäinen oma satelliitti. Olemme simuloineet instrumentin ja kalibroineet sen uudelleen avaruudesta saadun datan avulla. Esittelemme määrittämämme vastefunktiot jokaiselle instrumentin kanavalle. Tarkastelemme laitteen elektronikanavien kontaminaatiota suurienergiaisten protonien vaikutuksesta. Käytämme vastefunktioita instrumentin mittaamien hiukkaslukumäärien muuntamiseen fysikaalisiin vuoyksiköihin ja esittelemme RADMON:in 2017-2019 tekemät mittaukset.

Toinen väitöskirjassa kuvattu instrumentti on PATE-hiukkasteleskooppi, joka on osa suomalaisen Foresail-1 -kuutiosatelliitin hyötykuormaa. Satelliitti on tarkoitus luovuttaa laukaisijalle vuonna 2021. Olemme simuloineet kehitteillä olevaa instrumenttia ja verifioineet sen suunnittelun käyttämällä tarkkaa simulaatiomallia. Esittelemme laitteen rakenteen, hiukkasten luokittelusäännöt, ja laitteen vastefunktiot.

Olennainen osa väitöskirjassa esitettyä työtä ovat Monte Carlo -simulaatiot Geant4-ohjelmistolla. Olemme käyttäneet Geant4-mallinnusta hiukkasilmaisinten vastefunktioiden tutkimiseen, instrumenttien vahvistinparametrien kalibrointiin ja hiukkasluokittelijoiden suunnittelun verifiointiin. Johtopäätöksemme on, että tämä simulaatio-ohjelmisto tarjoaa tehokkaan tavan arvioida hiukkasinstrumenttien ominaisuuksia ja että tällaisten simulaatioiden tulisi olla erottamaton osa satelliittihankkeiden hiukkasinstrumenttien suunnittelu- ja verifiointiprosessia.

ASIASANAT: hiukkasten havainnointi, satelliitti-instrumentti, kuutiosatelliitti.

Acknowledgements

This research has started in the spring of 2018 at the University of Turku. At the same time, I started to work as a project researcher for the Finnish center of excellence in research of sustainable space FORESAIL.

The reported results were obtained during 2018 – 2020 at the Space Research Laboratory of the University of Turku. The first part of the reported research was to calibrate RADMON, a tiny radiation monitor onboard Aalto-1, the first Finnish research satellite. The second part of the research was to assess the performance of PATE, a future particle telescope.

First, I wish to express my sincere gratitude to my supervisors, Prof. Rami Vainio and Dr. Juhani Peltonen. I am grateful to Rami Vainio for the patience in looking for a mistake, continued encouragement, precise guidance, and time. It is a great moment to thank Juhani Peltonen for his supervision on the practical aspects since engineering questions are less highlighted in the publications. No space instrument worked without well-designed electronics, and the PATE particle telescope is not an exception.

Second, I thank Eino Valtonen for the remarkable documentation on the laboratory equipment that raised my standards. I am glad to thank Timo Eronen, who introduced me to the University clusters, which made the presented simulations possible and encouraged me to teach my peer students to follow my steps. I owe a debt of gratitude to Pasi Virtanen, who provided mechanical models of the instruments. I thank Jaan Praks for organizing inspiring and fruitful meetings, Arttu Punkkinen for the excellent cooperation and lovely photos taken during the experimental work, Hannu-Pekka Hedman and Risto Punkkinen for guiding me when we worked in a clean room, Tero Säntti for showing me an example of pedantic approach in system design, Rizwan Mughal for the tedious work done on the joint articles, and Jani Tammi for great software that aided the development of PATE.

Third, I truly appreciate the efforts made by my teachers at the University, who taught me how to express and present my ideas, which helped me during the preparation of the manuscripts, posters, and presentations for conferences, and grant applications.

Last but not least, I owe an immense deal of gratitude to my family, my wife Viktoria, my parents and her parents as well, who supported me during my studies and findings, cheered me up when something did not work as it should, supported me and kept patience when I needed more time than a usual workday.

Turku, November 2021
Philipp Oleynik

Table of Contents

Abbreviations

3D	3 Dimensional
AAGCM	Altitude-Adjusted Corrected Geomagnetic coordinates
ADC	Analog to Digital Converter
CAD	Computer Aided Design
CERN	Conseil Européen pour la Recherche Nucléaire
CERES	Compact Radiation belt Explorer
CSDA	Continuous Slow-Down Approximation
CSSWE	Colorado Student Space Weather Experiment
CuSP	CubeSat mission to study Solar Particles
DC	Direct Current
ENA	Energetic Neutral Atom
EPT	Energetic Particle Telescope
ESA	European Space Agency
IGRF	International Geomagnetic Reference Field
GCR	Galactic Cosmic Ray
GDML	Geometry Definition Markup Language
GEANT4	GEometry ANd Tracking 4
GUI	Graphical User Interface
LET	Linear Energy Transfer
MEPED	Medium Energy Proton and Electron Detector
MERiT	Miniaturized Electron pRoton Telescope
NASA	National Aeronautics and Space Administration
NOAA	National Oceanic and Atmospheric Administration
DAM	Digital and Absorber Module
PC	Personal Computer
PCB	Printed Circuit Board
POES	Polar-orbiting Operational Environmental Satellite
PROBA	PRoject for OnBoard Autonomy – Vegetation
SAA	South Atlantic Anomaly
SAMPEX	Solar, Anomalous, and Magnetospheric Particle Explorer
SEP	Solar Energetic Particle
SST	Solid State Telescope
STEREO	Solar Terrestrial Relations Observatory

THEMIS	Time History of Events and Macroscale Interactions during Substorms
XML	eXtensible Markup Language

List of Original Publications

This dissertation is based on the following original publications, which are referred to in the text by their Roman numerals:

I Oleynik, P., Vainio, R., Punkkinen, A., Dudnik, O., Gieseler, J., Hedman, H., Hietala, H., Hæggström, E., Niemelä, P., Peltonen, J., Praks, J., Punkkinen, R., Säntti, T., and Valtonen, E. (2020). Calibration of RADMON Radiation Monitor Onboard Aalto-1 CubeSat. *Advances in Space Research*, 66(1):42–51

II Gieseler, J., Oleynik, P., Hietala, H., Vainio, R., Hedman, H.-P., Peltonen, J., Punkkinen, A., Punkkinen, R., Säntti, T., Hæggström, E., Praks, J., Niemelä, P., Riwanto, B., Jovanovic, N., and Mughal, M. R. (2020). Radiation Monitor RADMON aboard Aalto-1 CubeSat: First results. *Advances in Space Research*, 66(1):52–65

III Oleynik, P., Vainio, R., Hedman, H.-P., Punkkinen, A., Punkkinen, R., Salomaa, L., Säntti, T., Tuominen, J., Virtanen, P., Bosser, A., Janhunen, P., Kilpua, E., Palmroth, M., Praks, J., Slavinskis, A., Kakakhel, S. R., Peltonen, J., Plosila, J., Tammi, J., Tenhunen, H., and Westerlund, T. (2020). Particle Telescope aboard FORESAIL-1: simulated performance. *Advances in Space Research*, 66(1):29–41

IV Mughal, M. R., Praks, J., Vainio, R., Janhunen, P., Envall, J., Näsilä, A., Oleynik, P., Niemelä, P., Slavinskis, A., Gieseler, J., Jovanovic, N., Riwanto, B., Toivanen, P., Leppinen, H., Tikka, T., Punkkinen, A., Punkkinen, R., Hedman, H.-P., Lill, J.-O., and Slotte, J. (2021). ”Aalto-1, multi-payload CubeSat: In-orbit results and lessons learned”. *Acta Astronautica*, 187:557–568

Author’s contribution to the Papers

The author has constructed models, carried out Monte Carlo simulations, performed the data analysis, and presented the results in the Papers.

Papers I, II, and III became a part of a special issue of the Advances in Space Research dedicated to scientific experiments carried out on CubeSats.

The author mastered the major part of the writing of Papers I and III and contributed to Paper II in the part that covers instrument properties. The author prepared plots and tables, based on the simulations done by the author, in Papers I and III.

The author calculated the calibration values for the RADMON instrument, applied in Paper II, and used them to prepare a dataset described in Paper II. The author wrote and edited a chapter concerning the lessons learned in RADMON operations for Paper IV.

In the following articles, not included in the thesis, the author wrote and edited sections concerning the instrument design and simulated response, prepared plots and illustrations for the sections:

A. Palmroth, M., Praks, J., Vainio, R., Janhunen, P., Kilpua, E. K. J., Afanasiev, A., Ala-Lahti, M., Alho, A., Asikainen, T., Asvestari, E., Battarbee, M., Binios, A., Bosser, A., Brito, T., Dubart, M., Envall, J., Ganse, U., Ganushkina, N. Y., George, H., Gieseler, J., Good, S., Grandin, M., Haslam, S., Hedman, H.-P., Hietala, H., Jovanovic, N., Kakakhel, S., Kalliokoski, M., Kettunen, V. V., Koskela, T., Lumme, E., Meskanen, M., Morosan, D., Mughal, M. R., Niemelä, P., Nyman, S., Oleynik, P., Osmane, A., Palmerio, E., Peltonen, J., Pfau-Kempf, Y., Plosila, J., Polkko, J., Poluianov, S., Pomoell, J., Price, D., Punkkinen, A., Punkkinen, R., Riwanto, B., Salomaa, L., Slavinskis, A., Säntti, T., Tammi, J., Tenhunen, H., Toivanen, P., Tuominen, J., Turc, L., Valtonen, E., Virtanen, P., and Westerlund, T. (2019). FORESAIL-1 CubeSat Mission to Measure Radiation Belt Losses and Demonstrate Deorbiting. *Journal of Geophysical Research: Space Physics*, 124(7):5783–5799

B. Huovelin, J., Vainio, R., Lehtolainen, A., Kilpua, E., Korpela, S., Esko, E., Muinonen, K., Bunce, E., Martindale, A., Grande, M., Andersson, H., Nenonen, S., Lehti, J., Schmidt, W., Genzer, M., Vihavainen, T., Saari, J., Peltonen, J., Valtonen, E., Talvioja, M., Portin, P., Narendranath, S., Järvinen, R., Okada, T., Milillo, A., Laurenza, M., Heino, E., and Oleynik, P. (2020). Solar Intensity X-Ray and Particle Spectrometer SIXS: Instrument Design and First Results. *Space Science Reviews*, 216(5):1–42

C. Praks, J., Mughal, M. R., Vainio, R., Janhunen, P., Envall, J., Oleynik, P., Näsilä, A., Leppinen, H., Niemelä, P., Slavinskis, A., Gieseler, J., Toivanen, P., Tikka, T., Peltola, T., Bosser, A., Schwarzkopf, G., Jovanovic, N., Riwanto, B., Kestilä, A., Punkkinen, A., Punkkinen, R., Hedman, H.-P., Säntti, T., Lill, J.-O., Slotte, J., Kettunen, H., and Virtanen, A. (2021). Aalto-1, multi-payload cubesat: Design, integration and launch. *Acta Astronautica*, 187:370–383

1 Introduction

> There is no such thing as an invalid measurement. One always gets the correct answer because all systems are constrained by physical laws. As in an electrical circuit, which always operates according to the way it is built even though that may not be what the designer intended, any physical test also provides the correct answer. The problem is that frequently the parameters being measured are not the parameters one thinks are being measured.
>
> ”Measurement techniques in space plasmas” (Vampola, 1998)

Motivation for the Thesis

Space research relies on data gathered by satellites. At the beginning of space exploration, many satellites were relatively small, below 100 kg. The scientific demands on the aperture size and electric power, i.e., solar cells dimensions, pushed the average size of a research satellite in the tonne domain. However, a new turn of technology development enabled scientific instruments to become again small and power-efficient. The CubeSat project introduced a new era in space research. The new standard allowed the creation of miniature, reliable instruments on platforms with a size of a milk jug and costs below 1 million. This recently emerged environment stimulated the development of nanosatellites for space research by universities around the world.

The relaxed requirements on the product assurance and the electronic components for instruments encouraged new research and the same time, reduced the number of documents describing instruments. However, the quality of the scientific data relies on the integrity of the development of an instrument. The work presented in the Thesis aims at presenting the instruments openly, thoroughly, and transparently. The articles that compose the thesis show development, calibration, verification, modeling of instruments, and lessons learned from the Aalto-1 mission.

The influence of the near-Earth environment on modern technological society grows year by year. The dynamics of radiation belts affect the spacecraft fleet that we depend on in many aspects of our life.

Thesis Structure

The Thesis consists of an introductory part and four research articles.

Paper I reports on the in-flight calibration of the radiation monitor RADMON onboard Aalto-1 CubeSat. The instrument is measuring fluxes of charged particles in low Earth polar orbit. Paper II provides an overview of the observational data obtained by RADMON during a period from October 2017 to May 2018. It shows the observed magnetosphere dynamics and discusses data comparison between RADMON and the PROBA-V/EPT mission.

Chapter 2 of the introductory part gives a concise overview of the near-Earth magnetic and radiation environment relevant to the research presented in Papers I-IV. The overview scope supports the scope of the Thesis, which concentrates on particle instruments rather than on the physics of the magnetosphere. The chapter also outlines the space weather and its significance for modern technology.

Paper III introduces the particle telescope PATE designed to explore charged particle populations in low Earth orbit with the ability to observe particles' pitch angle distribution. Chapter 3 supports Papers I–III by introducing necessary particle instrument design and calibration details. Chapter 4 briefly describes Aalto-1/RADMON and Foresail-1/PATE and discusses how a future instrument similar to RADMON could be designed.

Paper IV considers the lessons learned from the Aalto-1 mission after three years in space. RADMON has proven to be one of the most successful payloads on the satellite. Paper IV discusses how a future instrument similar to RADMON could be improved to monitor the charged particle fluxes.

Chapter 5 introduces the method of Geant4 simulations used in Papers I-IV to characterize the instrument response, define the energy channels, and build the RADMON data product.

Finally, Chapter 6 comprises the Papers' summaries, Chapter 7 condenses the Thesis results, and Chapter 8 provides an outlook on the future research.

2 The near-Earth space

2.1 Introduction

On September 1 and 2, 1859, occurred the most intense documented magnetic disturbance in history. It led to widespread failures of telegraph communications. Aurora has been observed not only in polar regions but as southern as Cuba and Hawaii. It was reported to be as bright as one could read a newspaper under the aurora.

In 1896 Kristian Birkeland proposed that cathode rays (i.e., electrons) coming from the Sun, especially from the sunspots, cause magnetic disturbances, and aurora on Earth phenomena are connected. Disturbances in Earth magnetic field were known to hinder navigation and radio communications. The importance of these two supported the importance of research on what causes geomagnetic storms.

Ironically, a governmental ban on amateur operations in frequencies lower than 1.5 MHz led to discovering multiple ionospheric reflections of the radio waves in higher frequencies predicted by Heaviside in 1902. The phenomenon was explained by the presence of ionized layers in the upper atmosphere. Long-distance radio communication gradually gained great importance for society and technology.

At the dawn of the space era in 1957–1958, a series of space probes discovered inner and outer Van Allen radiation belts surrounding the Earth (Van Allen, 1958; Snyder, 1959; Vernov and Chudakov, 1960; Rothwell and McIlwain, 1960). Two trapped particle clouds were discovered, and their dynamics were proven to depend on solar activity. On the verge of the 21st century, the practical significance of understanding the dynamics of the radiation belts rose dramatically in correlation with the number of satellites operating in the Earth orbit. Energetic charged particles can cause satellite malfunctions in space by altering semiconductor devices' properties due to accumulated radiation dose (Claeys and Simoen, 2002), flipping bits in the computer memory, or deep charging dielectric materials to hazardous levels.

The phenomena that connect the dynamics of the radiation belts, the near-Earth space environment, and the interplanetary space, including the Sun, were designated as "space weather" (Baker, 1998). The importance of space weather to our technological society is no less critical than meteorological forecasts fifty years ago. Our dependence on satellite navigation, communication, and remote sensing has immensely grown in the last decades and has the potential to further growth. Therefore, it is crucial to understand the space weather phenomena, which can be done by comprehensive observations, modeling, and analysis.

2.2 Radiation environment

The near-Earth radiation environment consists of Van Allen radiation belts, solar energetic particles (SEP), and galactic cosmic rays (GCR) (Vainio et al., 2009). From the three components, the GCR is the most stable one. The lower energy component of GCRs varies in intensity by an order of magnitude, decreasing with solar activity. The other two, on the contrary, are intensively dynamic.

The GCRs[1] are 90% protons, 8% alpha particles, 1% heavier, fully stripped nuclei, and about 1% electrons (Papini et al., 1996). GCRs have not only ordinary matter but antiprotons and positrons in minor quantities. In the near-Earth space, the peak intensity of GCRs lies in the energy range of 0.1 – 1 GeV/nucleon with an integral flux of about $1\,\mathrm{cm}^{-2}\,\mathrm{s}^{-1}$. The GCRs are generated in supernova remnants by diffusive shock acceleration (Ackermann et al., 2013). The GCRs of energies above 8 EeV are reported to have anisotropy that suggests their extragalactic origin (Aab et al., 2017).

The SEPs are electrons, protons, and heavier nuclei accelerated to high energies above 1 MeV during intensive solar flares and coronal mass ejections (Reames, 1999, 2015). The SEP flux may rise several orders of magnitude in a matter of few hours. The geomagnetic field partially traps energetic solar protons into the inner radiation belt (Selesnick et al., 2007; Li and Hudson, 2019). Some of the energetic protons may experience charge exchange with neutral hydrogen in solar corona and continue their way through the interplanetary space as solar energetic neutral atoms observable at the Earth orbit (Mewaldt et al., 2009).

The Van Allen radiation belts can be pictured as two large toroidal structures surrounding Earth. Figure 1 shows the cross-section of the radiation belts. The inner belt lies at geocentric distances of 1 – 3 Earth radii in the equatorial plane. The outer belt starts right after a small depletion region around the inner belt and extends up to 7 – 8 Earth radii. The radiation belts are formed by charged particle populations trapped by the Earth magnetic field. Their shapes are aligned with the Earth magnetic dipole axis, which is tilted about 10 degrees from the polar axis. Multiple interconnected phenomena compete to enrich, accelerate, or deplete the radiation belts, making them a unique natural laboratory (Ripoll et al., 2020).

2.2.1 Radiation belts

The inner belt that is closer to the Earth is mostly proton-dominated, with a small portion of heavier ions. The observed proton energies range from several MeV up to hundreds of MeV. The proton energy distribution is argued to have a tail reaching the the trapping limit of 3–4 GeV (Selesnick et al., 2007). Most of the high-energy protons originate from cosmic ray albedo neutron decay (Singer, 1958), but the confined

[1] At the Earth orbit.

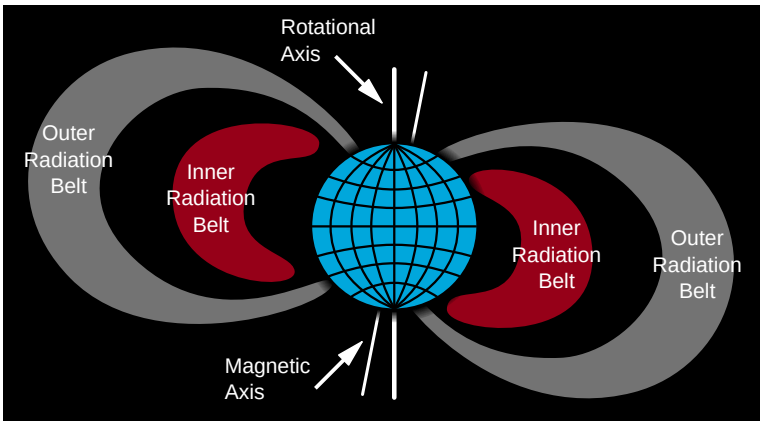

Figure 1. Structure of the radiation belts. Image credit Chris Martin, public domain image.

population of energetic solar protons dominates in the energy range below 100 MeV. Solar energetic protons get trapped in the polar regions into the belt (Selesnick et al., 2007). The inner proton belt is highly stable on the time scale of a year (Selesnick and Albert, 2019).

One of the prominent features of the inner belt is the South Atlantic Anomaly (SAA) discovered shortly after the discovery of radiation belts (Kurnosova et al., 1962). The behavior of the anomaly is significant for near-Earth satellites due to extreme fluxes of energetic protons able to disrupt the functioning of satellites' electronic equipment. SAA is caused by the shift of the Earth magnetic dipole to the side from the rotation axis. The inner belt sustained by the magnetic field falls asymmetric relative to the Earth surface, approaching altitudes about 400 km above the South Atlantic region. The region affected by energetic particles drifts slowly westwards, driven by the changes in the Earth magnetic field (Anderson et al., 2018).

In addition to the stable proton population, the inner belt has a minor but very dynamic electron population. It has been questioned whether particle instruments observe high energy protons or energetic electrons in SAA, but Selesnick (2015) shows convincing evidence that electrons are injected into the inner belt in short events. The electron lifetime in the inner belt, as observed by SAMPEX, is several years.

The outer belt is electron-rich, separated from the inner belt by the particle-depleted slot region. It is a highly dynamic region filled with electrons of energies up to several MeV. The electrons are injected and lost at time scales from minutes to days and months. The dynamic behavior is driven by solar activity, but the link is not straightforward. The response of the outer belt electrons to geomagnetic storms induced by solar activity may be enrichment, depletion, or sustaining (Reeves et al., 2003). Figure 2 shows intensive dynamics of the outer belt electrons observed by Van Allen Probes mission in 2012–2016. The variety of the processes influencing

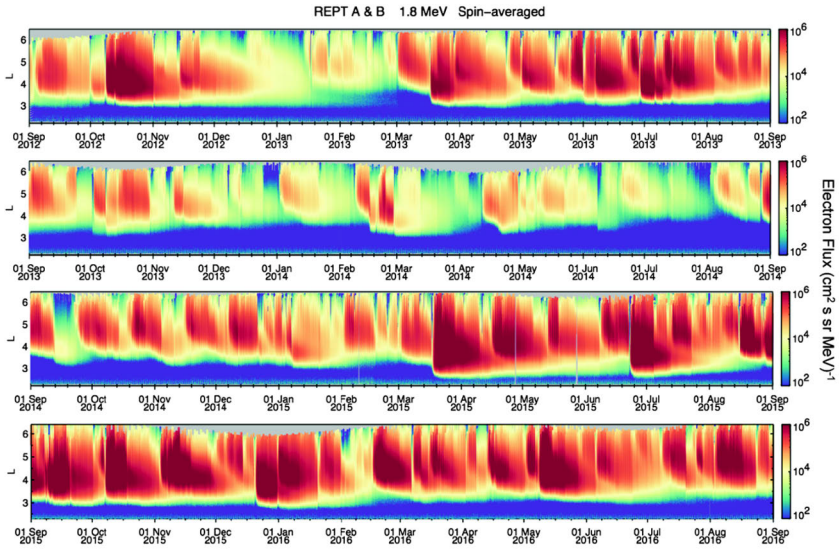

Figure 2. Relativistic Electron-Proton Telescope (REPT) observations of the outer belt relativistic electrons of energies about 1.8 MeV in Sep 2012 – Sep 2016. During powerful storms, the electron belt sinks quite deeply into the $L < 3$. Both sudden enrichment and depletion events are seen in the time history. Image credit (Baker et al., 2018)

the outer belt is wide, including those yet unknown (Kanekal et al., 2019; Li and Hudson, 2019).

One of the essential loss mechanisms for outer belt electrons is their precipitation to the atmosphere at high latitudes. An electron with its momentum direction inside the loss cone (close to the magnetic field direction) does not reflect from the polar magnetic mirror until it reaches the upper atmosphere, which is dense enough to absorb it. The electron precipitation depletes the outer radiation belt of energetic electrons and also causes a change in the chemistry of NO_x, HO_x and ozone in the upper atmospheric layers (Seppälä et al., 2015). It is argued that the change in the chemistry caused by large-scale geomagnetic storms can affect the neutral winds in the upper atmosphere (Weimer et al., 2011; Borovsky and Valdivia, 2018). The absorption of energetic ionizing electrons induces the pulsating aurora phenomenon (Turunen et al., 2016). One of the key questions in the science of radiation belts is to clarify how electrons get accelerated to relativistic energies, how they are transported within the radiation belt, how they are eventually lost, and how their precipitation affects the magnetosphere and the atmosphere (Borovsky and Valdivia, 2018). To answer this question, we have to observe the electron population in a wide energy range tens of keV to several MeV with an instrument able to deliver pitch-angle resolved measurements.

2.2.2 Magnetic coordinates

The Earth magnetic field can be represented as a primary dipole, tilted 10° to the axis of rotation of the planet, with multiple additional components. The surface field magnitude varies in the range of 30 – 60 μT being stronger near the poles. Thus, the Earth magnetic field constitutes a magnetic trap with magnetic mirrors at poles.

The primary dipole axis drifts inside the Earth, causing magnetic poles to migrate on the surface by several kilometers per month. The current International Geomagnetic Reference Field (IGRF) model has 13 spherical harmonics that describe the Earth magnetic field in its complexity (Thébault et al., 2015).

L-shell coordinate system. McIlwain (1961) proposed a coordinate system that would adequately describe positions in the near-Earth space to study the radiation belts. Assuming the Alfven invariant to be constant, in the absence of electric field, and with $\partial B/\partial t$ being small[2], one can define a coordinate via second (longitudinal) invariant J_2 as

$$I \equiv \frac{J_2}{2p} = \frac{\oint_A^{A'} p_{\parallel}\, ds}{2p} = \oint_A^{A'} \sqrt{1 - p_{\perp}^2/p^2}\, ds = \oint_A^{A'} \sqrt{1 - B_l/B}\, ds\,, \qquad (1)$$

where I is the magnetic coordinate, ds is the differential length of the guiding center path between points A and A', which are conjugate points of the magnetic field line, B is the magnitude of the magnetic field at A, B_l is the magnitude of the magnetic field along the field line, $p_{\parallel}$ and $p_{\perp}$ are the momentum components parallel and perpendicular to the magnetic field. The closed contour integration goes along the guiding center path from A to A' and back.

A given pair of I and B defines two rings in the opposite hemispheres. A particle that mirrors at the point A will travel along the magnetic field line to the A' and back between those rings, forming a shell. McIlwain (1961) defines the magnetic shell coordinate $L^3B/M = F(I^3B/M)$ via an empirical function F representing the complex shape of the Earth magnetic field and the Earth dipole moment M. In dipole approximation, L is the distance in Earth radii from the Earth center to the place where the shell crosses the Earth-centered magnetic equatorial plane. The distance of a shell from the Earth dipole quantifies the magnetic trap characteristics for a particle in the shell. Therefore, the L shell parameter is used to spatially identify a particle population trapped between the magnetic mirrors.

A satellite in a circular polar orbit crosses a wide range of L-shells. The field lines crossing the equatorial plane at several Earth radii close at the poles almost vertically. Thus, a satellite in a low-Earth polar orbit crosses L-shells with the L parameter much higher than the orbital altitude measured in the Earth radii.

Altitude-Adjusted Corrected Geomagnetic coordinates (AACGM, Shepherd (2014)) serve a similar purpose of adequate spatial navigation in the Earth mag-

[2] so that the total momentum is conserved

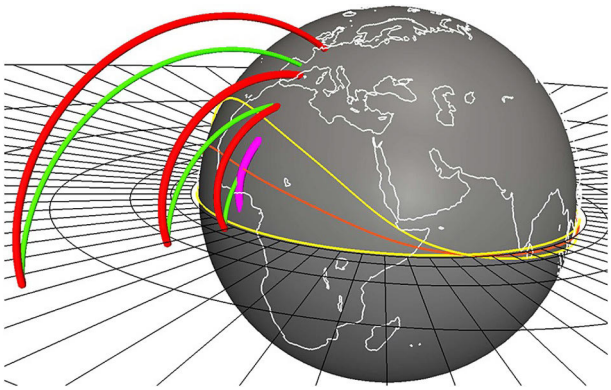

Figure 3. An example of calculating the AACGM coordinates. Red lines are the IGRF magnetic field lines, and green lines are the dipole model field. The magenta line shows the IGRF field line closing before touching the magnetic equator. By definition, there is no AACGM coordinate available for such regions. AACGM never reaches regions close to the magnetic dip equator (thin orange line), marked with thin yellow lines. With permission from American Geophysical Union, adopted from (Shepherd, 2014).

netic field. Their definition relies on tracing the magnetic field lines using the IGRF model. From the mathematical point of view, the coordinates of a point in $\mathcal{R}^3$ are projected to sphere $\mathcal{S}^2$ losing one degree of freedom. Thus, two points in space can have identical AACGM coordinates, which means that the locations of these points are on the same magnetic field line. Particles that bounce along the field line will be observed in both points unless some particles mirror halfway due to their pitch-angle. These two points likely share the particle population confined in the magnetic trap of Earth dipole.

For an arbitrary position A in space, the AACGM coordinates are the latitude λ_m, longitude ϕ_m of the point on the surface, which is connected with A by a dipole magnetic field line. The Figure 3 explains the concept of AACGM. To obtain AACGM coordinates for a point on the surface, one must trace the IGRF magnetic field line emanating from the geographical location to the magnetic equator. A dipole field line is then traced from the point where the IGRF field crosses the magnetic equatorial plane to the Earth surface. The latitude and the longitude of that point are the AACGM coordinates (λ_m , ϕ_m). λ_m is connected to the L-shell coordinate as

$$\cos \lambda_m = 1/\sqrt{L} \tag{2}$$

For a point in near-Earth space, a touching IGRF magnetic field line is traced to the magnetic equator the same way as for a surface point. Thus, the ”forbidden zone” around the equator, where magnetic field lines close at lower altitudes, is wider for a higher orbit.

2.2.3 Solar energetic neutral atoms

Large gradual solar energetic particle events produce high fluxes of protons at energies above tens MeVs, dangerous to crewed and robotic missions alike. The SEPs are accelerated at shock waves of coronal mass ejections during powerful solar eruptions (Reames, 1999). Details of the acceleration mechanism depend on the presence of supra-thermal ions in the solar corona (Desai and Giacalone, 2016). Turbulent coronal magnetic fields can confine these ions; therefore, it is challenging to observe them directly. The solar corona is not fully ionized, so that the supra-thermal ions can be converted to neutral atoms by the charge-exchange process. The neutral energetic atoms can escape the coronal region unaffected by the magnetic field.

There is an observation of energetic (few MeV) neutral atoms from a powerful X9 solar eruption on 5 Dec 2006 by STEREO mission(Mewaldt et al., 2009). The neutral atoms of high energy are proxies of the original supra-thermal population of ions in the solar corona. These ions significantly influence how effectively particles can be accelerated by the shock waves created by coronal mass ejections.

A neutral atom would travel in the same direction as the initial ion without being deflected by electromagnetic fields in the interplanetary space. These neutrals would be observable at the Earth orbit as a flux of energetic particles coming directly from the Sun.

2.2.4 Space weather

The term ”space weather” coined by Baker (1998) comprises phenomena influencing the dynamical near-Earth environment, which in turn affects many aspects of modern technology and society in general (Lanzerotti, 2017; Baker et al., 2018). The term encompasses the processes and states of the geospace environment, the interplanetary space, and the Sun. Space weather is known to be rapidly changing, which drives the efforts to predict it the same way as we predict the weather on the ground.

The radiation belts are affected by the space weather the most, and at the same time, are the main environmental factor influencing the performance and reliability of spacecraft and ground-based equipment.

3 Particle detection

The first particle detector in space was a Geiger-Muller counter onboard the Explorer 1 mission launched in 1958. The counter was sensitive to protons with energies >30 MeV and electrons with energies >3 MeV. Despite being simple, the instrument allowed us to discover the radiation belts of the Earth.

A particle instrument detects a charged particle by measuring how physical properties of its sensitive units, or detectors, change upon interaction with an incident particle. The interaction concludes within nanoseconds, resulting in a trigger in the logic of the instrument. The logic further compares the signals from detectors to produce a count. The total number of counts within a time unit comprise the count rate of an instrument.

This chapter introduces the particle detection techniques used in the presented Thesis; the topic is expounded by Papers I, III, and IV.

3.1 Introduction

One of the scientific objectives for a particle instrument is to acquire the particle distribution function in the 6D phase space.

$$f(x,p) = \frac{\mathrm{d}^6 N}{\mathrm{d}^3 x \, \mathrm{d}^3 p} \tag{3}$$

The knowledge of the distribution function moderates the development of hypotheses on particle transport and acceleration. These hypotheses eventually mature into theories and models that help us understand and predict the behavior particle populations in space.

The full distribution function is hard to recover, but it is possible to describe it in a particular part of the phase space using an instrument sensitive to particle energies and incident angles and temporal flux variations. Using the count rates of particle detectors, we can restore the distribution function of the particles.

Let us assume a particle instrument that observes the flux, a function of time, energy, and solid angle.

$$\frac{\mathrm{d}I}{\mathrm{d}E} = \frac{\mathrm{d}N}{\mathrm{d}A \, \mathrm{d}\Omega \, \mathrm{d}t \, \mathrm{d}E} \tag{4}$$

For a non-relativistic case $\mathrm{d}E = mv\,\mathrm{d}v = p\,\mathrm{d}v = v\,\mathrm{d}p$. For a relativistic particle, the following is still true:

$$\mathrm{d}E = v\,\mathrm{d}p. \tag{5}$$

Let us apply it for $\mathrm{d}E$ in (4) and note that $\mathrm{d}A\,v\,\mathrm{d}t = \mathrm{d}^3x$:

$$\frac{\mathrm{d}I}{\mathrm{d}E} = \frac{\mathrm{d}N}{\mathrm{d}A\,\mathrm{d}\Omega\,\mathrm{d}t\,v\,\mathrm{d}p} = \frac{\mathrm{d}N}{\mathrm{d}^3x\,\mathrm{d}\Omega\,\mathrm{d}p} \tag{6}$$

We can substitute $\mathrm{d}^3p = p^2\,\mathrm{d}\Omega\,\mathrm{d}p$, therefore:

$$\frac{\mathrm{d}I}{\mathrm{d}E} = p^2\frac{\mathrm{d}^6N}{\mathrm{d}^3x\,\mathrm{d}^3p} = p^2 f(x,p) \tag{7}$$

Therefore the task was reduced to obtaining the incident flux I by measurements. However, a particle telescope reads out its sensors and reports the number of valid counts per time unit, or the count rate. To recover I, we must know the dependence of the count rate on the incident flux in a specific energy range.

Geometric factor $G\,[\mathrm{cm}^2\mathrm{sr}]$ of an instrument is a linear factor that links the count rate $C\,[\mathrm{s}^{-1}]$ of an instrument to the incident particle flux $I_0\,[\mathrm{cm}^{-2}\mathrm{sr}^{-1}\mathrm{s}^{-1}]$ (Sullivan, 1971):

$$C = I_0\,G \tag{8}$$

An ideal single planar detector, exposed to the isotropic incident flux, has a geometric factor of πA, where A is its surface area. Despite the complexity of a real instrument, the geometric factor notion enables a straightforward conversion of the count rates observed by the instrument into physical flux units. The concept of the geometric factor can be generalized as the response function of an instrument to account for the properties of a realistic instrument that depend on the incident particle energy, incident angle, particle species, as well as temperature or instrument age. The equation then expresses the count rate:

$$C = \sum_{k=1}^{N}\int_E\int_\Omega f_k(E,\Omega)\,\Psi_k(E,\Omega)\,\mathrm{d}E\,\mathrm{d}\Omega\,, \tag{9}$$

where f_k is the differential particle flux of k-th species, $\Psi_k(E,\Omega)$ is the instrument response to particles of k-th species, E is the incident particle energy, and Ω is the solid angle of particle incidence. Equation (9) becomes (8) when the incident flux is isotropic, monoenergetic and consists of only one particle species.

If an instrument has multiple counter channels, the response function is defined for each of them so the count rate is:

$$C_i = \sum_{k=1}^{N}\int_E\int_\Omega f_k(E,\Omega)\,\Psi_{ik}(E,\Omega)\,\mathrm{d}E\,\mathrm{d}\Omega\,, \tag{10}$$

where C_i is the count rate of the i-th particle channel, and the response function $\Psi_{ik}(E, \Omega)$ has two indices for channel and particle species. The response function depending on the incident energy, angle, and particle species comprehensively describes a particle instrument. The simulations and calibration of particle instruments described in Paper I and Paper III aim to characterize instruments by obtaining their response functions.

3.2 Detectors

The development of elementary particle and solid-state physics brought multiple different types of physical devices that are capable of converting energy deposited in the detector medium to another form that is accessible to electronics, and finally, to researchers. Charged particles ionize the solid-state bulk of a detector, producing either an electrical signal, or accumulative change in electrical properties, or an optical flash.

A particle instrument consists of one or more detectors paired with readout electronics. The analog signals formed by the readout subsystems are digitized by analog-to-digital converters (ADC) and continue their way in the digital domain to particle classifiers and counters. A particle classifier is essentially an algorithm that compares digital values from the ADCs to built-in thresholds, applies coincidence conditions, calculates the deposited energy in digital units, and decides which particle counter it needs to increment if any.

The instruments described in Paper I and Paper III utilize solid-state detectors. RADMON comprises a silicon semiconductor detector and a CsI(Tl) scintillator coupled to a silicon photodiode. PATE utilizes a stack of planar silicon detectors arranged in several neighboring planar segments and five parallel layers.

3.2.1 Detection technique

A single detector registers an incident particle if it has caused a detectable interaction with the sensitive volume of the detector. The energy deposit can be analyzed as well; however, a single detector does not discriminate between particle species. A combination of two or more detectors delivers more comprehensive information on an incident particle. The combination is advantageous if the physics processes in the detector stack are not entirely identical. Each particle species has a specific profile of linear energy transfer inside the detector medium. Protons generally deposit more energy per unit length (or thickness, if we consider a layered structure) than electrons. The difference between detectors in respective deposited energies is a reliable proxy of the particle species and energy.

Mass stopping power is the measure of the energy deposited by a particle in the material that causes ionization. It shows how much energy is transferred from an

incident particle and absorbed by the unit of density of the medium per unit length of the particle path. Charged particles lose their energy in the medium by ionization and excitation of atoms; this quantity is essential in choosing the right detectors for the instrument design.

For protons and heavier nuclei, the mass stopping power is described by the Bethe-Bloch equation (Jackson, 1998).

$$-\frac{\mathrm{d}E}{\mathrm{d}x} = Kz^2\frac{Z}{A}\frac{1}{\beta^2}\left[\frac{1}{2}\ln\left[\frac{2m_ec^2\beta^2\gamma^2E_{\max}}{I^2}\right] - \beta^2 - \frac{\delta}{2} - \frac{\phi}{Z}\right], \qquad (11)$$

where $I \approx 16\,Z^{0.9}$ eV is the mean excitation energy of atoms in the material[1], Z, A is the atomic number and the atomic mass of material, z is the charge of the incident particle, $\beta = v/c$, $\gamma = 1/\sqrt{1-\beta^2}$,

$$K = N_A\frac{4\pi e^4}{c^2m_e} \approx 0.307\,\mathrm{MeVcm}^2/\mathrm{g}\,,$$

and

$$E_{\max} = \frac{2m_ec^2\beta^2\gamma^2}{1 + 2\gamma m_e/M + (m_e/M)^2}$$

is the maximum kinetic energy obtained by an electron from an interaction with a particle of mass M. ϕ/Z is the shell correction that corrects (11) for the simplifying assumption that shell electrons are at rest state. The shell correction affects non-relativistic particles, e.g., protons of energies $E/Z < 10$ MeV. δ is the density correction for polarization effects in the medium important for protons above 100 MeV.

$-\mathrm{d}E/\mathrm{d}x$ is independent on the density of material and has a dimension of $[\mathrm{MeVcm}^2/\mathrm{g}]$. To obtain the spatial rate of the energy deposit in $[\mathrm{MeVcm}^{-1}]$, one should scale $-\mathrm{d}E/\mathrm{d}x$ by the material density[2] ρ $[\mathrm{g}/\mathrm{cm}^3]$.

$$\frac{\mathrm{d}\epsilon}{\mathrm{d}(\rho l)} = -\frac{\mathrm{d}E}{\mathrm{d}x}\,, \qquad (12)$$

where l is the distance traveled by the particle.

If a material is a mixture of different atoms, e.g., a plastic or an oxide, it may be considered as made up of thin layers of the compound elements according to their proportion. The stopping power can be treated as being additive, with exemptions for tightly bound molecules (Seltzer and Berger, 1982).

$$\frac{\mathrm{d}E}{\mathrm{d}x} = \sum w_j\left.\frac{\mathrm{d}E}{\mathrm{d}x}\right|_j, \qquad (13)$$

[1] Not to be confused with the ionization energy, which is much lower.

[2] In engineering, it is often called linear energy transfer (LET) or specific energy loss.

where $\mathrm{d}E/\mathrm{d}x|_j$ is the mean stopping power in the j-th element, and w_j is the element proportion.

A property significant for medium energy particle detectors is that the stopping power of a proton $-\mathrm{d}E/\mathrm{d}x \sim 1/\beta^2$, for $\gamma\beta < 3$. The stopping power rises as the particle decelerates in the medium. LET vs. distance in material exhibits a sharp peak near the full stop, called the Bragg peak. At lowest particle speeds[3], i.e. $\gamma\beta < 0.05$, equation (11) is no longer precise (Berger et al., 1993) and phenomenological models or experimental data should be used to account for low energy processes.

One can integrate the equation (11) to obtain the range travelled by a particle before it stops. The range R has the units of $[\mathrm{g\,cm^{-1}}]$ and should be scaled by the density of the material to obtain the path length.

$$R(E_0) = \int_{E_0}^{0} \left[\frac{\mathrm{d}E}{\mathrm{d}x}\right]^{-1} \mathrm{d}E\,, \tag{14}$$

where $R(E_0)$ is the particle range in so-called Continuous Slow-Down Approximation (CSDA). The CSDA range approximation assumes that a particle path is straight, which is moderately precise for protons and heavier particles. Since the $-\mathrm{d}E/\mathrm{d}x \sim \beta^{-2}$ the range is expected to be proportional to the energy squared $R \sim E^2$. Despite being a rough guess, it is close to the widely accepted Bragg-Kleeman rule of $R = R_0 E^\gamma$, where $\gamma \approx 1.7$. In Paper I, we discuss and apply an approximation by Attix (1987) that is even more accurate but still simple.

Each interaction with an electron deflects the incident particle a little. Therefore, the energy deposit is a statistical process with a certain countable number of collisions. The effect of statistical uncertainty of the energy loss per unit length due to the discrete nature of particle interactions is called straggling. The deposited energy is split into a series of discrete amounts, each statistically distributed around the most probable value given by (11). To account for straggling, a "projected range" is available (Berger, 1992). A Monte Carlo simulation of the sequence of particle collisions within matter is intrinsically accurate as well.

The equation (11) is valid for particles with a mass much larger than the mass of an electron. Hence, a significant update is required for the calculations of energy loss by an electron. The incident electron and an electron in the medium are of the same mass. Therefore, the energy loss due to collisions is:

$$-\left.\frac{\mathrm{d}E}{\mathrm{d}x}\right|_{\text{collision}} = K\frac{Z}{A}\frac{1}{\beta^2}\left[\ln\left[\frac{m_e c^2\beta^2\gamma^2(E/2)}{2I^2}\right] + \mathcal{F}(\beta) - \frac{\delta}{2} - \frac{\phi}{Z}\right], \tag{15}$$

where $\mathcal{F}(\beta)$ is a relativistic correction close to $1-\beta^2$.

[3] About 1 MeV for a proton.

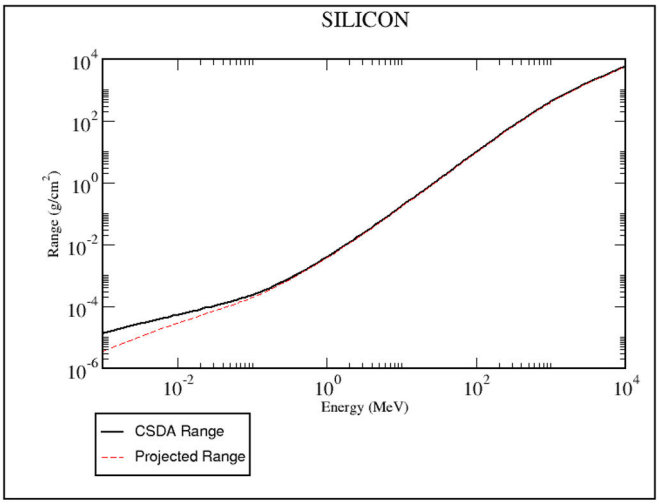

Figure 4. CSDA range and projected range for protons in silicon. Plots are produced by the PSTAR software (Berger, 1992).

Moreover, for relativistic electrons, a prevailing portion of the energy is lost to bremsstrahlung when an electron is decelerating in the Coulomb field of a nucleus. The process dominates at energies of an incident electron above 10 MeV.

$$-\frac{\mathrm{d}E}{\mathrm{d}x}\bigg|_{\text{Bremsstrahlung}} = 4\alpha N_A \frac{Z^2}{A} r_e^2 E \ln\frac{183}{Z^{1/3}} = \frac{E}{X_0}\,, \tag{16}$$

where α is the fine structure constant, and X_0

$$X_0 = \frac{A}{4\alpha N_A Z^2 r_e^2 \ln\frac{183}{Z^{1/3}}} \tag{17}$$

is the radiation length, the average distance in the material reducing the energy of an electron by a factor of e. Therefore, the energy of a relativistic electron decreases exponentially with distance $E(x) = E_0 e^{-x/X_0}$.

The total linear energy transfer is a sum of collision and bremsstrahlung losses plus a minor (several percent in the peak) addition from Møller scattering, which is negligible outside 1...3 MeV energy range.

$$\frac{\mathrm{d}E}{\mathrm{d}x} = \frac{\mathrm{d}E}{\mathrm{d}x}\bigg|_{\text{Bremsstrahlung}} + \frac{\mathrm{d}E}{\mathrm{d}x}\bigg|_{\text{collision}} + \frac{\mathrm{d}E}{\mathrm{d}x}\bigg|_{\text{Møller}} \tag{18}$$

The experimental data (Berger, 1992) presented in Figure 5 shows the transition from collision losses dominating at energies below 1 MeV to bremsstrahlung losses at energies above 10 MeV.

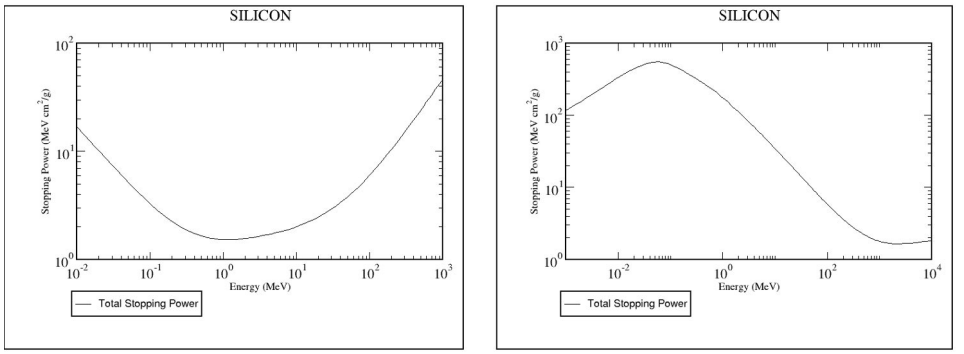

Figure 5. Stopping power vs. energy for electrons (left) and protons (right) in silicon. Plots are produced by ESTAR and PSTAR software (Berger, 1992).

Electrons also experience straggling due to multiple interactions with the electrons and nuclei in the matter. Since the electron mass is either equal or much less than the masses of particles in matter interacting with the electron, the scattering angles reach π. The path of an electron in a dense medium is by no means a straight or slightly curved line. Electron straggling puts limitations on using range tables for the instrument design, warranting a Monte Carlo simulation to be implemented.

3.2.2 Silicon detectors

A silicon particle detector is a semiconductor device that converts energy deposited by an incoming particle into an electric current. Electrically, a silicon detector is a p-n-junction with a reverse bias applied to the terminals on the sides of a silicon disc, plate, or another flat shape (Leroy and Rancoita, 2012). Detector structures are usually manufactured on a bigger wafer, and then the detector is sawed to the size. The detector terminals are usually thin aluminum layers deposited on top of a thin p^+- or n^+-interface doped on the surface of the silicon plate. There could be one or more guard rings around the sensitive area of a silicon detector. The guard rings are also diodes with one of the terminals common to the entire detector. The guard rings, if reversely biased, drain the leakage current caused by non-uniformities on the edges of a silicon plate. Figure 6 shows a schematic cross-section of a silicon detector with a guard ring connected to an electrode and two passive guard rings.

Reverse bias has potential high enough to deplete charge carriers from both the junction region and the detector bulk. A fully depleted p-n-junction is very similar to a capacitor with silicon as dielectric (its dielectric constant $\epsilon = 11.7 \pm 0.2$). The capacitance of the RADMON[4] $2.1 \times 2.1 \times 0.35\,\mathrm{mm}^3$ detector shown in Figure 7 is about 1.7 pF (Peltonen et al., 2014).

[4]The instrument description is in Section Aalto-1/RADMON.

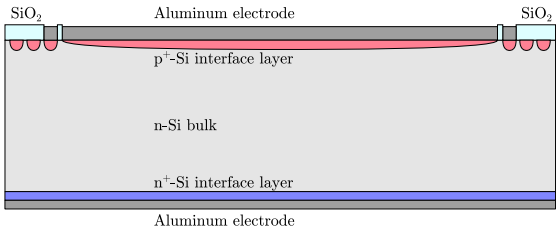

Figure 6. A cross-section of a silicon detector with a guard ring. Interface layers p^+ and n^+ have enhanced carrier density. Silicon oxide passivation protects the detector from environment and insulates the electrodes.

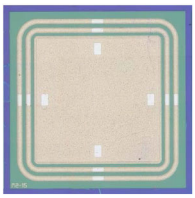

Figure 7. RADMON silicon detector with two guard rings. The inner ring is biased. The outer ring is left floating. (Peltonen et al., 2014)

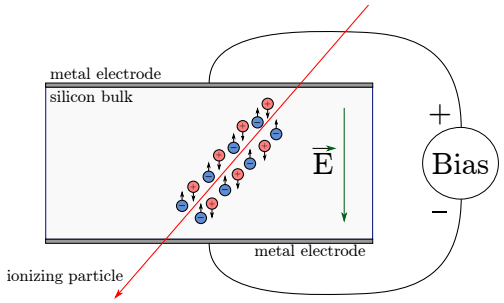

Figure 8. A silicon detector, an ionizing particle hit and the movement of created electron-hole pairs.

When a particle hits the depleted region, it generates multiple electron-hole pairs in sub-nanosecond time. The electric field existing in the depleted region pulls electrons and holes apart until they are collected as a current spike on the terminals, see Figure 8. The drift time might be substantially longer, especially for detectors thicker than several hundred microns. The current is usually read out on the terminal under positive potential since electrons have larger mobility than holes. A 300 µm thick detector produces a current spike of about ten nanoseconds for electrons (Frass, 2009).

The average energy of electron-hole pair creation in silicon is 3.62 eV at room temperature, whereas the bandgap is 1.12 V (Owens and Peacock, 2004). The difference is that silicon is an indirect semiconductor with a maximum of the valence band and minimum conduction band occurring at different crystal momenta (Prinzie et al., 2018). Unlike optical photons with energies below 3.62 eV, which can travel hundreds of microns in silicon without being absorbed until a proper phonon assists photoionization, a charged particle interacts with electrons and nuclei without delay, producing phonons on its way. Therefore, each 1 MeV of energy deposited in silicon ionization yields about $2.72 \cdot 10^5$ electron-hole pairs (Frass, 2009).

A silicon detector may have several active areas sharing a common substrate

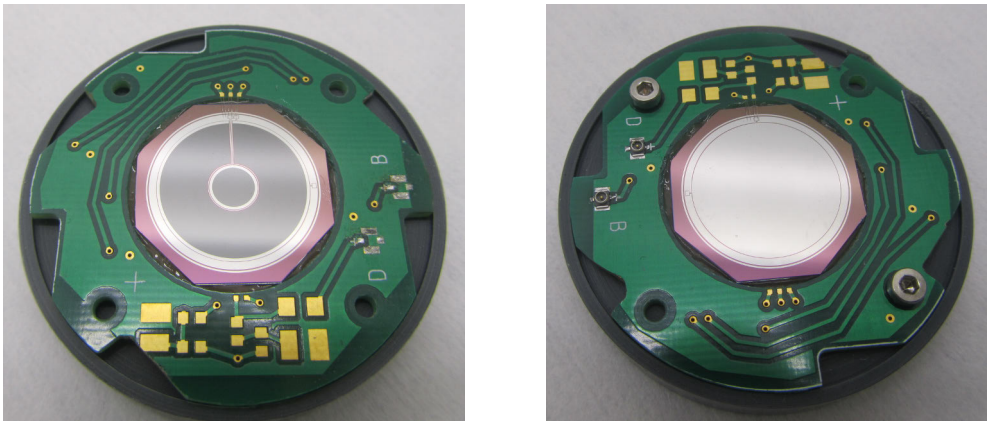

Figure 9. PATE detectors D2 (left) and D3 (right). Segments of D2 and guard rings of both detectors are visible on the surface. Photo credit: Risto Punkkinen.

but with their other terminals isolated from each other. One can use multiple active areas to enable spatial sensitivity or make the active area electronically adjustable on a single silicon layer. Neighboring active areas influence each other as nearby capacitors. Besides, the edge of the crystal is prone to excess leakage current due to cutting defects. The irregularity of the edge leakage current might translate into extra noise of the detector. Each silicon detector plate can have several guard rings between the p-n-junction(s) used for particle detection to address the leakage issue. These guard rings improve cross-talk and noise immunity being a screen between two active regions. Figure 9 shows PATE[5] detectors D2 and D3 mounted on carrier printed circuit boards (PCBs). The D2 detector has a central spot, an outer ring, a guard ring between them, and a guard ring around the outer ring. The D3 detector has a single round active area and a guard ring around it. The carrier PCBs contain a bias voltage distribution circuit and cable connectors and provide mechanical rigidity for the detector assembly.

3.2.3 CsI detectors

Scintillation is a process of emitting optical photons by the ionized detector medium. Primary ionization is converted to de-excitation with a release of energy. The energy is converted either to crystal lattice phonons, eventually becoming heat, or to the emission of a photon. The scintillation photons are read-out by an optical detector such as a photodiode or a photomultiplier. The RADMON radiation monitor described in this Thesis employed CsI(Tl) inorganic scintillator; therefore, this Introduction will concentrate on properties of this type of scintillator.

[5]The instrument description is in Section PATE/Foresail-1.

Pure CsI is an alkali-halide scintillator with a highly polarized ion crystalline structure. The spectrum of its optical emission has a narrow peak around 330 nm (Schotanus and Kamermans, 1990). One recent research suggests that undoped CsI has four decay constants, with the longest being about 20 us with an intensity of about 48% of the full light output (Moszynski et al., 2016).

A small amount of thallium creates luminescence centers distributed within the CsI lattice(Gwin and Murray, 1963). Thallium ions shift the peak wavelength of scintillation photons to the green light with a wavelength of around 520 nm, which is better suited for silicon-based light sensors. The absolute light output also substantially rises with the addition of $> 10^{-3}$ mol[6] of Tl^{+} ions (Hamada et al., 2001). Thallium doping moderately shortens the decay time of luminescence (Schotanus and Kamermans, 1990). For a doped CsI(Tl), the luminescence has two components: fast and slow, which intensities are particle species-dependent, especially for heavy nuclei (Benrachi et al., 1989). The fast component has a decay time of 575...620 ns, and the slow component has a decay time of 2.4...3.34 μs (Hamada et al., 2001; Milbrath et al., 2008)

The energy resolution of scintillation detectors is inferior to silicon and solid-state detectors in general. One of the reasons is that the light collection depends on the location of the particle track. Photons reflect multiple times from the crystal edges before they are either registered or absorbed. Different surface treatment has shown variations in the light collection. The second reason is that the relative quantum yield is much lower, i.e., one MeV of deposited energy in silicon produces $2.72 \cdot 10^5$ e-hole pairs and only $5 \cdot 10^4$ photons in CsI(Tl) (Holl et al., 1988). For the RADMON radiation monitor(Kestilä et al., 2013) with the data product energy resolution $\Delta E/E \sim 50\%$, the intrinsic energy resolution of the detectors is an order of magnitude less; therefore, it was not considered to be affecting the instrument performance.

The light output of CsI(Tl) depends on the temperature of the crystal (Grassmann et al., 1985) with a plateau around +30 ...+40 degrees Celsius and a temperature coefficient of $3 \cdot 10^{-3}/°C$ at 20°C. The temperature onboard Aalto-1 was measured to be within 0...+40°C, therefore the deviation of the light yield of several percent is considered insignificant for the mission.

Radiation tolerance of CsI was studied by Valtonen et al. (2009). For a photodiode readout similar to the one used in RADMON, no observable change was observed up to the dose of 100 Gy in the light output and the transparency of selected scintillation crystals.

[6] It is the absolute ratio of the number of dopant ions to the total number of atoms in bulk.

Birks effect

Upon ionization of the scintillation medium by an incident particle, the electron-ion pairs start to recombine. The ionization density is concentrated around the incident particle track and tracks of secondary particles. The denser is the local ionization, the more chances there are for a free electron to recombine without emission of a photon. Two processes of radiative or non-radiative recombination compete for free electrons in the crystal with the equilibrium depending on densities of ionization, luminescence centers, and crystal defects (Murray and Meyer, 1961).

For a given crystal, the total light output is quenched with increased ionization density. This phenomenon is known as the Birks effect (Birks, 1964). The Birks effect is insignificant for electrons and photons since their linear energy transfer is relatively low, but it affects the detection of heavier particles such as protons and ions.

By the model proposed by Birks (1964), the quenching depends on the linear energy transfer dE/dx:

$$\frac{\mathrm{d}L}{\mathrm{d}x} = \frac{S|\mathrm{d}E/\mathrm{d}x|}{1 + kB|\mathrm{d}E/\mathrm{d}x|}\,, \tag{19}$$

where L is the light output, S is a normalization constant, E is the particle energy, and kB is a measure of the Birks effect influence on the light output. The value of the constant is measured for different nuclei, e.g. by Bashkin et al. (1958); Horn et al. (1992); Avdeichikov et al. (2000); Tretyak (2010); Koba et al. (2011). However, several authors follow the method proposed by Horn et al. (1992) where $-\mathrm{d}E/\mathrm{d}x$ is argued to be proportional to E^{-1}. The assumption allows to solve the equation (19) to obtain a formula for the light output vs. the deposited energy given in elementary functions. A paper by Avdeichikov et al. (2000) notes that accuracy of the assumption $-\mathrm{d}E/\mathrm{d}x \sim E^{-1}$ is substantially limited. A numerical integration of the equation (19) is presented by Avdeichikov et al. (2000) with a properly calculated value for kB for CsI(Tl). That value was used in research described by Paper I.

Paper I discusses a way to integrate the equation (19) for an approximation valid for the energy range or RADMON. A power-law approximation of $-\mathrm{d}E/\mathrm{d}x \sim E^{-\beta}$ where $\beta = 0.678$ follows the experimental data in PSTAR database (Berger, 1992). The approximation allows integration of (19) through hypergeometrical function ${}_2F_1$:

$$L(E_{\mathrm{CsI}}) \sim E_{\mathrm{CsI}} \cdot \left(1 - {}_2F_1(1, \frac{1}{\beta}; \frac{1}{\beta} + 1; -\frac{E_{\mathrm{CsI}}^{\beta}}{kB\, a_0})\right)\,, \tag{20}$$

where E_{CsI} is the energy deposited in CsI(Tl) scintillator, $L(E_{\mathrm{CsI}})$ is the expected luminosity, and a_0 is a constant in the power-law approximation $-\mathrm{d}E/\mathrm{d}x = a_0 E^{-\beta}$. Figure 10 shows the effect of Birks correction applied to raw deposited energy in CsI(Tl).

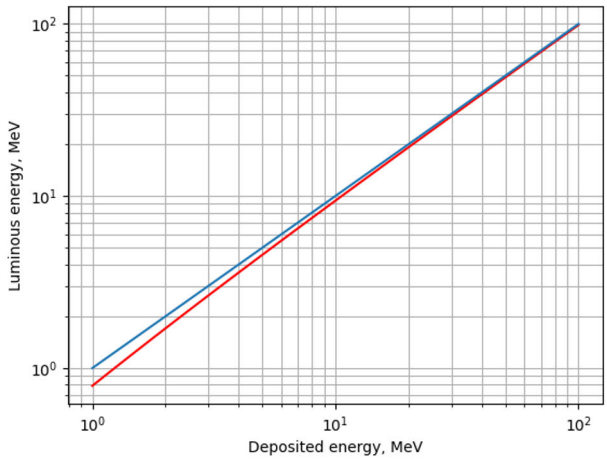

Figure 10. The Birks effect in CsI(Tl) for protons. Blue is the linear function, red is the scintillator luminosity corrected for Birks effect by the equation (20). For energies above 20 MeV the difference becomes minuscule.

3.3 Particle identification

3.3.1 ΔE–E method of particle identification

We say that a particle hits a detector if it deposits enough energy in the form of ionization to be registered by an electronic circuit attached to the detector, which is generally called a readout. Detector hits are practically electric pulses. These pulses are analyzed in time and amplitude domains to obtain valuable information about the incident particle. For instance, time-of-flight analyzers can directly measure the incoming particle speed by measuring a delay between hits in two detectors situated nearby. Detectors designed to absorb an incident particle fully can record the particle energy despite the species. However, a more complex setup is necessary to distinguish between particle species of apriori unknown energy.

One of the standard scientific objectives is to distinguish between electrons and protons or between multiple heavier nuclei. As we saw in the previous subsection, the linear energy transfer depends on the particle species, incident energy, and the properties of the material used for a detector.

One of the techniques for particle identification is the ΔE–E method, which employs a combination of two detectors. The first detector an incident particle hits is a thin semiconductor layer that absorbs a small portion of the particle initial energy. The second detector is a calorimeter, which absorbs the rest of the particle energy.

The particle discrimination relies on the difference of linear energy transfer for different particle species. Electrons deposit significantly less energy per unit length

than nuclei; heavier nuclei deposit energy proportional to their charge. Therefore, if we construct a thin ΔE detector, which absorbs only a small portion of the particle energy in the nominal energy range, it will output significantly different signals for an electron and a proton of equal energy. An ideal E detector must absorb the rest of the particle energy to point the deposited energies in both detectors on the ΔE–E plane.

It is essential that an incident particle passes the ΔE detector first. If a particle travels backward and can leave the calorimeter due to its high initial energy, it maps to a significantly different area on the ΔE–E plane. It is also important to inhibit single detector hits to minimize dead time in response to each pulse even if invalid. Therefore, it is important to add a collimator to the pair of detectors and a shield limiting particles penetrating from the back.

The particle classification decision originates from the observed position of a particle on the ΔE–E plane. The instrument has to be calibrated to synchronize the physical and digital domains of the ΔE–E method. Once calibrated, an instrument should be able to classify particle species. The calibration sets the dependence of the digital values of instrument electronics on the physical quantities, such as deposited energy, volume charge, etc. For an entirely linear detector, one should obtain its gain and an offset. It is essential to confirm these values stay the same in time; otherwise, a fresh calibration is needed.

3.3.2 Proton curve

In order to construct a detector able to differentiate between protons and electrons in a wide energy range, i.e., more than an order of magnitude, one must carefully limit spots on the ΔE–E plane. The energy range is limited at the lower end by the ΔE detector since a particle must penetrate the ΔE detector and reach the calorimeter. The upper limit is virtually set by the energy necessary to penetrate the calorimeter, but even penetrating particles might be classified correctly at energies of about 10-30 % higher than the penetration limit. However, the energy resolution plummets as soon particles get enough energy to traverse the detector stack through and scatter away.

The geometry and materials of an instrument define the shape of the area in the ΔE–E plane where a particular particle should be detected. The size of the spot depends on the characteristic scattering angle for a particle and varies with its energy and species. Electrons scatter at much larger angles than protons (see section Detection technique), forming a loose cloud in ΔE–E plane even with constant incident energy, while mono-energetic protons form a compact population. These proton ”specks” form a curved track on the ΔE–E plane as the incident energy glides within the energy range of an instrument. The procedure tersely described in Paper I is elaborated below to show the equations essential for instrument calibration.

A proton[7] that can penetrate the ΔE-detector, but not the calorimeter deposits its total energy into the detector stack. The ΔE-detector absorbs only a small part of the incident energy. For the sake of analytical solution, we consider the particle range, R [g cm^{-2}], in the detector stack as a sum of a thickness of ΔE-detector and an arbitrary range for a particle of remaining energy in the same material:

$$R(E_0) = R(E_0 - \Delta\varepsilon) + d_\Delta \rho_\Delta \,, \tag{21}$$

where E_0 is the incident particle energy, $\Delta\varepsilon$ is the energy deposited in ΔE-detector, d_Δ is the thickness of the ΔE-detector, and ρ_Δ is its density. The equation (21) establishes the relation between the incident particle energy and how much energy is deposited in the ΔE-detector. This relation defines a parametric function on the ΔE–E plane, which is unique for a given pair of ΔE- and E-detectors. The proton "track" described by the function on the ΔE–E plane allows both proton discrimination and in-flight calibration even if the exact incident energies of protons are not known.

One can solve the equation (21) for $\Delta\varepsilon(E_0)$ if the range function is reversible and the proton is stopped in the E-detector. The Bragg-Kleeman rule defines $R(E)$ as:

$$R(E') = A_0 \cdot E'^{\gamma} \,, \tag{22}$$

where $E' = E_0/(1\mathrm{MeV})$, and A_0 is a dimensional constant.

In this work we used silicon as the material for a ΔE-detector. In silicon the approximation (22) shows larger deviation in the 2 – 200 MeV energy range than one proposed by Attix (1987):

$$R_{\mathrm{Si}}(E) = \beta + \alpha \left(\frac{E}{1\,\mathrm{MeV}} \right)^{\gamma} , \tag{23}$$

where α and β are constants with dimension of length, and γ is dimensionless. The constants must be fitted to match the experimental data on protons in silicon, e.g., PSTAR (Berger, 1992). It is important to note that these constants are independent from the geometry of a particle instrument.

Let us use that the whole energy of a particle is deposited in the detector stack consisting of a ΔE-detector and a calorimeter. Let $E_c = E_0 - \Delta\varepsilon$ be the energy deposited in calorimeter. The $R_{\mathrm{Si}}(E)$ in (23) is reversible, so we obtain a solution of the equation (21) for $\Delta\varepsilon$:

$$\Delta\varepsilon = \left(\left[\frac{E_c}{1\,\mathrm{MeV}} \right]^{\gamma} + \frac{d_\Delta \rho_\Delta}{\alpha} \right)^{1/\gamma} (1\,\mathrm{MeV}) - E_c \,. \tag{24}$$

The equation (24) is a parametric definition of the "banana" curve on the ΔE–E_c plane with parameters fixed by the instrument geometry and materials. In space,

[7] Holds true for heavier nuclei, but we limit the scope to protons for the sake of consistency.

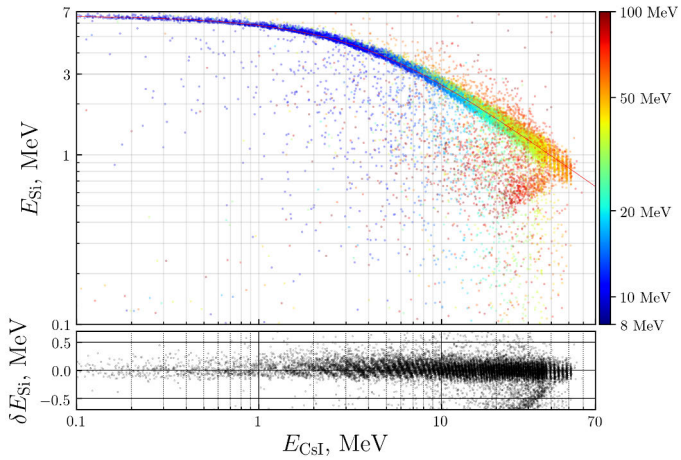

Figure 11. The analytical proton curve matched to simulation data. In the upper panel, the red curve follows the equation (25) with E_{CsI} shifted by 0.15 MeV to correct for a 2% error of the analytical range approximation at lower energies. The color of the dots shows the incident proton energy. The lower panel shows the difference between the analytical curve and Geant4 simulations. (Oleynik et al., 2020)

protons with a continuous energy spectrum fill the curve dot by dot. The shape of the curve is set by d_{Δ}, ρ_{Δ}, and constants independent on the instrument.

For an arbitrary energetic proton population, the proton "banana" curve is observed in ΔE–E$_{\mathrm{c}}$ plane. If an instrument can deliver a set of points on the ΔE–E_c plane in digital units, which are used by its particle classifier, it is possible to calibrate gains and offsets of both detectors in the stack. The curve is non-linear, whereas the detectors are considered linear; therefore, it is nearly impossible to match the observed curve to a derived one unless the gains and offsets are precise.

In Paper I, we present the calibration of the detector stack of RADMON, which has a silicon ΔE-detector and a CsI scintillator as a calorimeter. The curve obtained in space from digitized particle detections is projected to the $E_{\mathrm{Si}} - E_{\mathrm{CsI}}$ plane. The following equation shows an analytical curve, which we used to match the gains and offsets of RADMON. Figure 11 (Figure 3 in Paper I) illustrates how the analytical curve matches simulation data for protons of energies from 8 to 100 MeV.

$$E_{\mathrm{Si}} = \left(\left[\frac{E_{\mathrm{CsI}}}{1\,\mathrm{MeV}} \right]^{\gamma} + \frac{d_{\mathrm{Si}} \rho_{\mathrm{Si}}}{\alpha} \right)^{1/\gamma} \mathrm{MeV} - E_{\mathrm{CsI}}\,. \tag{25}$$

3.3.3 Aperture and collimation

The ΔE–E principle is valid if the incident particles arrive within a certain solid angle so that the ΔE detector is the first one a particle passes through in full depth.

Figure 12 illustrates one of the possible edge effects. Some particles end up

hitting the edge of the active area of a silicon detector. The detector records a reduced amount of deposited energy, which confuses the ΔE–E particle identification algorithm.

Figure 13 illustrates another possible edge effect. An energetic particle might continue to the detector even though it has traversed arbitrary length in the collimator material. The ΔE–E particle classifier will identify the right particle species of the wrong energy.

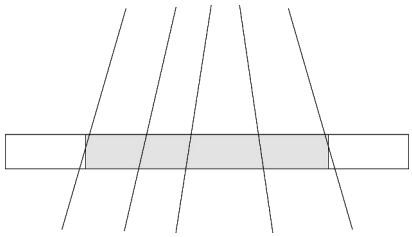

Figure 12. Edge effect for a silicon detector with an active (grey) and a passive (white) areas.

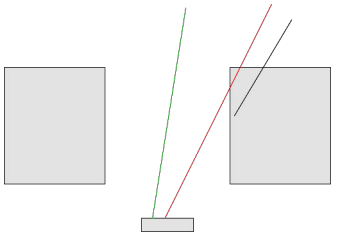

Figure 13. Edge effect for a detector with a non-optimized collimator structure. Green is the particle track for a nominal detection, red is for touching the edge of collimator, black is a nominally absorbed particle.

Both effects are relevant for RADMON. The first one introduces ”bleeding” of proton detections down from the proton curve with their ΔE signal reduced. The second effect allows energetic protons in the SAA to enter the detector at a wider solid angle than nominal. Such aperture widening contributes to elevated geometric factors for protons above 50 MeV. The possible solutions are discussed in Paper IV, where a heavier shielding and a modified geometry of the RADMON entrance window are proposed.

If a particle passes the calorimeter first and then the ΔE detector, the classification rules become substantially different. First, the particle must have enough energy to penetrate the full depth of the calorimeter. Second, it deposits substantially more energy in ΔE detector than it would do hitting ΔE detector first. The particle classifier should be constructed in a way that scores such particles as ”other” or ”trash” so that they do not create an additional background in particle channels. They can be discarded, but retaining them helps to tune the instrument in space if, for an unusual reason, nominal detections get misplaced in the ”trash”.

4 Space experiments

Once launched to space, a small space experiment continues on its own without means to alter its design from the ground. The choice of detectors, the design of their readout, the particle classification logic, and the rest of the software require a great amount of care and rigorous planning of possible malfunctions and ways to overcome them.

The space environment is unique; its replication on the ground is usually unreasonably expensive for a small space mission. Likely, the first comprehensive calibration of a miniature particle instrument occurs already in orbit. It does not, of course, devalue the ground-based measurements but sets a reasonable schedule for the proper assessment of the instrument response to energetic charged particles. Software of a spaceborne particle instrument should include a diagnostic mode, which gives insights into the possible changes in calibration both right after launch and during the mission.

This chapter briefly introduces the design of particle instruments discussed in Papers I-IV: Aalto-1/RADMON and Foresail-1/PATE. Next, it describes the calibration techniques applied for the instruments in the presented Thesis and provides an overview of space missions comparable to RADMON and PATE.

4.1 Instrument design

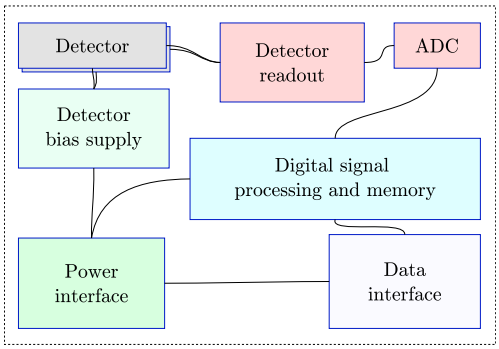

Figure 14. Basic structure of a small particle instrument designed for a CubeSat mission. The dashed line marks the instrument as a spacecraft payload. Data and power interfaces are connected to the spacecraft subsystems.

The scope of the thesis is focused on the use of Monte Carlo simulations of particle instruments, which is an essential element of the instrument design process in modern research. The design of a space instrument evolves in a non-linear fashion. The first round of a spiral path leading to the optimal design starts when a scientific question transforms into requirements for the measurement. A set of detectors should be preliminarily selected at this step. The detectors are likely to be simulated alone in vacuum in the virtual world. The second round involves the simulation analysis that may give the green light for the next step or another round of detector selection.

Further, the instrument requirements eventually crystallize into a crude model of a scientific instrument, which is to be polished using simulations. At later steps, one should define data products and consider the power and data budgets. Eventually, the instrument is ready for production when there is nothing to add or remove from the design.

There is usually little space on a CubeSat, which may fit one or two instruments with compact detectors. A basic structure of such an instrument is shown in Figure 14. In every instrument, several sub-units influence the way one interprets the simulation results. For instance, one must take a realistic threshold and dynamic range of the detector readout into account to make a precise computer simulation representative of the actual system.

4.1.1 Aalto-1/RADMON

RADMON is a compact radiation monitor aimed at observing energetic electrons and protons in low Earth orbit. Its mission is to monitor the radiation environment in Van Allen radiation belts in a circular orbit with in altitude of about 500 km. The monitor detects electrons of energies 1.5 – 10 MeV and protons of energies 10 – 100 MeV. Incident particles are classified and counted in several energy channels; the counter values are recorded in the memory each 15 seconds[1] producing time history of the particle flux.

RADMON utilizes a classical ΔE–E method to identify particle species. The ΔE detector is a $2.1 \times 2.1 \times 0.35\,\mathrm{mm}^3$ silicon detector, surrounded by a silicon passive area of $3.5 \times 3.5 \times 0.35\,\mathrm{mm}^3$. The detector is mounted on a PCB. The E detector, or a calorimeter, is a $10 \times 10 \times 10\,\mathrm{mm}^3$ CsI(Tl) scintillator crystal with a photodiode readout. The photodiode is a Hamamatsu S3590-08 silicon photodiode with a depletion layer of 300 μm. The detector stack is protected by a brass envelope from particles penetrating from sides. The brass collimator restricts the field of view to a solid angle of about $\pi/5$ to ensure the ΔE–E technique is useful. The brass shield is effective in absorbing protons up to 50 MeV; for electrons, the limit is about 8 MeV (Kestilä et al., 2013; Peltonen et al., 2014; Oleynik et al., 2020).

[1] In the angular measure it is about 1° along the orbit.

The radiation monitor produces scientific data in nine proton energy channels and five electron energy channels with a temporal resolution of 15 seconds. Each 15-second record is saved with a timestamp. The instrument also features a pulse-height mode and an oscilloscope mode for calibration. The first one produces particle-wise records of detector pulse-heights that correspond to deposited energies. The pulse-height mode allows an in-flight calibration discussed in Paper I. The oscilloscope mode allows direct observations of detector signals. The oscilloscope records assist in the assessment of noise and electromagnetic interference when the instrument is in orbit.

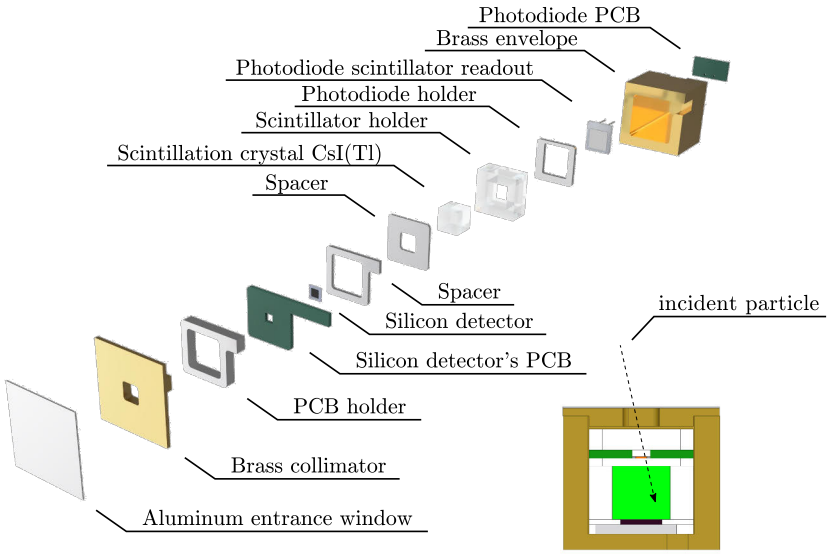

Figure 15. An exploded view of RADMON detector unit. In the lower right - an illustration of the particle detection principle.

An exploded view of the detector stack and its envelope is presented in Figure 15.

4.1.2 PATE/Foresail-1

PATE is a small ($94 \times 94 \times 140$ mm^3) particle instrument designed for the Foresail-1 CubeSat and equipped with two narrow-field energetic particle telescopes with an identical set of detectors. The scientific objectives of PATE are the following:

1. To observe and quantify the electron precipitation from the Van Allen radiation belts;

2. To observe solar energetic neutral hydrogen atoms reaching the Earth during the most intensive solar flares.

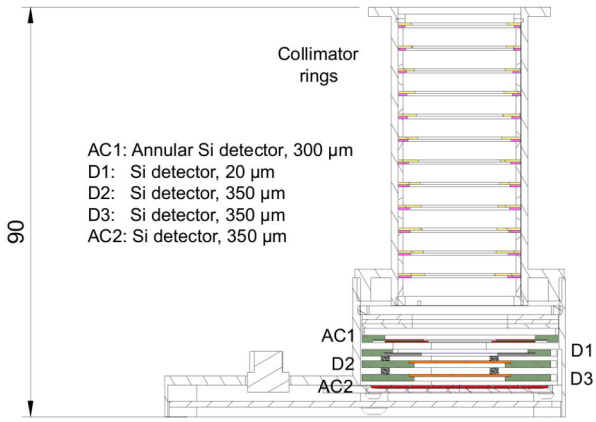

Figure 16. A cross-section of the Sun-pointed tube of the PATE particle telescope. The height is in millimeters. (Vainio et al., 2019)

The telescopes differ in the opening angles of their collimators according to individual observation tasks. One of the telescopes looks in the Sun direction to catch solar energetic neutral hydrogen atoms; its aperture is a cone of about 10°opening angle. The second telescope looks in the perpendicular direction. Foresail-1 will rotate around the spacecraft–Sun axis with a period of about 15 seconds. Thus, the second telescope scans the pitch-angle distribution of the particle populations in the Van Allen radiation belts converting the angular distribution into the time domain. The entire rotation is divided into 32 logical sectors providing an angular resolution slightly coarser than 10°.

PATE has a stack of silicon detectors under a collimator tube housed in an aluminum envelope. The detector stack consists of five detectors, D1, D2, D3, AC1, and AC2. The detectors are housed in an aluminum envelope with a collimator. AC1 is an annular detector with a hole that is the deepest element of the collimator. Other detectors are solid planar silicon detectors. The collimator tube is an aluminum tube with multiple rings; each ring is a sandwich of aluminum and tantalum rings. Tantalum effectively stops charged particles, and aluminum suppresses the scattering of electrons inside the collimator tube. Figure 16 illustrates the instrument geometry.

The computer-aided render of the instrument is presented in Figure 17 and 18 (Figures 1, 2, and 3 in Paper III), which display the mechanical design and the structure of the detector stack used in PATE.

PATE uses a combined ΔE–E method to identify particle species. The first detector pair is D1 and D2. D1 is thin enough to pass electrons without producing a detectable signal, whereas D2 detects protons of energies below 10 MeV. A particle hit triggering only D2 is classified as an electron, and a hit in both D1 and D2 is classified as a proton unless other detectors produce a signal. The following detector pair aimed at electrons of higher energies is D2 and D3, with the condition that D1

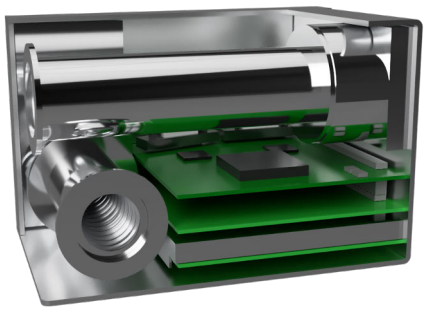

Figure 17. The computer-rendered image of PATE with one cover removed. (Oleynik et al., 2020).

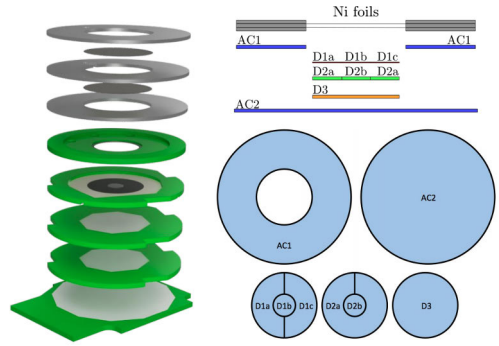

Figure 18. Left: an exploded view of PATE detector stack. Right: The detectors in the order they are installed with a chart showing their relative sizes. (Oleynik et al., 2020).

does not have a signal. The last combination of the detectors is D2, D3, and AC2, which catch the most energetic particles able to penetrate the whole stack.

The combined ΔE–E method allows PATE to detect and classify protons (or neutral hydrogen atoms) of energies below 0.5 MeV to 10 MeV into ten energy channels and electrons of energies of about 100 keV to 1 MeV into seven energy channels. There are several special channels for penetrating particles and a ”trash” channel for accounting for the dead-time.

The PATE calibration data is similar to the one in RADMON. The pulse-height data contains digitized pulse-heights from all eight detector plates, three for D1, two for D2, and one for D3, AC1, and AC2. The comprehensive record allows precise simulations relevant to environments both on the ground and in space. In a monoenergetic accelerator beam, it is possible to fine-tune the energy thresholds for the particle energy channels. In space, the calibration is planned to be similar to the one of RADMON (see Paper I). The oscilloscope data is used in the same way as in RADMON.

4.2 Instrument calibration

The raw data stream of a particle instrument consists of sets of numerical values reflecting the energy deposited in the sensitive volumes of the instrument, i.e., the detectors. The values are obtained by analog-to-digital conversion of analog signals produced by the detectors. The numerical values are further analyzed using a logic engine to create single particle detection records or to increment particle counters.

The path from a physical detection of a particle to an update in digital memory is relatively long. Each step performs a conversion operation, which may or may

not be reversible. Figure 19 shows an illustration of the signal path inside a particle instrument.

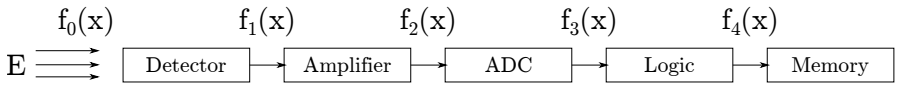

Figure 19. The signal path in an instrument.

First, $\mathrm{f}_0(x)$ might be a linear function of deposited energy with no offset. Though a scintillator with the Birks effect, or a saturating photosensor will introduce non-linearity. The non-linearity or an added offset of the next step $\mathrm{f}_1(x)$ might be introduced by saturation or overshooting in electronics. The ADCs might have an offset and gain error, differential or integral non-linearity. The next $\mathrm{f}_3(x)$ does not seem to be a problem at all, though a digital clipping might occur. The last step might have deliberately non-linear $\mathrm{f}_4(x)$, for example, to reduce the bit-width by applying a log-scale to the energy. Being useful itself, it might misbehave if earlier steps have introduced an offset beyond a margin.

The ultimate goal of calibration is to find a relation that maps the digital data of measurement into the measured physical quantities. We use radioactive sources and accelerator beams to establish the dependencies of the detector signals on the deposited energy. To estimate which incident energy activates a particular particle classifier, we simulate detector signals by precise pulse generators. Finally, we combine measurement in the laboratory with simulations to provide the response functions of the particle channels of the the instrument.

The voltages or currents measured at the detector outputs are functions of deposited energy, which are quite close to linear functions. A counter-example is a scintillator with the Birks quenching effect; the transfer function includes a non-linear part, depending on the particle species and the deposited energy. However, even if the transfer function is linear, it has two variables, which link the numerical value to the deposited energy of the particle. The calibration process is to establish the transfer functions of each stage of the measurement.

For a data product, counts obtained by an instrument must be converted to physical units so that they are comparable with the data produced by other instruments. A response function and a count rate could be used as well, but it is more convenient to deal with channel energies and geometric factors. We derive these quantities using the bow-tie analysis introduced by Van Allen et al. (1974)[2] that yields a simplified picture of the instrument channels.

While each instrument is first calibrated on the ground, it is necessary to confirm the calibration in space repeatedly. Harsh vibrations during the launch, radiation

[2] See section Bow-tie analysis for details of the method.

damage, or thermal aging may affect how detectors perceive the energy deposited by charged particles.

Instruments of large missions, for example, THEMIS/SST (Ni et al., 2011), are extensively calibrated and cross-calibrated in-flight. The work presented in the Thesis intends to extend the practice of thorough verification of particle instruments to nanosatellite missions.

4.2.1 RADMON calibration

RADMON has a special Calibration mode for ground and in-flight calibration. In the Calibration mode, the instrument delivers raw digitized amplitudes of ΔE–E detector pulses. Protons traverse RADMON detectors without much scattering. The trajectories of these protons and the energy they deposit in detectors are determined by detector materials' properties, which quite feasibly stay unchanged.

In the range of energies about 10 – 30 MeV protons produce a pronounced track on the ΔE–E plane (see 3.3.1). The track position and shape are restricted by the instrument geometry, much less affected by the signal path and electronic gains. The non-linear shape of the track locks degrees of freedom of the detector transfer functions and prevents calibration procedure from picking the wrong offsets and gains. Matching the proton track to the simulations allowed us to calibrate RADMON while it was operating in space. The calibration data obtained in space has a mixture of particle hits. One can never guarantee that the collected hits originate from protons within a narrow range of 10 – 30 MeV. The correct set of points must be picked by a machine learning method that sorts mixed set into groups based on their spatial location without prior knowledge of what the groups should be. The core algorithm is k-nearest neighbors (Altman, 1992). The base version has the drawback of reduced performance on a dataset with background noise. Hence, an advanced version of the k-nearest neighbors' algorithm with hierarchical density by McInnes et al. (2017) (HDBSCAN) was employed in Paper I. The algorithm uses the density of points as a measure for their relationship to a particular cluster with further extraction of the most significant clusters as proposed by Campello et al. (2013). The points on the ΔE–E plane are sorted into clusters, with the proton track being one of them.

Once the data points are selected, the best-fit parameters of the curve are obtained by an iterative Levenberg-Marquardt fitting algorithm (Levenberg, 1944; Marquardt, 1963). The algorithm minimizes the value of the generalized sum of residuals. For a smooth function, a simple measure of least residuals squares would be sufficient

$$S = \sum_{1}^{N} (y_i - f(x_i))^2 \,,$$

where $(x_i, y_i)|_1^N$ are the experimental points for a function $y = f(x)$ to be fitted. The proton track is a parametric function that has a variable slope along the curve,

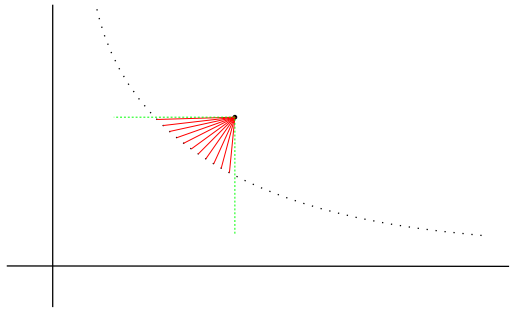

Figure 20. The minimization of the distance from a point to the analytical curve represented in dots. Red lines show the candidates for minimization. The green lines show the minimization scope.

which makes the simple least-squares measure favoring the range where the slope is sharp. The sum of squares of euclidean distance from the experimental points to the analytical proton track has to be used to level the influence of the points along the track on the final result.

$$S = \sum_{1}^{N} \mathrm{dist}((x_i, y_i), y = f(x))^2 \,, \tag{26}$$

where $\mathrm{dist}((x_i, y_i), y = f(x))$ is the true distance between a point (x_i, y_i) and the curve $y = f(x)$. If a curve is represented by a dense set of points, the distance between an experimental point can be minimized with an error not exceeding the distance between the curve points. Figure 20 illustrates the distance concept.

The minimal distance between an experimental point and one of the points representing the proton track is then $d((x_i, y_i), f(x))$. The sum (26) is minimized with Levenberg-Marquardt fitting algorithm by variation of parameters of the proton curve. The parameters are the instrumental gains and offsets that define the instrument transfer function. The instrument transfer function is a fold of the (25) with (20), where energies are converted to the digital domain the following way:

$$\begin{aligned} \mathrm{ADC}_{\mathrm{CsI}} &= E_{\mathrm{CsI}} * A_{\mathrm{CsI}} + B_{\mathrm{CsI}} \\ \mathrm{ADC}_{\mathrm{Si}} &= E_{\mathrm{Si}} * A_{\mathrm{Si}} + B_{\mathrm{Si}} \,, \end{aligned}$$

where A are the gain, and B are the offset for detectors (CsI, Si), and ADC is the numerical value of the digitized pulse-height for the energy deposit E.

Figure 21 shows the proton track used for calibration, the calibration points acquired in orbit, and the regions of ΔE–E plane used by the RADMON particle classifier. The calibration points marked in green are the points used for the parameter fitting.

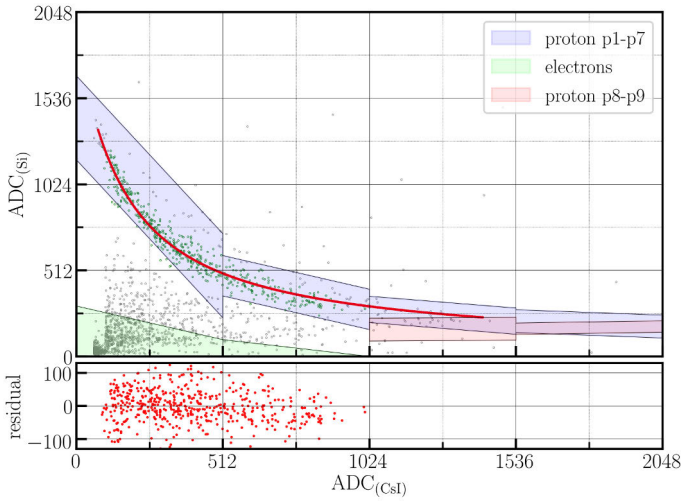

Figure 21. A fit of the proton "banana" track to the in-flight calibration data. Colored polygonal areas show the particle classifier rules for electrons and protons. (Oleynik et al., 2020)

4.2.2 PATE calibration

Upon a particle interaction with the stack, the signals from detectors are digitized by a 14-bit ADC into pulse-height values. The digital filter applied to the ADC values eliminates a DC bias. The pulse-heights are proportional to the deposited energy as $V_{\mathrm{ph}} = g * E_{\mathrm{dep}}$, where E_{dep} is the deposited energy, g is the conversion gain, and V_{ph} is the digital pulse-height. The detection logic analyzes the pulse-heights and classifies the particle event to belong to one of the particle channels or the Others(trash) channel[3]. To ensure correct classification, the conversion gains must be defined (measured) for each detector. Gains allow the classifier to operate in the energy domain rather mere digital, which allows particle identification and estimation of its incident energy. The calibration process can be summarized to the measurement of gains for each detector.

PATE has a special Pulse-height mode for ground and in-flight calibrations. In this mode, the pulse-heights are reported for each detection before the particle classification occurs. Using the Geant4 simulations, one can predict how a histogram of the pulse height data looks when the instrument is exposed to certain charged particle flux.

We plan to use the following particle sources for PATE on-ground calibration:

- Particles emitted by a radioactive calibration source, e.g., ^{207}Bi (β^-) and ^{241}Am (α);

[3] Paper III discusses the particle classification in more detail.

- Independently calibrated proton beam (proton energies 1.0 – 10.2 MeV) at Kumpula accelerator facility of the University of Helsinki.

PATE can be calibrated in-flight using the same principle as we described for RADMON in Paper II. One may consider D1 and D2, and D2 and D3 as ΔE–E pairs of detectors. Each pair has its intrinsic properties defined by the material and thicknesses, which allows the instrument to be calibrated the same way as RADMON using proton curves. Geant4 simulations of PATE set the expected distributions of the in-flight pulse-height data for a mixed particle environment containing protons of energies between 3 and 10 MeV. These protons form proton curves for above mentioned pairs of detectors in a ΔE–E plane for each pair. The shape of the proton curve is defined by the thicknesses of detectors and their relative positions. The incident spectrum of particles and possible contamination by particles penetrating the collimator and detector housing should not change the curve but lower the signal-to-noise ratio. The measurement campaign performed with RADMON in low-Earth polar orbit demonstrated that the interference from penetrating species on the proton curve is minimal. Thus, an in-flight calibration for PATE should be considered as viable option for in-flight verification of the instrument performance.

4.3 Referenced space missions

> The science community as a whole should acknowledge the usefulness of small satellites and look for opportunities to leverage developments in the small satellite industry. All branches of space science can potentially benefit from the smaller envelope, the associated lower cost, and higher repeat rate.
>
> A COSPAR scientific roadmap. (Millan et al., 2019)

The first solar-powered satellite in space, Vanguard-1, was a nanosatellite in the modern classification. Launched in 1958, Vanguard-1 has a weight of 1.46 kg and a spherical body diameter of 16.5 cm. It proved the concept of solar power for a satellite by operating for seven years. However, the technology of the 1950s-1960s did not allow precise scientific measurements in such a small size. The satellites' dimensions increased with increasing demand for larger imaging apertures and higher power consumption.

The space technology trend changed to nanosatellites in 1999 with the start of the CubeSat project. The CubeSat project provides standards for satellite design to reduce cost and development time. Standard dimensions allow for more accessibility to space since the developer of a satellite and the launch provider do not have to customize a launch vehicle for every customer. It is required, that a failure of a nanosatellite does not affect the launch vehicle or any other satellite in the batch (Liddle et al., 2020).

4.3.1 CubeSat missions

A 1-unit CubeSat format is a $11.35 \times 10 \times 10\,\mathrm{cm}^3$ cube with a mass slightly above 1 kg. Such missions mostly aim at technology or science demonstrations. Their solar panels cover the satellite body. Larger formats feature a 1.5-unit satellite, which is a $17.02 \times 10 \times 10\,\mathrm{cm}^3$ right angle parallelepiped, and a 3-unit one, which is a $34 \times 10 \times 10\,\mathrm{cm}^3$ tall bar. A bit infrequent, a 6-unit CubeSat is a $34.05 \times 20 \times 10\,\mathrm{cm}^3$ block, often with deployable solar panels and advanced attitude control and determination systems.

The Thesis describes two particle instruments designed for CubeSats, RADMON onboard Aalto-1 mission (Peltonen et al., 2014) and PATE onboard Foresail-1 mission (Paper III). There are several existing and planned CubeSats with similar scientific objectives and particle instruments that should be mentioned.

A 3-unit CubeSat, Colorado Student Space Weather Experiment (CSSWE), launched on September 13, 2012, into an orbit with an inclination of 65° and an altitude of 480 × 780 km, has been operating for two years. CSSWE carried the

Relativistic Electron and Proton Telescope integrated little experiment (REPTile), which is a small particle telescope in heavy element shielding. It measured protons of energies 9 – 40 MeV and electrons of energies 0.58 – >3.8 MeV in three energy channels. The telescope consisted of four silicon detectors layered into a compact detector stack shielded by a tungsten envelope. The geometric factor of the telescope is 0.2 cm^2 sr. The telescope should have scanned the pitch-angle distribution of charged particles, though the pitch-angle data is not included in the mission data product. The telescope was verified with a Geant4 model in a parallel beam incident at different angles (Baker et al., 2013; Schiller et al., 2014).

A 1.5-unit pair of CubeSats, the FIREBIRD-II, launched on January 31, 2015, into a polar orbit with an inclination of 99.1° and an altitude of 632 × 433 km, is operational. The FIREBIRD-II experiment carries the FIREBIRD Instrument for Relativistic Electrons (FIRE), observing electrons with energies from 200 keV to >1 MeV, in six energy channels. Also, FIRE is sensitive to protons of energies above 1 MeV. The FIRE instrument consists of two particle detectors. Each detector is a single, round, 32 mm in diameter, 1.5 mm thick silicon detector covered with aluminum foil, stopping low energy radiation. Electrons of energies up to 1.05 MeV are fully absorbed with an insignificant rate of penetration. The minimal electron energy is 200 keV for each detector. One of the detectors is exposed to the 2π solid angle of outer space. Another detector has an aluminum collimator that moderately reduces acceptance with the increase of the incident angle. The instruments are verified with a Geant4 model in a cosine-law radiating sphere using a monoenergetic flux of particles (Johnson et al., 2020; Crew et al., 2016).

A 3-unit CubeSat, the Compact Radiation belt Explorer (CeREs), launched on December 16, 2018, into a polar orbit with an inclination of 85° and altitude of 500 km, is operational. CeREs carries the Miniaturized Electron pRoton Telescope, MERiT, which observes electrons in two energy ranges from 5 to 200 keV and 1 – 8 MeV, and protons of energies 200 – 400 keV and 7 – 100 MeV. The instrument has differential energy channels with an energy resolution of about 30%. MERiT measures electron microbursts with a time resolution down to 4 ms. The detector stack consists of an avalanche photodiode and several layers of silicon detectors. The geometric factor of the instrument is 31 cm^2 sr for electron energies above 1 MeV and 0.05 cm^2 sr for the lower energy range. The detector stack is shielded by a composite aluminum-tungsten housing. The instrument was characterized with Geant4 simulation combined with extensive calibration in a low-energy electron beam and with radioactive calibration sources (Kanekal et al., 2019).

A 6-unit CubeSat, CuSP (CubeSat mission to study Solar Particles), formerly CuSPP+, is a mission planned for an interplanetary trajectory. The spacecraft will carry the MERiT particle telescope upgraded to detect ions up to iron with an energy of 5 – 170 MeV/n (Fe) (Desai et al., 2019).

Two particle instruments discussed in Paper II and the Discussion chapter are presented below in more detail.

4.3.2 PROBA-V/EPT

The PROBA-V (PRoject for OnBoard Autonomy–Vegetation) is a 158 kg, ESA minisatellite[4] equipped with three cameras for remote sensing. The satellite cameras covers entire surface of the Earth each two days. The mission has environmental objectives in assessment of climate impact, agricultural monitoring, and management of surface water resources.

PROBA-V operates in a polar low-Earth orbit with an inclination of 98.7° and an altitude of 820 km. The satellite has been launched on 7 May 2013 by ESA from the Kourou launch site.

PROBA-V/EPT is a a compact ($128 \times 162 \times 212\text{mm}^3$) particle instrument with a mass of 4.6 kg. The field of view has a conical shape with a 52° opening angle. Electrons are detected up to the incidence angle of 55° due to scattering in the entrance window. Figure 23 presents the internal detector structure of the instrument, and Figure 22 shows a photo of the instrument assembly. Detectors S1/S3 and S2 comprise the low-energy ΔE–E section, and D1–D10 comprise the high energy section. The instrument employs classical ΔE–E technique for low energies (below 13 MeV for protons) and matching of a hit pattern in a series of Digital and Absorber Modules (DAM) for high energies. Each DAM consists of a degrader plate and a silicon detector. The degrader plate is either aluminum or tungsten. The silicon detector has a diameter of the sensitive area of 35 mm and a 10mm-wide anticoincidence ring around the central spot.

The instrument detects electrons of energies 0.5 – 20 MeV, protons of energies 9.5 – 300 MeV, and He-ions of energies 38 – 1200 MeV. PROBA-V/EPT was verified with a Geant4 model and a particle source covering the 78 mm diameter EPT aperture imitating the through hole in the satellite body for the entrance window of the instrument. About one billion events originating from modeled electrons, protons, and helium ions of energies within the nominal range were registered by the simulation code. The calibration was confirmed in an accelerator beam of protons of an energy up to 105 MeV. The off-axis contamination was negligible in a proton beam up to 203 MeV (Cyamukungu et al., 2014).

PROBA-V/EPT observes dynamics of the outer radiation belt at a higher altitude than RADMON, but at a similar range of L values. Paper II compares RADMON measurements to the PROBA-V/EPT data for the same time period.

[4]Less than one cubic meter spacecraft.

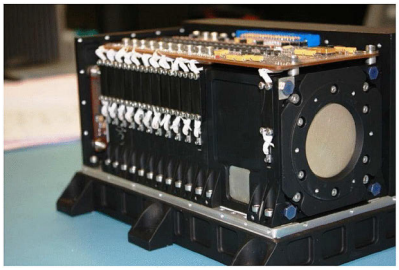

Figure 22. PROBA-V/EPT instrument. Image credit: ©2014 IEEE (Cyamukungu et al., 2014)

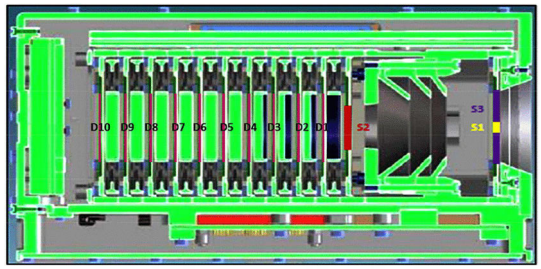

Figure 23. PROBA-V/EPT internal structure. Image credit: ©2014 IEEE (Cyamukungu et al., 2014)

4.3.3 POES/MEPED

Polar-orbiting Operational Environmental Satellite (POES) is a series of spacecraft operated by the National Oceanic and Atmospheric Administration (NOAA). The NOAA-15 satellite was the first one to carry an upgraded version of the Space Environment Monitor (SEM-2), which was also used on ESA Meteorological Operational satellite (MetOp) series. Out of the total 19 satellites, five are currently in operation, each of them has the SEM-2 equipment set. The satellites are operating at an average altitude of 817 kilometers in Sun-synchronous orbits with an inclination of 98.7°.

MEPED is a compact[5] instrument with dimensions of $282 \times 252 \times 138\mathrm{mm}^3$ and a mass of 8.7kg. The instrument provides both directional and omnidirectional measurements. Figure 24 illustrates the installation place of MEPED on the carrying spacecraft. MEPED comprises eight separate particle detector units, two solid-state proton telescopes, two solid-state electron telescopes, and four omnidirectional detector units observing energetic protons of energies $>$16 MeV, $>$35 MeV, $>$70 MeV, and $>$140 MeV incident from a 2π solid angle. The electron telescope (Figure 25) has three energy channels for an energy range of 30 – 2500 keV. The proton telescope (Figure 26) has six energy channels for an energy range from 30 to $>$6900 keV. The nominal geometric factor in both telescopes is 0.01 cm^2 sr.

The telescopes have been verified using Geant4 simulations. A model of each instrument was placed inside a radiating sphere of a 3.5 cm diameter. In total nine billion particles of each species were simulated to obtain geometric factors of the instrumental channels (Yando et al., 2011).

MEPED instruments has been flown onboard multiple NOAA/POES satellites; their data offers a unique, nearly continuous record of energetic particle fluxes since 1978. The data archive covers more than three solar cycles. To ensure data integrity, an in-flight re-calibration was performed using satellite close conjunctions. The

[5] Compared to the hosting meteorological satellite with a total mass of several tons.

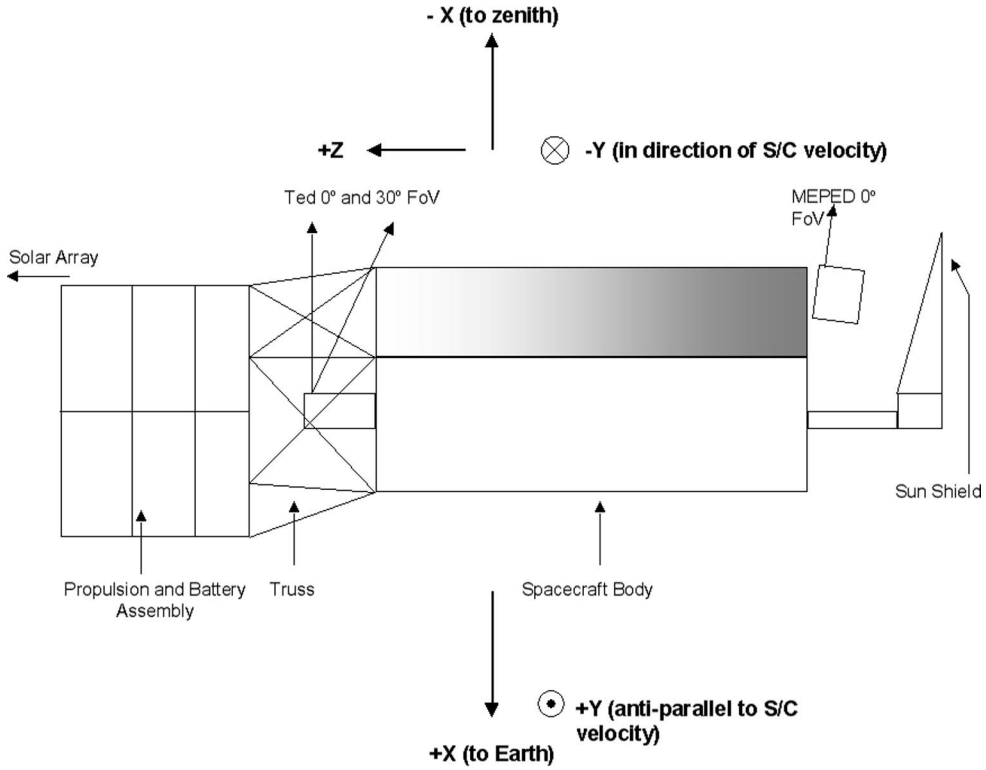

Figure 24. MEPED placement in respect to the spacecraft body. Image credit: NASA, SEM-2 documentation (Evans and Greer, 2004)

time history of detector degradation was monitored for several years at each satellite (Asikainen and Mursula, 2011; Asikainen, 2019).

PATE (Paper III) will be observing electrons in similar energy range with a larger geometric factor of more than 0.06 cm^2 sr. In the Discussion chapter we compare two instruments and discuss in which way PATE has an advantage in radiation belt observations.

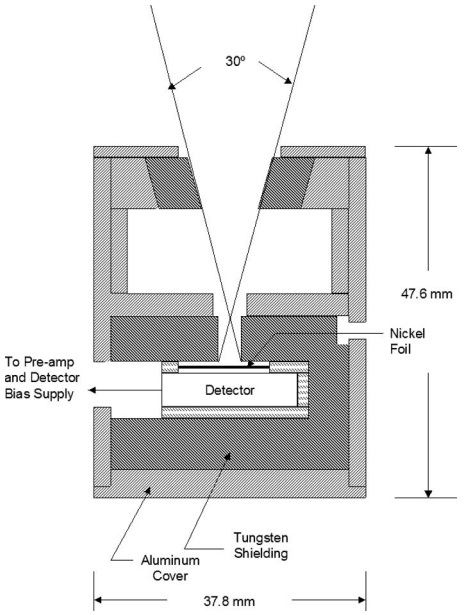

Figure 25. A cross-section of the MEPED electron telescope.

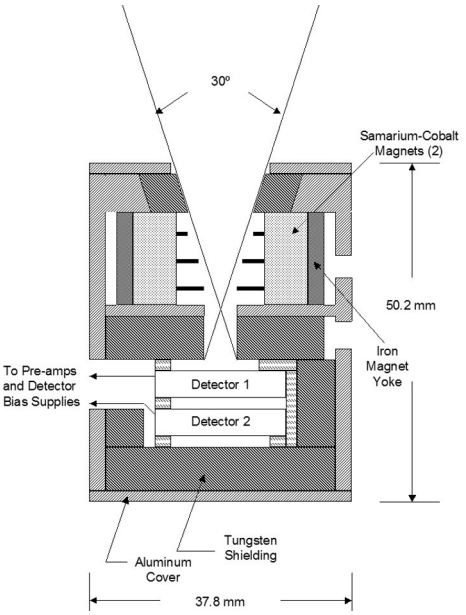

Figure 26. A cross-section of the MEPED proton telescope.

5 Geant4 simulations

The Geant4 (GEometry ANd Tracking 4) is a toolkit for the simulation of the interactions of elementary particles passing through matter (Agostinelli et al., 2003; Allison et al., 2006; Allison et al., 2016). It is an open-source software developed by the Geant4 Collaboration. The leading institution of the Collaboration is CERN. The software has extensive databases on particle interaction with matter, each other, and electromagnetic field. The Geant4 software license excludes any warranty on the software performance and necessitates citing the core publications on the Geant4 by the Geant4 Collaboration.

5.1 Introduction

Geant4 feasibly is a framework rather than a standalone software since the essential parameters of a simulation are set up by the user by writing their code in C++. The main application must have a predefined structure, including a description of the simulation World, particle sources, sensitive detectors, relevant physics processes, etc. Figure 27 shows the basic structure of a multi-threaded Geant4 application. Such entities as physics processes used in the simulation or the geometry and materials are globally defined. The multi-threading gives boost in performance for the worker threads that generate particles, compute the particle tracking and interactions, account for the deposited energy and collect the events' data. These threads are almost independent from each other, which allows effective concurrent execution.

The user must describe a virtual World with necessary details, such as geometry and materials of its entities, particle sources, and electromagnetic fields if needed. Every description is a particular C++ class derived from the base classes defined in the Geant4 core.

For instance, consider a steel bar and the amount of data necessary to describe details of an arbitrary steel bar located somewhere in a real-world laboratory to a person who has never seen it before. The bar can be large or small; maybe it is magnetized, lying on a table or in a cabinet, one surface may be mirror-polished, etc. The list of properties and physical dimensions becomes a collection of the following C++ objects in Geant4:

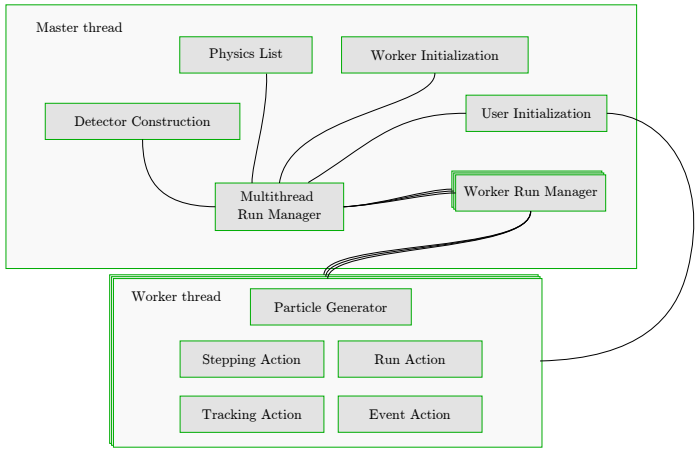

Figure 27. The structure of a multi-threaded Geant4 user application. User Actions are classes assisting in reading out the simulation results. These classes are thread-local. User Initializations are the classes responsible for setting up the simulation. These classes are shared across threads and governed by the G4MTRunManager class. The schematic is based on an image obtained with permission from Elsevier. (Allison et al., 2016)

- Physical volume in the Geant4 World (unique name)
  - Logical volume of steel bar (unique name)
    - Geometry-defining class for a bar (height, width, length)
    - Material-defining class for steel
      - A list of atom-defining classes for compounds
      - Density, atomic or mass composition
      - A class for optical properties (optional)
    - Electromagnetic field-defining class (optional)
  - Position-defining class, (x,y,z) placement
  - Rotation-defining class, rotation transformation
  - A link to a sensitive detector class (optional)
  - A link to a surface-defining class (e.g., is the bar mirror-polished?) (optional)

The significant difference from a real-world bar is that a Geant4 bar could have the sensitivity to elementary particles regardless of its material. A Geant4 sensitive volume does not have to be a radiation detector by design. Sensitive detectors are parts of the World general geometry, but in addition to the material and the shape, they incorporate classes with descriptions of what must be recorded if the particle track crosses the volume. Each time such an event occurs, Geant4 calls a dedicated method to read out the energy or charge deposited at the event. Consequently, the

simulation results are the readout from the detectors, which can be written out raw or processed in place, e.g., summarized in a histogram.

To make particle events happen, a particle source must be defined. Particles are generated by a dedicated class, tuned to imitate an accelerator beam, a uniform particle flux, or a radioactive source. Unlike a real-world particle source, a collimated beam of particles with a precise energy distribution is the simplest to implement in the code. In case a continuous energy spectrum is required, intensities are simulated count-wise to populate the given spectral shape. The more particles are in the simulation, the better the coverage of a given probability density function.

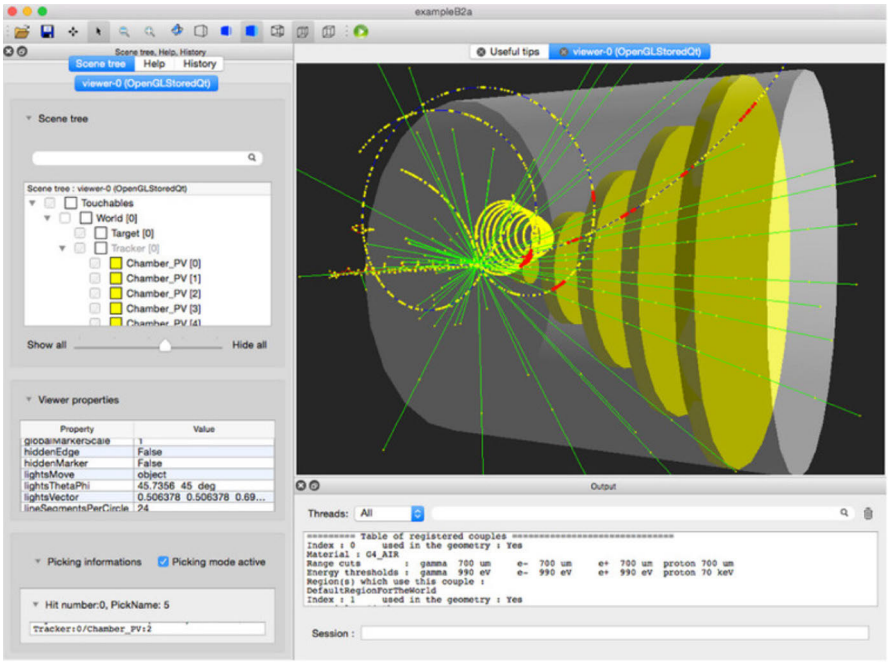

Figure 28. The graphical user interface of Geant4. Image obtained with permission from Elsevier. (Allison et al., 2016)

Finally, Geant4 allows the researcher to visually check if the simulation is functioning in the intended way. A Geant4 application may include a graphical user interface (GUI). GUI visualizes the constructed model of an instrument and supporting structures and allows 3D navigation in Geant4 World. It is also able to run a short simulation and show the resulting particle tracks for debugging purposes. (See Figure 28). GUI has a command-line interface for text commands, which control the simulation.

5.2 Simulation method

A particle instrument usually comprises several detectors, a mechanical structure such as a collimator or a detector holder, readout electronics, and a casing. The instrument is intended to use in the space particle environment, which is quite different from ground-based particle beams. In space, particles hit the instrument from all directions. Therefore, each instrument part affects particle detection even if a specific piece is not designed to influence the performance directly. Thus, the instrument simulation must include its precise digital 3D model placed into a 3D model of the spacecraft, so the results are relevant to the performance of the manufactured device. A 3D chamber model in the testing facility is used instead of the 3D spacecraft model to simulate the ground-based environment.

5.2.1 Physics processes

Physics processes in Geant4 are classes providing models for an extensive set of physics processes and their cross-sections. The processes are organized in lists, which assist the comprehensive representation of the real-world physics in a specified domain (Geant4, 2021; Allison et al., 2016). Each process can alter a primary particle parameters, generate secondary particles, delete the primary particle, and deposit energy into material according to the built-in models. Geant4 throws dice each simulation step to choose the process to be simulated[1].

A specialized transport process activates if no particle interaction has to occur, but the particle needs to be moved to the next volume boundary. The transport process is also responsible for altering the particle path in the electromagnetic field (Geant4, 2020).

In the context of simulation of the space environment, two physics lists should be considered:

FTFP_BERT. This list incorporates standard electromagnetic physics and the FRITIOF model (Apostolakis et al., 2009b; Andersson et al., 1987) of hadron-nucleus and hadron-hadron interactions of particles with momenta $>$ 3–5 GeV/c. The standard electromagnetic physics includes ionization, Compton scattering, Bhabha–Möller scattering, Bremsstrahlung, pair production, annihilation, and gamma polarization. The upper limit of energies for the list is 10 PeV, and the lower limit is 0.99 keV. Allison et al. (2016) note that for the energy range 0.99 – 100 keV, the results might be up to 10% off with respect to the measured data provided by NIST XCOM Photon Cross Sections Database (Berger et al., 2010).

FTFP_BERT + EM option 3 or 4. This list is an extension of FTFP_BERT to the energies below 100 keV. **option3** provides accurate simulations of the electro-

[1] The corollary is that the simulation repeats itself in detail if the same seed is given to the random generator.

Table 1. Geant4 logical levels of simulation.

Level	Functional description
Run	The total number of particles to be simulated is divided between worker processes. The geometry is constructed. The sensitivity is assigned to geometrical volumes. All initial parameters are fixed before the run starts. The run concludes when all events have been concluded in all threads. The final dataset is ready by the end of the run.
Event	An incident particle is generated according to the particle source settings. The particle starts its way through the Geant4 World. An event concludes after the incident particle, and every secondary particle is either absorbed, decayed, or slowed down below the threshold. The total deposited energy is ready to read out by the end of the event.
Track	Geant4 navigates each particle through the simulation geometry. Each track is a continuous path of a particle that consists of steps. A daughter track can be instantiated by a physical process that produces secondary particles. A track stops upon particle stopping.
Step	A step is a two-point entity that is the finest grain of the simulation. The Monte Carlo engine chooses a physics process for the next interaction. It is possible to record the true incident angle of a particle for any detector or exact location of a physics process inside a volume at the step level.

magnetic processes recommended for medical and space science applications. The **option4** comprises the most accurate electromagnetic models and the finest model-relevant settings. Naturally, the latter uses more time for computation. However, the production and transport of optical photons are not included by default. To take into account Cerenkov radiation or scintillation and the plethora of optical processes such as Rayleigh scattering, refraction, and reflection, one has to add the Optical Physics module.

The optical processes construct a separate block of physics in Geant4. Photons are treated as particles, not waves; therefore, Geant4 can not simulate diffraction or other wave-related optical effects.

5.2.2 Simulation levels

Geant4 splits the simulation as a whole into a hierarchy of simulation levels. The division to the simulation levels is reflected in the logical structure of classes that a user can tune at each simulation stage. For a given task, one should limit the tuning to the level streamlined for the desired purpose. The hierarchy of the simulation is presented in Table 1.

5.2.3 Geometry and materials

Geant4 geometry is much like a set of drawings translated to a special language. Geant4 allows construction by primitive volumes, such as a bar, a cylinder, a sphere, etc. Each geometrical primitive is a shape-defining class that is combined with a material-defining class and a position-defining class to a logical volume. A built-in database of materials is provided to enhance the readability of the code. The basic primitives are shown in Figure 29. The instrument can be described by creating objects in C++ code, which can grow dramatically if fine details are essential for the simulation.

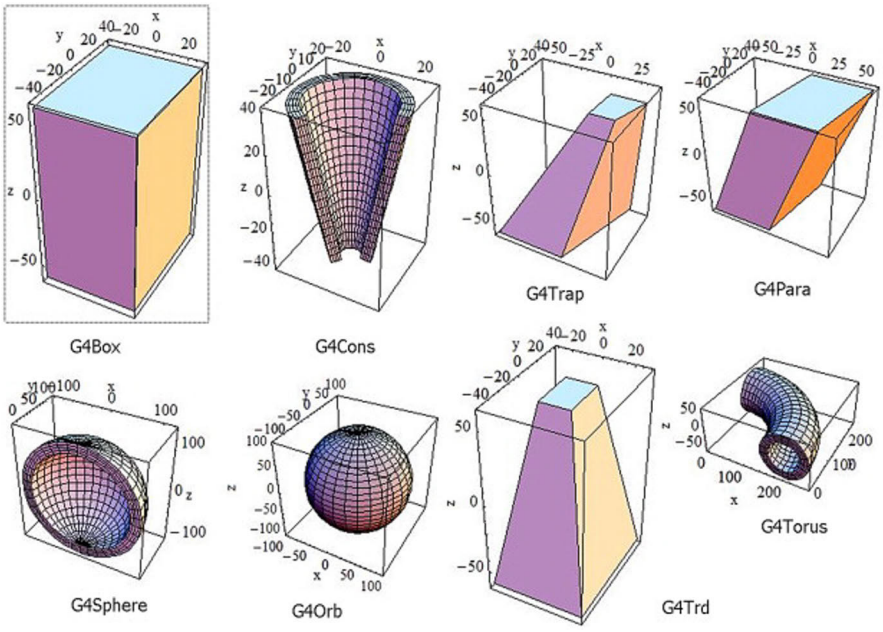

Figure 29. Basic geometry shapes defined by the Geant4 geometry classes. Each shape has a corresponding primitive in GDML. Used with permission from Elsevier, (Apostolakis et al., 2009a).

An alternative way to describe geometry is a Geometry Definition Markup Language (GDML) (Chytracek et al., 2006). The language is a CERN extension to standard XML. Elements of a detector must be hierarchically described within a GDML file, which holds comprehensive data on the dimensions and the position of each part and its material. GDML allows simple math and loops, which support a degree of automation, for example, to create multi-pixel detectors.

Materials in GDML are constructed from chemical elements. Elements are defined by their atomic number and atomic mass. Materials may have one or more elements; a mixture is defined by the elemental mass- or mole portion. Each material may have an arbitrary bulk density. This option allows for the usage of foam-like mass equivalent replacements for structures located away from the detector stack.

Their bulk can shadow the detectors, but their details are insignificant. For such a structure, the exact details would consume a lot of computing time while the effect on the detectors is negligible.

The simulations performed for the research in Papers I-IV used GDML models of particle instruments. These models were translated from 3D models used for the production of mechanical parts of spacecraft, the supporting structures, and enclosures of the instruments. These models reflect precise replicas of the instruments and surrounding structures. Parts of the models that are located distantly from the detectors were replaced by aluminum bars with the same mass to save computing time. The replaced parts consisted of light elements such as aluminum, carbon, oxygen, and chlorine by more than 95%; accordingly, such replacement was deemed valid. Any characteristic gammas from these parts are absorbed by surrounding structures or detector housing.

5.2.4 Particle sources

The space environment presents charged particles traveling in all directions. In the Van Allen radiation belts, the pitch angle distribution varies substantially across the magnetic field lines. We found it reasonable to simulate an isotropic distribution of particles and register the particles' incident angle that caused a hit in the instrument. The statistics is well enough to allow inhibition of a certain range of pitch angles; hence, an isotropic incidence appears to be an optimal level of generality in the simulation of dynamically changing space environment.

The isotropic distribution of particles is obtained by a spherical radiating surface, which sends particles inside itself. An excellent review on the correct particle generation for Monte Carlo simulations was written by Greenwood (2002). The Papers' I-IV simulations implemented radiating spheres with particle directions distributed by the cosine law[2]. The direction distribution is shown in Figure 30.

5.3 Data collection

The Geant4 itself has powerful analytical capabilities (Allison et al., 2016). The application can calculate accumulated quantities, such as dose or volume charge, using built-in classes and methods. Geant4 classes can produce tables and histograms of physical quantities, such as deposited energy in a distinct sensitive volume. However, these intrinsically enabled calculations are locked to the simulation process. In case a change is necessary for the accumulation method, the whole simulation has to be run anew. The work described in Paper III demanded tuning of the PATE particle classifier at the point when the simulation has already concluded. The author

[2] Also called Lambertian in optics.

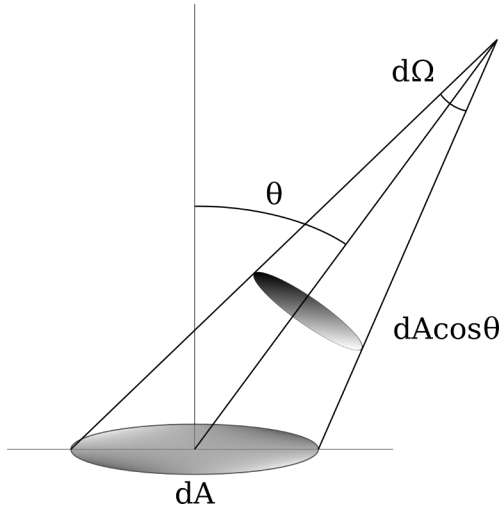

Figure 30. Cosine law intensity. The observed flux within $d\Omega$ is proportional to $\cos\theta$.

chose to collect raw data from the sensitive detectors and to post-process the data separately. Post-processing scripts use Python language and multi-processing.

5.3.1 Geant4 workflow

The simulations that made a foundation for the thesis produce numerical tables of records of deposited energies in the sensitive volumes (detectors).

The experimental setup consisted of an instrument model, a particle source, and additional structures, which were essential to reproduce the environment corresponding to the simulation. The model is placed inside the World volume, which is filled with hydrogen with the space vacuum density[3]. A particle source is either a sphere encompassing the instrument within or a flat circle that radiates particles normally to its plane.

A record[4] is put to the table if the deposited energy in any detector is above zero in the current event. The record has a separate field for the energy deposited by secondary particles to assess their influence. The record tables allow flexible analyses of the data for a single detector or any combination of them. One of the benefits is that a particle classifier can be iterated on the same data for each variant.

If a radiating surface emulates a uniform particle flux, the majority of simulated particles do not produce a record in the table. The number of simulated particles is usually in the order of billions, but their tracks do not touch detectors, which are relatively small compared to outer dimensions of RADMON and PATE. A generated

[3] Geant4 terminates a particle track if the volume density is zero.

[4] i.e., an n-tuple object

table with deposited energies resulted from particle hits contains about 10^4 – 10^6 usable records per run. Data size is larger for particles with higher incident energies since the collimators and shields reach their transparency limit.

The amount of particles to be simulated is chosen large enough to keep the statistical errors for the geometric factors within the range of 1–10%.

The Birks correction was not applied directly in the Geant4 simulation. It was previously speculated that Geant4 might demonstrate peculiar behavior of processes generating optical photons, including Birks correction to the scintillation light (Dietz-Laursonn, 2016). One of the significant points is that Geant4 applies Birks correction to energy deposits in steps, which may be larger than the lengths of significant changes in dE/dx. On the other hand, the correction is straightforward to apply for protons fully absorbed in the scintillator (see Section 3.2.3). The RADMON calibration relies on the registration of particles fully absorbed by the scintillator, i.e., those in the proton "banana" curve.

To cover a wide energy range in calculations of geometric factors, each simulation run had a narrow range of incident particle energies. The midpoint of the range is chosen on a logarithmically spaced grid. The energy distribution for each run is either single energy (a δ-function), or a boxcar distribution with two boundaries, equally spaced from midpoints on the logarithmic grid. The monoenergetic approach is more straightforward in realization; therefore, it is used for CubeSat instruments, e.g. by Johnson et al. (2020). It samples the geometric factor in the midpoint energy value, whereas a boxcar distribution emulates averaging by the Monte Carlo integration method. The possible difference is presented in figure 31 for a geometric factor rapidly changing with energy.

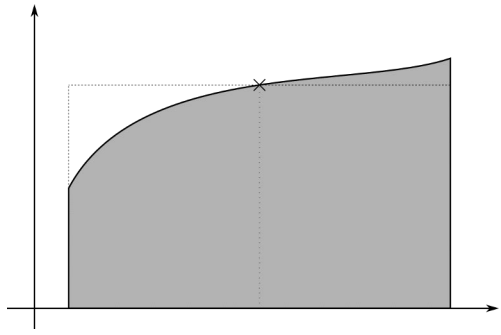

Figure 31. An illustration of the averaging error occurring if a function changes significantly across the energy bin.

Since RADMON has softer curves for geometric factors, its simulation energy grid has 64 bins per decade. Simulations for PATE were performed using the monoenergetic approach with 64 bins per decade at the first stage. To reveal the slopes of the geometric factors of its proton channels, the number of bins was raised to 256,

or about 0.4% in energy resolution. Finally, the instrument was simulated with 256 boxcar bins per decade.

5.3.2 Simulation results

The data from each run was systematically saved into separate files for further processing. Each file carried metadata on the particle species and their total count, the midpoint energy[5], and the serial number of the run. These data files were also used to assess pile-up effects in the detectors by my colleagues.

Particle tracking is a quite demanding task for a computer. Initial simulations that help ensure the model is correct and the preliminary results make sense were performed on a desktop machine. The "production" runs required massive computing power inaccessible on a personal computer. At various stages of the development, we have used Iphiclus, a multiprocessor machine in the Space Research Laboratory of the University of Turku, the Pleione cluster, and the Dione cluster, both located in the University of Turku. These large machines give an up to 1000 times increase in computing power compared to a desktop computer. A full simulation round covering several decades of energies usually took about two weeks to complete.

The simulations required large disk space ($\sim$ 100 Gb) to store raw hits data. We have used storage on the clusters to keep and process the data. The processing was initially done on the local office PC but later was moved to clusters to benefit from the number of cores available. Most of the tasks on the data processing and visualization of results were programmed in Python 3. The tasks were split into independent threads in fully parallel mode.

The geometric factors for the instrument channels were calculated from the data according to Sullivan (1971). A model of an instrument was placed inside a spherical radiating surface. The geometric factor of an instrument being simulated is obtained by the equation:

$$G = \pi \frac{N_d A_0}{N_0}; \qquad \sigma_G = \pi \frac{\sqrt{N_d} A_0}{N_0}, \tag{27}$$

where G is the geometric factor, σ_G is its statistical deviation, N_d is the number of detected particles, N_0 is the total number of simulated particles, and A_0 is the area of the radiating sphere. The equation (27) is also correct for N_d counted for a specific range of energy or solid angle or an instrument channel.

A response function calculated for a specific environment is a two-dimensional table of geometric factors evaluated for the particle population in the selected environment for each instrument channel in multiple narrow energy bins $\{\Psi_{ik}\}$, where i is the channel index, k is the number of the energy bin. The table with the central

[5] the upper and lower bounds were added in the final simulation.

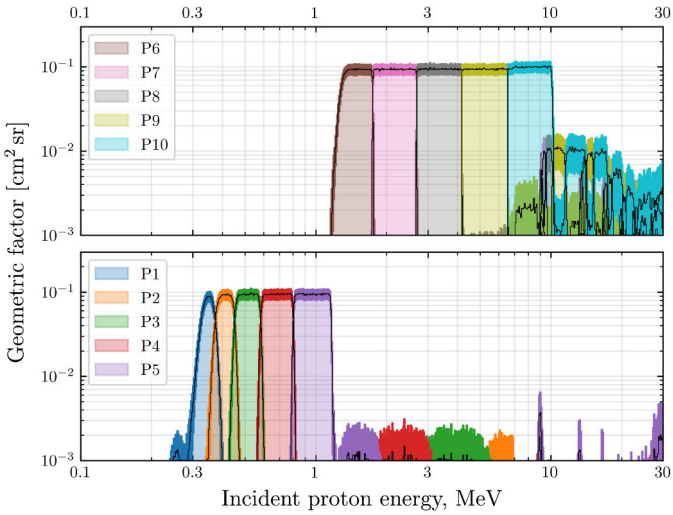

Figure 32. The response functions of ten PATE proton channels shown in black solid lines, vivid color outline present a 3-σ statistical error.

energies in each energy bin is also stored along $\{\Psi_{ik}\}_j$. The response function calculated for the space environment is a set of tables of geometric factors evaluated for the isotropic flux of each particle species for each instrument channel $\{\Psi_{ik}\}_j$, where i is the channel index, k is the number of the energy bin, and j is the particle species. Figure 32 shows an example of graphical representation of the response function $\{\Psi_{ik}\}$ obtained for an isotropic incident flux of protons as measured by PATE proton channels; 256 energy bins per decade are shown.

5.3.3 Bow-tie analysis

The "bow-tie" analysis aims to obtain effective geometric factors and characteristic energies for instrument channels that do not necessarily have a boxcar or step-like shape of their energy response functions. It was first introduced by Van Allen et al. (1974) to describe a particle detector response onboard Pioneer-10 spacecraft.

Particles are classified into instrument channels depending both on energy deposited in the detectors of the instrument and on the combination of the detectors that had a hit. An ideal response function would look like a boxcar or step function, depending on the energy condition. Scattering blurs the edges of the response, if the scattered particle is not absorbed in detectors but elsewhere and consequently, only a part of the energy gets registered.

The bow-tie analysis scans the response with modeled power-law spectra within a certain range. Specific energy would have the same geometric factor for all spectral shapes, and there is most probable energy where it happens.

A single channel response function is folded with power-law incident differential particle spectra $f(E) = AE^{-\gamma}$ with several indices. The range of γ indices must correspond to a physically reasonable range of spectral slopes that is likely to be observed by the instrument. A pair of values for geometric factor and effective channel energy is found by matching the results for different γ indices. The analysis details depend on whether the instrument channel is a differential or an integral one, but the ideas are pretty similar.

Bow-tie analysis for a differential channel

The "bow-tie" analysis probes the acceptance of a differential channel to the power-law spectra $f(E) = AE^{-\gamma}$ of particles, where γ power indices lie within a certain range. The goal is to find a pair of values for the central energy and geometric factor that the channel would have if it had an ideal boxcar function for the energy response.

$$f(E_{\text{eff}}) = \frac{C}{G\delta E}\,, \tag{28}$$

where E_{eff} is the effective energy of the channel, $f(E)$ is the incoming particle flux density, C is the observed count rate in the channel, and $G\delta E$ [$\text{cm}^2\,\text{sr}\,\text{MeV}$] is the effective geometric factor obtained by the bow-tie analysis of the channel response function $\Psi(E)$ is defined as:

$$G\delta E = \frac{\int_0^\infty f(E')\,\Psi(E')\,\mathrm{d}E'}{f(E_{\text{eff}})}\,, \tag{29}$$

In case the energy response function of a differential channel has a single distinct peak above the plateau, the effective geometric factor of the channel is practically constant for particles of energies around the peak.

To illustrate the method, let us consider an ideal differential energy channel with a boxcar response.

$$G_b(E) = G_0(H(E - E_l) - H(E - E_h))\,, \tag{30}$$

where $H(x)$ is the Heaviside step function, E_l and E_h are the lower and the upper energy cuts of the channel, and G_0 is a constant that represents the geometric factor of the instrument for particles of energies between E_l and E_h.

Let us assume that the channel is narrow and replace E_l with $E_0(1-\alpha)$ and E_h with $E_0(1+\alpha)$, $\alpha \ll 1$. If we plug the values in (29) and calculate the effective differential geometric factor of the channel we get

$$G\delta E = \frac{\int_0^\infty f(E')\,\Psi_b(E')\,\mathrm{d}E'}{f(E_{\text{eff}})} = \frac{\int_{E_0(1-\alpha)}^{E_0(1+\alpha)} AE'^{-\gamma} G_0\,\mathrm{d}E'}{AE_{\text{eff}}^{-\gamma}} \tag{31}$$

If we take the integral and use the assumption of $\alpha \ll 1$ to linearize the equation by α, we obtain a function that is constant for any γ if $E_{\rm eff} = E_0$.

$$\begin{aligned} G\delta E(\gamma, E_{\rm eff}) &= G_0 \frac{E_0^{-\gamma}}{E_{\rm eff}^{-\gamma}} \frac{E_0((1+\alpha)^{-\gamma+1} - (1-\alpha)^{-\gamma+1})}{-\gamma+1} \\ &\approx G_0 \frac{E_0^{-\gamma}}{E_{\rm eff}^{-\gamma}} \frac{E_0(1+\alpha(1-\gamma) - 1 + \alpha(1-\gamma))}{1-\gamma} \\ &= 2\alpha E_0 G_0 \frac{E_0^{-\gamma}}{E_{\rm eff}^{-\gamma}} = \Delta E_0 G_0 \left(\frac{E_0}{E_{\rm eff}}\right)^{-\gamma}, \end{aligned} \tag{32}$$

where $\Delta E_0 = 2\alpha E_0$ is the channel width. Obtained $G\delta E$ is constant for any γ if $E_{\rm eff} = E_0$.

An energy response of a realistic instrument channel usually resembles a smoothed, somewhat broadened boxcar function. For such a response function, the $E_{\rm eff}$ depends on the choice of the range of γ indices. Widening of the peak and smoothed edges make $G\delta E$ deviate a little from a constant value as γ index changes even at the $E_{\rm eff}$.

Figure 33 shows an example of a "bow-tie" formed by a family of functions given by (29). The neck of the "bow-tie" has a non-zero thickness, which indicates that the response function $\Psi(E)$ has smooth slopes. To account for this deviation, we utilize a statistical criterion to find the $E_{\rm eff}$ as the energy with a minimum standard deviation of the values of $\{G\delta E(\gamma_k, E_{\rm eff})\}$ at fixed energy within the used sequence of $\{\gamma_k\}$ indices. The obtained $E_{\rm eff}$ is accepted as an exact value. $G\delta E$ is then defined to be within an interval given by $[0.05 \ldots 0.95]$ percentiles of its distribution at $E_{\rm eff}$ in respect to $\{\gamma_k\}$ indices taken to be uniformly distributed between limiting values.

Bow-tie analysis for an integral channel

An integral channel is analyzed similarly. First, we generate modeled power-law spectra $f(E) = AE^{-\gamma}$ within a certain range of γ power indices. Next, we probe the acceptance of the channel to the spectra to find a pair of values for the threshold energy and geometric factor that the channel would have if it had a Heaviside step function for the energy response.

$$F(E > E_{\rm thr}) = \frac{C}{G_I}, \tag{33}$$

where $E_{\rm thr}$ is the threshold energy of the channel, $F(E > E_0)$ is the integral flux of incoming particles, C is the observed count rate in the channel, and G_I [cm^2 sr] is the effective geometric factor obtained by the bow-tie analysis. The geometric factor G_I is defined as:

$$G_I(E_{\rm eff}) = \frac{\int_0^\infty f(E')\,\Psi(E')\,{\rm d}E'}{\int_{E_{\rm eff}}^\infty f(E'')\,{\rm d}E''}, \tag{34}$$

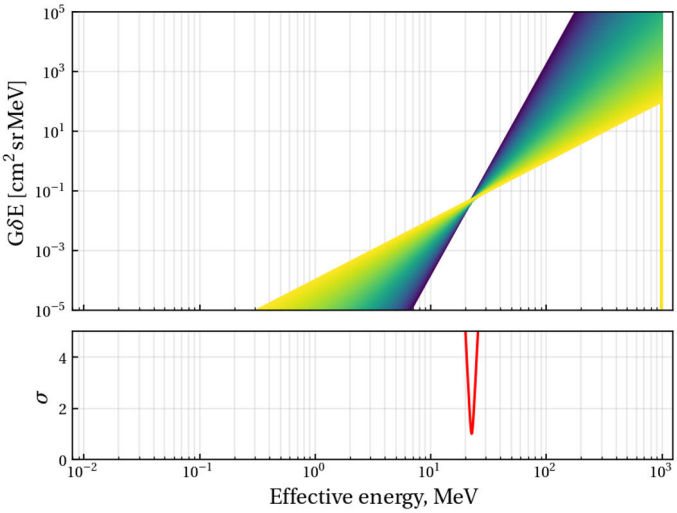

Figure 33. An example of a "bow-tie" formed by folding modeled spectra with a range of indices $\{\gamma_k\} \in [-1.5 \cdots -3.5]$ with a response function of the P8 proton channel of the BepiColombo/SIXS-P instrument. The lower panel shows the statistical measure of the "bow-tie" spreading in standard deviation units normalized to the deviation of $G\delta E$ at E_{eff} for the channel, (Huovelin et al., 2020).

where $f(E)$ is a modeled power-law differential flux, and E_{eff} is the effective threshold energy. In case a channel can be characterized as an integral one, $G_I(E_{\text{eff}})$ is practically constant for a range of power-law indices of $f(E)$.

To illustrate this method, let us consider an ideal integral energy channel with a step response.

$$\Psi(E) = G_0 H(E - E_{\text{thr}}) \,, \tag{35}$$

where $H(x)$ is the Heaviside step function, E_{thr} is the threshold energy. Let us plug the response into (34):

$$\begin{aligned} G_I(E_{\text{eff}}) &= \frac{\int_0^\infty f(E')\,\Psi(E')\,\mathrm{d}E'}{\int_{E_{\text{eff}}}^\infty f(E'')\,\mathrm{d}E''} \\ &= \frac{\int_0^\infty f(E') G_0 H(E' - E_{\text{thr}})\,\mathrm{d}E'}{\int_{E_{\text{eff}}}^\infty f(E'')\,\mathrm{d}E''} \\ &= G_0 \frac{\int_{E_{\text{thr}}}^\infty f(E')\,\mathrm{d}E'}{\int_{E_{\text{eff}}}^\infty f(E'')\,\mathrm{d}E''} \,, \end{aligned} \tag{36}$$

which equals to G_0 if $E_{\text{eff}} = E_{\text{thr}}$. In the strict sense the exact shape of the model spectrum is of a less importance for an integral channel than for a differential one, but we use the same power-law spectra as for differential channels.

A realistic integral channel has a smoothed step-like response, which contributes to the spread of a bow-tie given by a family of functions described by (34). Therefore,

the statistical procedure described earlier for a differential channel is necessary to determine an exact value of E_{thr} and a value with a margin for the G_I.

6 Summary of the original publications

6.1 Paper I.

Oleynik, P., Vainio, R., Punkkinen, A., Dudnik, O., Gieseler, J., Hedman, H., Hietala, H., Hæggström, E., Niemelä, P., Peltonen, J., Praks, J., Punkkinen, R., Säntti, T., and Valtonen, E. (2020). Calibration of RADMON Radiation Monitor Onboard Aalto-1 CubeSat. *Advances in Space Research*, 66(1):42–51

The article summarizes the results of several tasks dedicated to the calibration of RADMON, a tiny radiation monitor onboard Aalto-1, the first Finnish CubeSat (Peltonen et al., 2014). The radiation monitor was developed by students of the University of Helsinki and the University of Turku. It has exceeded its original scientific objective to become a miniature particle instrument in the low-Earth orbit. Figure 34 reproduces Figure 1 from Paper I and shows the RADMON instrument.

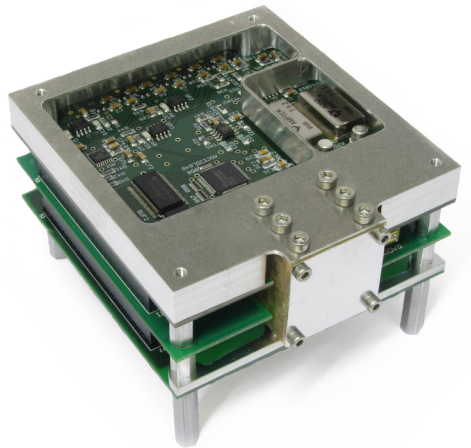

Figure 34. A photo of RADMON instrument. The top PCB with preamplifiers and ADCs is visible. Image credit: Arttu Punkkinen.

The article has a brief description of RADMON, focusing on details concerning the instrument detectors' physical properties and supporting parts.

A GDML[1] model of the instrument was constructed. We have constructed a

[1] See section 5.2.3

GDML model of Aalto-1 spacecraft as well to provide a comprehensive simulation. The modeled assembly originates from the realistic spacecraft model produced in mechanical CAD software. Due to differences in data formats, the physical volume boundaries were transformed into tessellated surfaces. This approximation by many triangular faces keeps the tolerances on the same level as most of the machined parts have. The detector stack elements and the sensitive detectors themselves were machined more precisely than the rest of the construction. Therefore, they were replaced with basic geometrical shapes (true cylinders, cubes, extrusions, etc.) in the model.

The model was put into a spherical radiating envelope, which mimicked the space environment. We have simulated an environment filled with protons and electrons. Each simulation run utilized the single energy of the incident particles. Based on the Geant4 package, the simulation software implemented the ΔE–E coincidence logic. The rest of the logic comprised a set of Python scripts. We have calibrated the gains of the detectors by comparison of the simulated data with the orbital data. Best fit values were found for the gains of silicon and scintillation detector. These values allowed us to calculate realistic response curves for all particle channels of the instrument.

To make the data product more useful, we have calculated effective energies for the particle channels using Van Allen's bow-tie method described in section 5.3.3. The obtained values were used in Paper II.

6.2 Paper II.

Radiation Monitor RADMON aboard Aalto-1 CubeSat: First results. Gieseler, J., Oleynik, P., Hietala, H., Vainio, R., Hedman, H.-P., Peltonen, J., Punkkinen, A., Punkkinen, R., Säntti, T., Hæggström, E., Praks, J., Niemelä, P., Riwanto, B., Jovanovic, N., and Mughal, M. R. (2020). Radiation Monitor RADMON aboard Aalto-1 CubeSat: First results. *Advances in Space Research*, 66(1):52–65

The article presents the RADMON observations in the period of October 2017 – May 2018. The observation data were made available as an electronic database. The database has nearly continuous coverage from October to December 2017, plus smaller periods in January, April, and May 2018. The daily observation time in hours is shown in Figure 35

We present electron and proton intensity maps in geographic and AACGM (Shepherd, 2014) geomagnetic coordinates in Chapter 3. The maps for electron channel E2 show the integral intensity of electrons in the high latitude regions where the outer radiation belt reaches the altitude of the Aalto-1 orbit. The proton channel data shows the region of the SAA. We also discuss the proton contamination of electron channels observed in orbit.

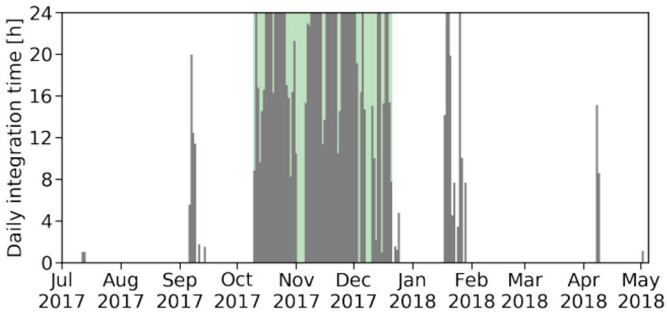

Figure 35. The daily measurement time of RADMON. The green shading indicates the observations period discussed in Paper II.

Chapter 4 provides an analysis of the magnetosphere dynamics observed. We show the dynamics in energy and magnetic (with respect to L-parameter) domains.

The observed dynamics is compared to the results of the PROBA-V/EPT mission in Chapter 5. We compare data of the two missions during the same time interval. A reasonable correlation between the two instruments is presented. We discuss the differences and present a spectral comparison of the integral electron spectrum from 9 to 20 Nov 2017 selected in $3.75 < \mathrm{L} < 5.25$. A spatial comparison of observed electron fluxes with respect to L-coordinates supports the consistency of the observational data of RADMON and PROBA-V/EPT.

6.3 Paper III.

Oleynik, P., Vainio, R., Hedman, H.-P., Punkkinen, A., Punkkinen, R., Salomaa, L., Säntti, T., Tuominen, J., Virtanen, P., Bosser, A., Janhunen, P., Kilpua, E., Palmroth, M., Praks, J., Slavinskis, A., Kakakhel, S. R., Peltonen, J., Plosila, J., Tammi, J., Tenhunen, H., and Westerlund, T. (2020). Particle Telescope aboard FORESAIL-1: simulated performance. *Advances in Space Research*, 66(1):29–41

The article provides an overview of the Particle Telescope (PATE) being developed for the Foresail-1 CubeSat mission in low-Earth orbit. Foresail-1 is the first of three spacecraft developed by the Finnish Centre of Excellence for Sustainable Space (FORESAIL). It is a 3-unit CubeSat with dimensions of $10 \times 10 \times 34\,\mathrm{cm}^3$ and a mass of about 4 kilogram. The spacecraft carries PATE and a plasma brake payload. The latter is designed to lower the satellite orbit to enable particle observations with a drifting magnetic local time. The initial orbit will be a Sun-synchronous with an altitude of about 600 km. The spacecraft is spin-stabilized with the axis of rotation pointing to the Sun. The rotation period is 15 seconds per revolution. Figure 36 shows the internal composition of the instrument.

Section 3 of the article describes the overall design of the instrument consisting

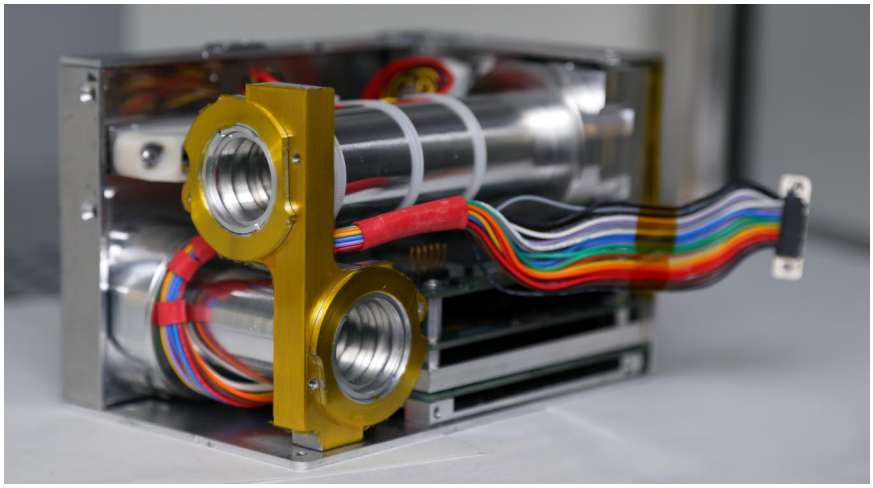

Figure 36. PATE engineering qualification model without the cover at the final stage of assembly.

of two telescopes with identical detector stacks. The first telescope is mounted perpendicularly to the spacecraft rotation axis. It scans the pitch-angle distribution of electrons with a resolution of 32 time-domain separated sectors per revolution. The second telescope is mounted along the spacecraft rotation axis, pointing to the Sun. It aims at observing energetic neutral atoms (ENA) arriving from the Sun undeflected by the Earth magnetic field.

Section 4 presents the Geant4 model of the instrument and the signal path model for the particle classifier.

Section 5 discusses the results of the simulations. We have obtained the energy response curves for all instrument channels. In addition, we have considered possible contamination of electron channels by energetic protons and proton channels by electrons of moderate energies. The angular pattern of acceptance for protons and electrons is also presented in Section 5.

We discuss the possible count rates along the orbit using the calculated geometric factors of PATE and models of orbital particle intensities AP-8 and AE-8 for protons and electrons, respectively. This analysis gives estimates on the feasible highest count rates in orbit due to trapped particle populations. The results assure that the count rate is within the limits of well-resolved pulse counting.

The estimates on possible counting rates for Solar ENAs are based on the STEREO observations published by Mewaldt et al. (2009). Our estimate is about 300 counts from ENAs from a similar event, which is well above modeled background in equatorial regions of the orbit.

6.4 Paper IV.

Mughal, M. R., Praks, J., Vainio, R., Janhunen, P., Envall, J., Näsilä, A., Oleynik, P., Niemelä, P., Slavinskis, A., Gieseler, J., Jovanovic, N., Riwanto, B., Toivanen, P., Leppinen, H., Tikka, T., Punkkinen, A., Punkkinen, R., Hedman, H.-P., Lill, J.-O., and Slotte, J. (2021). "Aalto-1, multi-payload CubeSat: In-orbit results and lessons learned". *Acta Astronautica*, 187:557–568

The article summarizes the science and technology results of the Aalto-1 mission. We discuss the achievements and lessons learned from the mission, which are organized by subsystem. The spacecraft was designed by many people interacting with each other. This cooperation revealed to be successful; multiple goals were achieved during the mission. Issues that surfaced in space challenged the authors, but most of them were resolved. In the article, we propose ways to improve the design of subsystems and scientific payloads.

The author's contribution to this article is a discussion in Chapter 4 of the lessons learned during the operation of RADMON.

First, we discuss the mechanical construction of the detector stack. An alternative shape of the entrance shaft could make the instrument response sharper for particles nearly penetrating the instrument brass case. The opening in the brass case has straight walls, but the acceptance of the detector stack is within a cone of approximately 20°. Thus, the effective thickness of the shielding depends on the incident angle in relation to the instrument axis. A varying effective thickness alters the shape of the instrument response; therefore, the angle-integrated response curve has shallower slopes in the energy domain. A streamlined conical entrance shaft would sharpen the edges of the response curves for all particle channels.

Second, we discuss the geometry of the ΔE detector, which has a rather small width to thickness ratio. A low aspect ratio of the detector combined with a rather large opening in the brass envelope increases the chances of an "edge hit" for the silicon detector. It occurs if a particle incident with an angle to the instrument axis traverses through an edge of the silicon detector and reaches the scintillator triggering the coincidence logic. This edge effect causes broadening of the response curves, which could be quenched if the silicon detector had two layers, one for triggering with a thickness of 100 – 150 µm, and the second as ΔE detector. This "sandwich" structure might inhibit the contamination of electron channels by high-energy protons in the SAA.

7 Discussion

7.1 Research findings in brief

The presented research uses Monte Carlo simulations to characterize two charged particle instruments. We simulate the space environment as an isotropic particle flux, which demands computing power orders of magnitude larger than a simulation of a beam at an accelerator facility. One may argue that the instrument calibration is well achievable solely with an accelerator beam, so what would make a meaningful difference?

A proper characterization of an instrument demands a good knowledge of how the instrument succeeds in particle detection and what kind of undesired behavior the instrument may show. We have shown that cross-species contamination may affect the measurements and, therefore, the scientific conclusions arising from the data analysis. Such a contamination is found to be mostly caused by particles incident outside the nominal solid angle with energies beyond the nominal energy range of an instrument.

We analyze what kind of contamination one would expect in space from, e.g., high energy protons of the inner Van Allen radiation belt. This analysis is rarely performed for CubeSat instruments, possibly because there is no reasonable way to reproduce the space environment on the ground to match the observed behavior with the simulations. Paper I and III discuss how each particle instrument detects target particle species in dedicated particle channels and how the particle species interfere the measurements in a mixed environment. The way to disentangle the influence of protons and electrons to a measurement in a mixed environment is to be described in the future publications.

In the Thesis, the author argues that once a Geant4 model has been verified in a specific environment, the model might be used to assess the instrument performance in another environment, eventually, in space. In four Papers comprising the Thesis, we demonstrate the effectiveness of Geant4 Monte Carlo simulations of charged particle fluxes in the characterization of particle instruments with minimal demand for ground-based facilities. Paper I shows the in-flight calibration using the natural proton source in space, the trapped proton population in the inner radiation belt. The same technique we should apply for the PATE particle telescope when it is in orbit to confirm the calibration obtained on the ground. Paper III sets the initial point of such in-flight confirmation for PATE.

Paper II discusses cross-calibration of Aalto-1/RADMON with Proba-V/EPT using the dynamics of the trapped electron population in the outer belt observed by two instruments in low-Earth orbit at high latitudes. The research demonstrates the scientific use of the calibration parameters obtained in simulations. A successful comparison of two independently built devices enhances trust in the data product the same way a scientific article benefits from an independent peer review. In the next chapter 8 we present a possible cross-calibration pair for PATE, the POES/MEPED particle telescope.

7.2 Software

The research resulted in the Papers comprising the Thesis have been performed two years ago, in 2019. During the last two years, the author developed simulation techniques and software to achieve excellence in research.

Both particle instruments described in the Thesis were simulated using a custom Geant4-based application with a custom output data format. One of the benefits of this approach is the minimal time required to write and verify the software. Though, such an approach could not be sustainable in the long run. If a feature must be added to simulations, it takes a bit of effort to apply the changes to each instrument-specific code. Another drawback is that the analysis tools are automatically limited to be instrument-specific.

Another possible solution could be GRAS[1] software maintained by ESA (Santin et al., 2005). The code incorporates simulation setup, the Monte Carlo engine, and flexible analysis tools. The analysis tools are C++ classes that include ready modules to calculate the dose, volume charge, and non-ionizing radiation damage. A custom GRAS analysis module could produce the event-based data, but creating own code from the existing templates seemed a shorter way to proceed.

7.2.1 Author's simulation code

A new code was developed to address the drawbacks of the instrument-specific code. From custom applications for each particular case, a universal simulation code emerged[2]. The core idea of yet another Geant4-based software is to allow a user, unskilled in C++, to simulate arbitrary complex geometries with an arbitrary number of readout points. The particle tracking task, which requires a lot of computing power, was isolated from everything else to save time used on computing clusters. The isolation of the Monte Carlo task also allowed the most time-demanding code to benefit from distributed parallel computing.

The code unified the simulation workflow from setup to the data analysis so that

[1] A General-Purpose 3-D Modular Simulation Tool for Space Environment Effects Analysis.

[2] https://github.com/phirippu/instrument-simulation

the data processing software follows the suit of unification, which allows better reuse of existing, tested software. The Geant4 part does only the particle tracking, leaving the rest to post-processing, making it flexible. One of the software applications is to create a volume map of expected ionizing dose inside an envelope of complex shape, which is essential for the engineering of space instruments exposed to an environment rich with energetic charged particles. If such code existed by the time of writing the Papers, it would have reduced the net effort.

7.2.2 Geometry definition

The geometry models used in the presented Thesis were initially developed as CAD mechanical models used in mechanical production. Each CAD software stores information about the geometric shapes and their positions in their own binary format, which is best suited for the mechanical design. However, it is not straightforward to convert the stored complex shapes into basic shapes recognizable in Geant4 (GDML, see 5). In Papers I and III, we have used a proprietary conversion tool, which translates CAD geometry descriptions to GDML files. The tool does not translate materials nor human-readable names of parts from the CAD data. Every surface becomes tessellated after the conversion, i.e., triangular faces forming a 3D part body. While this tessellation process produced decent accuracy from the mechanical point of view, the simulation model required manual adjustments.

Each detector consists of several areas, or volumes, playing certain roles in the instrument functionality. The areas are touching each other, e.g., a guard ring around the active area or a passive area between two active regions. Each volume still has the same thickness as the neighboring one, which is essential for accounting for the energy lost by a particle on its way through a detector or detector stack. When tessellated, curved boundaries of these volumes are no longer touching each other but either make a gap or overlap. The effect is minuscule yet significant when the simulation results are compared to experimental data obtained at an accelerator facility. A gap between two detector areas would allow some particles to see the given detector layer as a thinner one, which leads to unrealistic energy deposits in subsequent layers. An overlap would cause the Geant4 engine to push a particle outside the overlapping space, leading to errors in accounting for the deposited energy.

To mitigate the distortion of the detector shapes by tessellation, the detectors in the GDML model were manually replaced with cylinders, rings, and other shapes with smooth borders touching each other the same way as in the instrument detectors. The other volumes were not manually adjusted since the precise energy deposited in passive material does not affect the particle detection.

In 2020, a new CAD-to-GDML conversion tool, PYG4OMETRY, has matured enough to try it as an alternative. The tool uses STEP (Standard for the Exchange of Product Data) files as input and produces GDML with finer grids used for curved

surfaces. The observed accuracy is enough to keep the detectors tessellated since the gaps and overlaps are in the nanometer domain. The tool was not used for any of the Papers in the Thesis; however, it might have saved much effort if it was available in the present state when we have been constructing models for RADMON and PATE.

7.3 Instruments

7.3.1 PATE and POES/MEPED

This section briefly compares the electron telescope of POES/MEPED and the electron channels of the PATE particle telescope. The instruments will observe the same high-latitude regions of the radiation belts, PATE being in a little lower orbit. Their scientific objectives match in observations of the radiation belts' dynamics. Both instruments will be operational in the same period since MEPED instruments are installed on five operational weather satellites from NOAA and MetOp series. It is expected that the data from two experiments can be compared, and a cross-calibration might be achieved.

A composed plot of geometric factors vs. energy for electron channels of both instruments is presented in Figure 37. Channels E1 and E2 of PATE resolve the spectrum in the low-energy end, covered by the E1 channel of MEPED. Channels E3 – E5 of PATE resolve the part of the spectrum observed in channel E2. The last two channels of PATE, though practically integral, will improve the energy resolution of observations compared to MEPED.

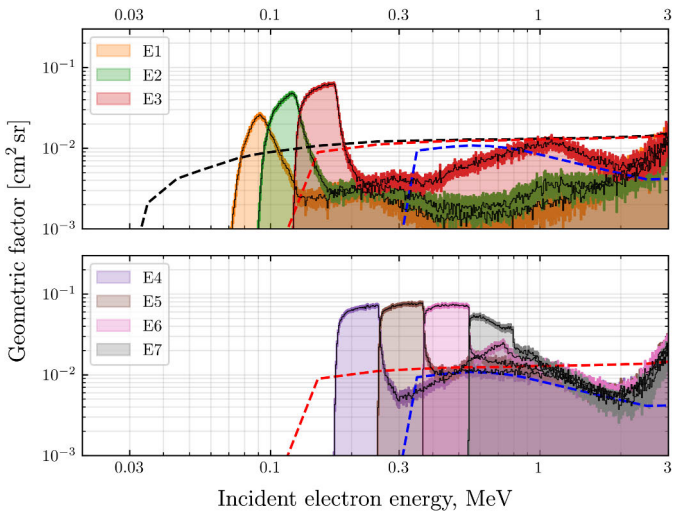

Figure 37. The response functions of PATE and POES/MEPED. PATE channels E1 – E7 are presented in filled curves, MEPED electron channels E1 (black), E2 (red), and E3 (blue) are presented in dashed curves.

A result from Asikainen (2019) is presented in Figure 38, which shows a combined history of observations of electron particle dynamics acquired by MEPED electron telescopes from 1979 to 2019. The plot shows data for 90° instrument, a similar plot exists for the 0° one.

The observations in two pitch angles by each telescope warrant observations with an enhanced angular resolution in pitch angle. PATE will have 32 sectors of pitch-angle for electrons in the outer radiation belt, which brings a new dimension to the measurements. The knowledge of the detailed shape of the pitch-angle distribution will advance our understanding of the electron acceleration and loss mechanisms in the outer belt. PATE observations should bring light to the details of relativistic electron precipitation to the upper atmosphere.

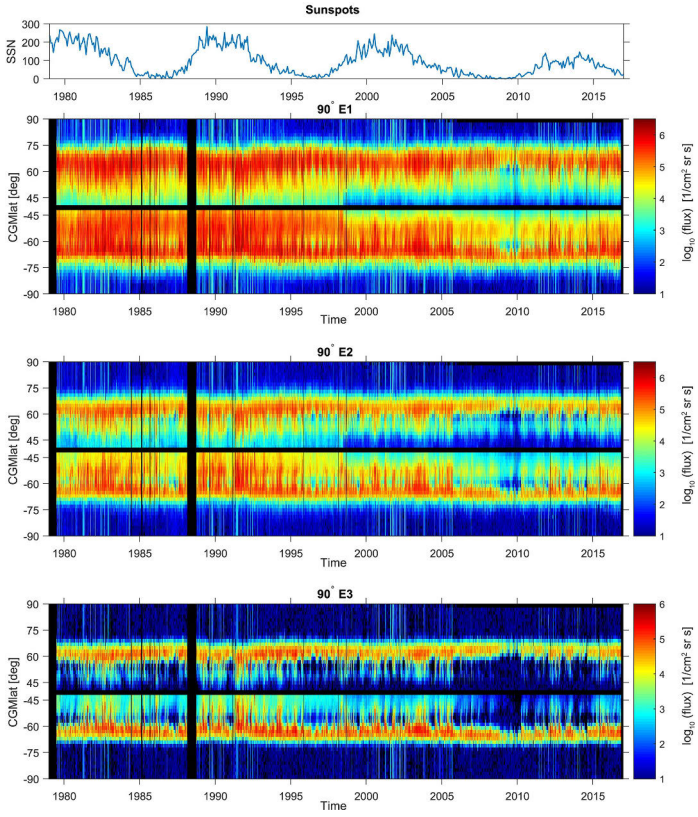

Figure 38. A composite of electron fluxes cleaned from background noise and normalized for magnetic local time driftof the satellite orbital planes. The composite has been computed using the data from the 90° telescope of NOAA-6, NOAA-8, NOAA-10, NOAA-12, and NOAA-15 satellites. The fluxes in both hemispheres have been averaged over the two opposite magnetic local time sectors sampled by the satellites. Panels from top to bottom depict the monthly sunspot number (SSN) as a reference and the E1, E2, and E3 energy channels, respectively. The image and the original caption is obtained with the permission of American Geophysical Union ©2019. Asikainen (2019)

8 Conclusion and the future prospects

The presented work has demonstrated the use of Monte Carlo simulations to verify the performance of miniature charged particle instruments designed for space. The simulations with Geant4 are a standard tool[1] for the design and optimization of ground-based accelerator facilities, beam therapy devices and large space instruments. The design of CubeSat instruments also includes Geant4 simulations as mentioned in Section Referenced space missions, though for some missions, the simulated environments are restricted to particle beams.

One of the aims of the presented research is to adopt the practice of publishing papers describing the design, development, and verification of traditional, big space missions to the CubeSat ecosystem. In particular, such an approach should be adopted for small charged particle instruments. Section 4.3 briefly describes several nano-size space missions with charged particle instruments and highlights the existing incompleteness in the published research. Unlike the early CubeSat practice, the success of each mission is not final when the satellite orbits the Earth and reasonably communicates with the ground. The mission data has to be trusted, which requires an open and thorough description of the mission payloads. It was demonstrated that CubeSats are capable of carrying modern, compact, low-power space instruments (Poghosyan and Golkar, 2017). Therefore, it is essential to create examples of solid research on the properties of CubeSat instruments to present the scientific benefits of nanosatellite missions coexisting along with undoubtedly lower cost and reduced development time.

Kestilä et al. (2013); Peltonen et al. (2014), the Papers I, II, and IV are an example of sustainable development of a space instrument from the mission design phase to the lessons learned from the mission. The series of the published papers gives a comprehensive overview of the performance of RADMON and provides insight into the effects influencing the measurements that propagate to the data product.

A fresh thread of the research publications describing the Foresail-1 CubeSat mission and the PATE telescope is started by Papers A and III. PATE is several required tests away from the launch into the low-Earth orbit. We will describe the results and findings of the test campaign in an instrument paper currently in preparation.

[1] https://geant4.web.cern.ch/publications

In the following short sections, the author wants to describe the future work that continues the research presented in the Thesis.

8.1 Ongoing and future operations of RADMON

The RADMON measurement campaign presented in Paper II and the lessons learned presented in Paper IV warranted a new observation period. The Covid-19 lockdown of 2020 inhibited RADMON operations, but already in November 2020, the operations have been restarted with a new in-orbit calibration campaign. The radiation monitor was in calibration mode for several days. With a bliss of luck, RADMON calibration data yielded a prominent proton curve formed by protons of energies between 10 and 30 MeV, see Figure 40. Figure 39 shows reference calibration data taken in 2017. The calibration data in both cases are collected inside SAA. In 2020 the orbit crossed SAA so that RADMON detected more protons of energies above 30 MeV compared to the measurement in 2017. However, the position and shape of the proton curve are reproduced approximately the same in both cases. The position of the curve confirms that RADMON detectors are insignificantly aged, and the instrument is capable of further observations. Despite three years in a radiation environment, the instrument functions are within the margin.

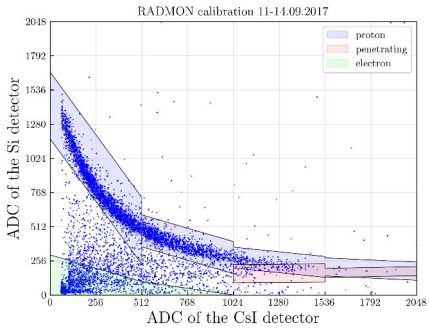

Figure 39. RADMON pulse-height data in 2017.

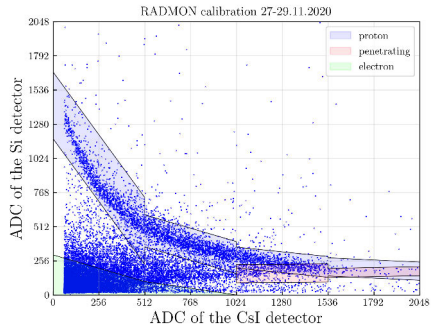

Figure 40. RADMON pulse-height data in 2020.

One of the issues onboard Aalto-1 is high-frequency interference that forced to raise the threshold of the scintillation detector of RADMON right after the launch. The RADMON measurements presented in Paper II exclude the E1 channel due to the very narrow energy range and small geometric factor that are the reasons for E1 to have too few counts. The electromagnetic interference appears periodic, which allowed mitigating its influence by adjusting the length of a digital filter used to process the current pulse from the scintillator readout. The energy threshold of the scintillation detector has been lowered by half, which allowed the first electron channel E1 to have a significantly wider energy range. The preliminary analysis

of the test measurements in orbit demonstrated a count rate in E1 comparable to E2, which suggests that the response of the E1 channel has been extended to the energies of slightly above 1 MeV. The updated response function is to be calculated and analyzed in future work to enable new observation runs.

8.2 Relativistic Electron and Proton Experiment

Relativistic Electron and Proton Experiment (REPE) is part of the Foresail-2 mission to the densest regions of the outer van Allen radiation belt. The instrument is to measure electron and proton spectra and to monitor the dynamics of the Earth radiation belts. The Foresail-2 mission is a 6U CubeSat carrying three scientific instruments, REPE, a fluxgate magnetometer on a deploying boom with a length of 60 cm, and a plasma tether experiment. The satellite will be launched into a geostationary transfer orbit with a perigee of about several hundred kilometers and an apogee of about 36000 kilometers. The satellite will cross the outer and the inner radiation belt twice in each orbit with a duration of 10.8 hours. The orbit provides repeated coverage in L-shell coordinates essential for monitoring charged particle acceleration and loss dynamics.

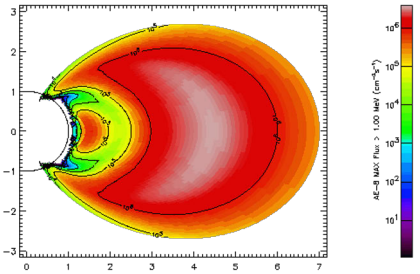

Figure 41. Electrons in AE-8. Image credit: SPENVIS (Heynderickx et al., 2004).

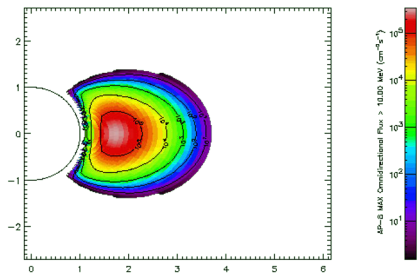

Figure 42. Protons in AP-8. Image credit: SPENVIS (Heynderickx et al., 2004).

Figure 41 and 42 illustrate the expected particle fluxes calculated using models describing trapped electrons and protons. At high altitudes, where the satellite will spend the major part of the time, fluxes are enormous, and spectra are steep with power-law indices above four. Such an environment requires an instrument with a variable geometric factor, which would rise as the incident energy grows, adapting to the particle spectrum. To observe electrons and protons with the highest energies, the geometric factor of an instrument must provide reasonable statistics for particle fluxes of about 10^4 part/cm^2 s. At the same time, the flux of about 10^7 part/cm^2 s at low energies, below 500 keV, should increase the dead time of the instrument insignificantly.

To meet the requirements and achieve the scientific objectives, REPE combines

two technologies used in RADMON and PATE and applies the lessons learned from the RADMON mission. It has three silicon detectors arranged as two layers in front of an LYSO (Lutetium-yttrium oxyorthosilicate, $\mathrm{Lu}_{2-x}\mathrm{Y}_x\mathrm{Si}\,\mathrm{O}_5(\mathrm{Ce});\ x = 0.1...0.2$) scintillation crystal and a layer on the back of the crystal. Figure 43 illustrates how the detector stack is composed. The nominal energy range for the presented stack is 400 – 8000 keV for electrons and 6 – 100 MeV for protons.

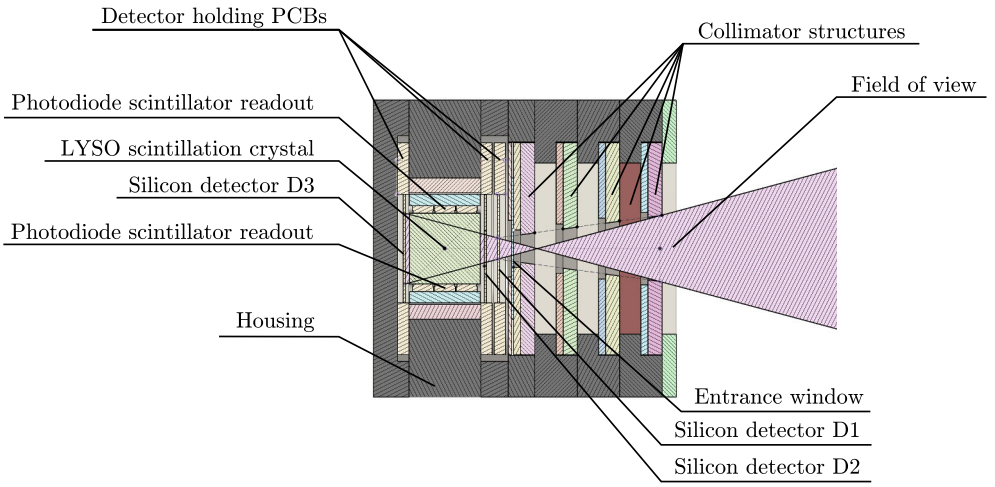

Figure 43. A sketch of the REPE detector stack and the collimator structures. Engineering graphics: Pasi Virtanen.

One of the lessons learned from RADMON is that the brass collimator allowed particles to enter the detector stack at significant incident angles if the incident energy is high enough to go through a couple of millimeters of brass. The energy deposited in an edge of the brass collimator could not be accurately accounted for, which resulted in widened response functions for the top proton energy channels. REPE has solid collimator walls without a shortcut to the detectors. The conical opening should prevent a particle incident outside the aperture from penetrating the detector stack unless the incident energy is above 150–200 MeV.

Another improvement is that the silicon detectors D1 and D2 will be a ΔE–E pair for the particles with the lowest energy unable to penetrate further into the scintillator. A silicon detector has a lower energy threshold than a scintillator, which allows the measurements of lower energy deposits characteristic to electrons. This pair has a geometric factor of somewhat below 10^{-2} cm^2 sr. The expected geometric factor may result in a count rate of about 10^5 s^{-1} in the densest regions; however, it is easier to handle such a count rate in a silicon detector than in a scintillator.

The detector plates of D1 and D2 extend to cover the entire field of view to ensure the stopping power is even for particles that hit the sensitive area of D1 or D2 and the particles going through the passive silicon in the scintillator. Thus, particles that

can reach the scintillator deposit well predictable energy in the D1 layer, even if they hit a rim of the D1 active area before they interact with the ΔE–E pair formed by D2 and the scintillator with a logical condition that D1 has a hit. The D1 condition provides active collimation for incoming particles, and the geometric factor is the same as in the previous pair. This ΔE–E pair detects particles of moderate energies, fully absorbed in the scintillator.

The last silicon detector in the stack, D3, detects high-energy protons penetrating the entire stack. A hit in D3 that coincides with a hit in the scintillator and D2 indicates that the detected proton has energy above $\sim$ 75 MeV. The penetrating protons deposit a similar amount of energy to high-energy electrons in the classical ΔE–E plane, but an electron is likely to either scatter away from the straight path or stop in the scintillator. The ability to discern protons by a hit in D3 extends the nominal energy range for protons beyond the limit of total absorption in the scintillator. Another way of extending the energy range could be a bigger crystal, but it would bring proportionally more background hits from charged particles and bremsstrahlung radiation originating from outside the aperture.

The mission requires exceptional agility of the particle measurements and a smart design of the radiation shield for the electronic circuits. In the same way as the Foresail-1, the paradigm of the Foresail-2 design is to utilize commercial off-the-shelf (COTS) electronic components in the majority of the spacecraft systems.

The usage of COTS components dramatically reduces the electronics costs but requires shielding that can reduce the ionizing dose for the electronics to the values below 300–500 Gy per six months in orbit. The obvious solution would be a thick metal vault that would itself weigh more than the CubeSat standard allows. To keep the mass within a reasonable margin, a smart solution is to be found. The Geant4 simulation software allows an arbitrary number of virtual sensitive detectors, which enables the plotting of a 2D map of the total ionizing dose for each PCB inside a particular radiation shield.

REPE has a compact detector stack confined in a thick aluminum collimator, which also acts as a shield that protects the electronics. Figure 44 shows a result of the ongoing work on the optimization of the radiation shielding for a PCB located right under the detector stack. The dark spot on the dose map originates from the detector assembly that absorbs most incident particles. The remaining dose is collected from the particles incident from the hemisphere opposite the location of the detector assembly.

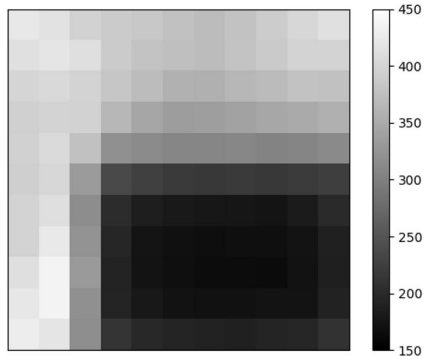

Figure 44. A map of the total ionizing dose distribution for one of the PCBs of REPE. The dose is in Grays for six months in orbit. The PCB size is 86 $\times$ 86 mm^2. The PCB is divided to 121 cells in the simulation.

List of References

Aab, A., Abreu, P., Aglietta, M., Al Samarai, I., Albuquerque, I. F. M., Allekotte, I., Almela, A., Alvarez Castillo, J., Alvarez-Muñiz, J., Anastasi, G. A., and et al. (2017). Observation of a large-scale anisotropy in the arrival directions of cosmic rays above 8×10^{18} eV. *Science*, 357(6357):1266–1270.

Ackermann, M., Ajello, M., Allafort, A., Baldini, L., Ballet, J., Barbiellini, G., Baring, M. G., Bastieri, D., Bechtol, K., Bellazzini, R., and et al. (2013). Detection of the characteristic pion-decay signature in supernova remnants. *Science*, 339(6121):807–811.

Agostinelli, S., Allison, J., Amako, K., Apostolakis, J., Araujo, H., Arce, P., Asai, M., Axen, D., Banerjee, S., Barrand, G., Behner, F., Bellagamba, L., Boudreau, J., Broglia, L., Brunengo, A., Burkhardt, H., Chauvie, S., Chuma, J., Chytracek, R., Cooperman, G., Cosmo, G., Degtyarenko, P., Dell'Acqua, A., Depaola, G., Dietrich, D., Enami, R., Feliciello, A., Ferguson, C., Fesefeldt, H., Folger, G., Foppiano, F., Forti, A., Garelli, S., Giani, S., Giannitrapani, R., Gibin, D., Cadenas, J. G., González, I., Abril, G. G., Greeniaus, G., Greiner, W., Grichine, V., Grossheim, A., Guatelli, S., Gumplinger, P., Hamatsu, R., Hashimoto, K., Hasui, H., Heikkinen, A., Howard, A., Ivanchenko, V., Johnson, A., Jones, F., Kallenbach, J., Kanaya, N., Kawabata, M., Kawabata, Y., Kawaguti, M., Kelner, S., Kent, P., Kimura, A., Kodama, T., Kokoulin, R., Kossov, M., Kurashige, H., Lamanna, E., Lampén, T., Lara, V., Lefebure, V., Lei, F., Liendl, M., Lockman, W., Longo, F., Magni, S., Maire, M., Medernach, E., Minamimoto, K., de Freitas, P. M., Morita, Y., Murakami, K., Nagamatu, M., Nartallo, R., Nieminen, P., Nishimura, T., Ohtsubo, K., Okamura, M., O'Neale, S., Oohata, Y., Paech, K., Perl, J., Pfeiffer, A., Pia, M., Ranjard, F., Rybin, A., Sadilov, S., Salvo, E. D., Santin, G., Sasaki, T., Savvas, N., Sawada, Y., Scherer, S., Sei, S., Sirotenko, V., Smith, D., Starkov, N., Stoecker, H., Sulkimo, J., Takahata, M., Tanaka, S., Tcherniaev, E., Tehrani, E. S., Tropeano, M., Truscott, P., Uno, H., Urban, L., Urban, P., Verderi, M., Walkden, A., Wander, W., Weber, H., Wellisch, J., Wenaus, T., Williams, D., Wright, D., Yamada, T., Yoshida, H., and Zschiesche, D. (2003). Geant4 – a simulation toolkit. *Nuclear Instruments and Methods in Physics Research Section A: Accelerators, Spectrometers, Detectors and Associated Equipment*, 506(3):250 – 303.

Allison, J., Amako, K., Apostolakis, J., Araujo, H., Arce Dubois, P., Asai, M., Barrand, G., Capra, R., Chauvie, S., Chytracek, R., Cirrone, G. A. P., Cooperman, G., Cosmo, G., Cuttone, G., Daquino, G. G., Donszelmann, M., Dressel, M., Folger, G., Foppiano, F., Generowicz, J., Grichine, V., Guatelli, S., Gumplinger, P., Heikkinen, A., Hrivnacova, I., Howard, A., Incerti, S., Ivanchenko, V., Johnson, T., Jones, F., Koi, T., Kokoulin, R., Kossov, M., Kurashige, H., Lara, V., Larsson, S., Lei, F., Link, O., Longo, F., Maire, M., Mantero, A., Mascialino, B., McLaren, I., Mendez Lorenzo, P., Minamimoto, K., Murakami, K., Nieminen, P., Pandola, L., Parlati, S., Peralta, L., Perl, J., Pfeiffer, A., Pia, M. G., Ribon, A., Rodrigues, P., Russo, G., Sadilov, S., Santin, G., Sasaki, T., Smith, D., Starkov, N., Tanaka, S., Tcherniaev, E., Tome, B., Trindade, A., Truscott, P., Urban, L., Verderi, M., Walkden, A., Wellisch, J. P., Williams, D. C., Wright, D., and Yoshida, H. (2006). Geant4 developments and applications. *IEEE Transactions on Nuclear Science*, 53(1):270–278.

Allison, J., Amako, K., Apostolakis, J., Arce, P., Asai, M., Aso, T., Bagli, E., Bagulya, A., Banerjee, S., Barrand, G., Beck, B., Bogdanov, A., Brandt, D., Brown, J., Burkhardt, H., Canal, P., Cano-Ott, D., Chauvie, S., Cho, K., Cirrone, G., Cooperman, G., Cortés-Giraldo, M., Cosmo, G., Cuttone,

G., Depaola, G., Desorgher, L., Dong, X., Dotti, A., Elvira, V., Folger, G., Francis, Z., Galoyan, A., Garnier, L., Gayer, M., Genser, K., Grichine, V., Guatelli, S., Guèye, P., Gumplinger, P., Howard, A., Hřivnáčová, I., Hwang, S., Incerti, S., Ivanchenko, A., Ivanchenko, V., Jones, F., Jun, S., Kaitaniemi, P., Karakatsanis, N., Karamitros, M., Kelsey, M., Kimura, A., Koi, T., Kurashige, H., Lechner, A., Lee, S., Longo, F., Maire, M., Mancusi, D., Mantero, A., Mendoza, E., Morgan, B., Murakami, K., Nikitina, T., Pandola, L., Paprocki, P., Perl, J., Petrović, I., Pia, M., Pokorski, W., Quesada, J., Raine, M., Reis, M., Ribon, A., Fira, A. R., Romano, F., Russo, G., Santin, G., Sasaki, T., Sawkey, D., Shin, J., Strakovsky, I., Taborda, A., Tanaka, S., Tomé, B., Toshito, T., Tran, H., Truscott, P., Urban, L., Uzhinsky, V., Verbeke, J., Verderi, M., Wendt, B., Wenzel, H., Wright, D., Wright, D., Yamashita, T., Yarba, J., and Yoshida, H. (2016). Recent developments in Geant4. *Nuclear Instruments and Methods in Physics Research Section A: Accelerators, Spectrometers, Detectors and Associated Equipment*, 835:186 – 225.

Altman, N. S. (1992). An introduction to kernel and nearest-neighbor nonparametric regression. *The American Statistician*, 46(3):175–185.

Anderson, P., Rich, F., and Borisov, S. (2018). Mapping the South Atlantic Anomaly continuously over 27 years. *Journal of Atmospheric and Solar-Terrestrial Physics*, 177:237–246.

Andersson, B., Gustafson, G., and Nilsson-Almqvist, B. (1987). A model for low-pT hadronic reactions with generalizations to hadron-nucleus and nucleus-nucleus collisions. *Nuclear Physics B*, 281(1-2):289–309.

Apostolakis, J., Asai, M., Bogdanov, A., Burkhardt, H., Cosmo, G., Elles, S., Folger, G., Grichine, V., Gumplinger, P., Heikkinen, A., and et al. (2009a). Geometry and physics of the Geant4 toolkit for high and medium energy applications. *Radiation Physics and Chemistry*, 78(10):859–873.

Apostolakis, J., Folger, G., Grichine, V., Heikkinen, A., Howard, A., Ivanchenko, V., Kaitaniemi, P., Koi, T., Kosov, M., Quesada, J. M., Ribon, A., Uzhinskiy, V., and Wright, D. (2009b). Progress in hadronic physics modelling in Geant4. *Journal of Physics: Conference Series*, 160:012073.

Asikainen, T. (2019). New Homogeneous Composite Of Energetic Electron Fluxes From POES: 2. Intercalibration of SEM-1 and SEM-2. *Journal of Geophysical Research: Space Physics*, 124(7):5761–5782.

Asikainen, T. and Mursula, K. (2011). Recalibration of the long-term NOAA/MEPED energetic proton measurements. *Journal of Atmospheric and Solar-Terrestrial Physics*, 73(2-3):335–347.

Attix, F. H. (1987). *Introduction to Radiological Physics and Radiation Dosimetry*. John Wiley & Sons, Inc.

Avdeichikov, V., Fomichev, A., Jakobsson, B., Rodin, A., and Ter-Akopian, G. (2000). Range–energy relation, range straggling and response function of CsI(Tl), BGO and GSO(Ce) scintillators for light ions. *Nuclear Instruments and Methods in Physics Research Section A: Accelerators, Spectrometers, Detectors and Associated Equipment*, 439(1):158–166.

Baker, D. (1998). What is space weather? *Advances in Space Research*, 22(1):7–16.

Baker, D. N., Erickson, P. J., Fennell, J. F., Foster, J. C., Jaynes, A. N., and Verronen, P. T. (2018). Space Weather Effects in the Earth's Radiation Belts. *Space Science Reviews*, 214(1).

Baker, D. N., Kanekal, S. G., Hoxie, V. C., Batiste, S., Bolton, M., Li, X., Elkington, S. R., Monk, S., Reukauf, R., Steg, S., and et al. (2013). The Relativistic Electron-Proton Telescope (REPT) Instrument on Board the Radiation Belt Storm Probes (RBSP) Spacecraft: Characterization of Earth's Radiation Belt High-Energy Particle Populations. *Space Science Reviews*, 179(1-4):337–381.

Bashkin, S., Carlson, R. R., Douglas, R. A., and Jacobs, J. A. (1958). Response of CsI (T1) Crystals to Energetic Particles. *Phys. Rev.*, 109:434–436.

Benrachi, F., Chambon, B., Cheynis, B., Drain, D., Pastor, C., Seghier, D., Zaid, K., Giorni, A., Heuer, D., Llères, A., Morand, C., Stassi, P., and Viano, J. (1989). Investigation of the performance of CsI(Tl) for charged particle identification by pulse-shape analysis. *Nuclear Instruments and Methods in Physics Research Section A: Accelerators, Spectrometers, Detectors and Associated Equipment*, 281(1):137 – 142.

Berger, M., Hubbell, J., Seltzer, S., Chang, J., Coursey, J., Sukumar, R., Zucker, D., and Olsen, K. (2010). NIST Standard Reference Database 8 (XGAM). https://www.nist.gov/pml/xcom-photon-cross-sections-database.

Berger, M. J. (1992). ESTAR, PSTAR, and ASTAR: Computer programs for calculating stopping-power and range tables for electrons, protons, and helium ions. Technical report, National Institute of Standards and Technology (NIST), Physics Laboratory (now Physical Measurement Laboratory (PML)).

Berger, M. J., Inokuti, M., Andersen, H. H., Bichsel, H., Powers, D., Seltzer, S. . M., Thwaites, D. ., and Watt, D. E. (1993). ICRU Report 49. *Journal of the International Commission on Radiation Units and Measurements*, os25(2):1.

Birks, J. B. (1964). The Scintillation Process in Alkali Halide Crystals. *IEEE Trans. Nucl. Sci.*, 11(3):4–11.

Borovsky, J. E. and Valdivia, J. A. (2018). The Earth's Magnetosphere: A Systems Science Overview and Assessment. *Surveys in Geophysics*, 39(5):817–859.

Campello, R. J. G. B., Moulavi, D., and Sander, J. (2013). *Density-Based Clustering Based on Hierarchical Density Estimates*, page 160–172. Lecture Notes in Computer Science.

Chytracek, R., Mccormick, J., Pokorski, W., and Santin, G. (2006). Geometry description markup language for physics simulation and analysis applications. *IEEE Transactions on Nuclear Science*, 53(5):2892–2896.

Claeys, C. and Simoen, E. (2002). *Radiation Effects in Advanced Semiconductor Materials and Devices*. Springer-Verlag Berlin Heidelberg, Berlin, Heidelberg, 1st edition.

Crew, A. B., Spence, H. E., Blake, J. B., Klumpar, D. M., Larsen, B. A., O'Brien, T. P., Driscoll, S., Handley, M., Legere, J., Longworth, S., and et al. (2016). First multipoint in situ observations of electron microbursts: Initial results from the NSF FIREBIRD II mission. *Journal of Geophysical Research: Space Physics*, 121(6):5272–5283.

Cyamukungu, M., Benck, S., Borisov, S., Gregoire, G., Cabrera, J., Bonnet, J.-L., Desoete, B., Preudrhomme, F., Semaille, C., Creve, G., and et al. (2014). The Energetic Particle Telescope (EPT) on Board PROBA-V: Description of a New Science-Class Instrument for Particle Detection in Space. *IEEE Transactions on Nuclear Science*, 61(6):3667–3681.

Desai, M. and Giacalone, J. (2016). Large gradual solar energetic particle events. *Living Reviews in Solar Physics*, 13(1).

Desai, M. I., Allegrini, F., Ebert, R. W., Ogasawara, K., Epperly, M. E., George, D. E., Christian, E. R., Kanekal, S. G., Murphy, N., Randol, B., and et al. (2019). The CubeSat Mission to Study Solar Particles. *IEEE Aerospace and Electronic Systems Magazine*, 34(4):16–28.

Dietz-Laursonn, E. (2016). Peculiarities in the Simulation of Optical Physics with Geant4. *arXiv: Instrumentation and Detectors*.

Evans, D. and Greer, M. (2004). Polar orbiting environmental satellite space experiment monitor-2: instrument descriptions and archive data documentation. NOAA Technical Memorandum version 1.3. NOAA Space Environment Center, Boulder, Colorado.

Frass, W. (2009). Lecture notes in C4: Particle Physics Major Option. Particle Detectors.

Geant4, C. (2020). Physics Reference Manual. https://geant4-userdoc.web.cern.ch/UsersGuides/PhysicsReferenceManual/fo/PhysicsReferenceManual.pdf.

Geant4, C. (downloaded in 2021). Reference physics lists. https://geant4.web.cern.ch/node/155.

Gieseler, J., Oleynik, P., Hietala, H., Vainio, R., Hedman, H.-P., Peltonen, J., Punkkinen, A., Punkkinen, R., Säntti, T., Hæggström, E., Praks, J., Niemelä, P., Riwanto, B., Jovanovic, N., and Mughal, M. R. (2020). Radiation Monitor RADMON aboard Aalto-1 CubeSat: First results. *Advances in Space Research*, 66(1):52–65.

Grassmann, H., Lorenz, E., and Moser, H.-G. (1985). Properties of CsI(TI) — Renaissance of an old scintillation material. *Nucl. Instruments Methods Phys. Res. Sect. A Accel. Spectrometers, Detect. Assoc. Equip.*, 228(2-3):323–326.

Greenwood, J. (2002). The correct and incorrect generation of a cosine distribution of scattered particles for Monte-Carlo modelling of vacuum systems. *Vacuum*, 67(2):217 – 222.

Gwin, R. and Murray, R. (1963). Scintillation process in CsI(Tl). 2. Emission spectra and possible role of self-trapped holes. *Physical Review*, 131(2):508+.

Hamada, M., Costa, F., Pereira, M., and Kubota, S. (2001). Dependence of scintillation characteristics in the CsI(Tl) crystal on Tl^+ concentrations under electron and alpha particles excitations. *IEEE Transactions on Nuclear Science*, 48(4):1148–1153.

Heynderickx, D., Quaghebeur, B., Wera, J., Daly, E. J., and Evans, H. D. R. (2004). New radiation environment and effects models in the European Space Agency's Space Environment Information System (SPENVIS). *Space Weather*, 2(10).

Holl, I., Lorenz, E., and Mageras, G. (1988). A measurement of the light yield of common inorganic scintillators. *IEEE Transactions on Nuclear Science*, 35(1):105–109.

Horn, D., Ball, G., Galindo-Uribarri, A., Hagberg, E., Walker, R., Laforest, R., and Pouliot, J. (1992). The mass dependence of CsI(Tl) scintillation response to heavy ions. *Nucl. Instruments Methods Phys. Res. Sect. A Accel. Spectrometers, Detect. Assoc. Equip.*, 320(1-2):273–276.

Huovelin, J., Vainio, R., Lehtolainen, A., Kilpua, E., Korpela, S., Esko, E., Muinonen, K., Bunce, E., Martindale, A., Grande, M., Andersson, H., Nenonen, S., Lehti, J., Schmidt, W., Genzer, M., Vihavainen, T., Saari, J., Peltonen, J., Valtonen, E., Talvioja, M., Portin, P., Narendranath, S., Järvinen, R., Okada, T., Milillo, A., Laurenza, M., Heino, E., and Oleynik, P. (2020). Solar Intensity X-Ray and Particle Spectrometer SIXS: Instrument Design and First Results. *Space Science Reviews*, 216(5):1–42.

Jackson, J. D. (1998). *Classical Electrodynamics*. John Wiley & Sons, Inc., Hoboken, New Jersey, USA, 3 edition.

Johnson, A. T., Shumko, M., Griffith, B., Klumpar, D. M., Sample, J., Springer, L., Leh, N., Spence, H. E., Smith, S., Crew, A., and et al. (2020). The FIREBIRD-II CubeSat mission: Focused investigations of relativistic electron burst intensity, range, and dynamics. *Review of Scientific Instruments*, 91(3):034503.

Kanekal, S. G., Blum, L., Christian, E. R., Crum, G., Desai, M., Dumonthier, J., Evans, A., Greeley, A. D., Guerro, S., Livi, S., and et al. (2019). The MERiT Onboard the CeREs: A Novel Instrument to Study Energetic Particles in the Earth's Radiation Belts. *Journal of Geophysical Research: Space Physics*, 124(7):5734–5760.

Kestilä, A., Tikka, T., Peitso, P., Rantanen, J., Näsilä, A., Nordling, K., Saari, H., Vainio, R., Janhunen, P., Praks, J., and Hallikainen, M. (2013). Aalto-1 nanosatellite – technical description and mission objectives. *Geosci. Instrumentation, Methods Data Syst.*

Koba, Y., Iwamoto, H., Kiyohara, K., Nagasaki, T., Wakabayashi, G., Uozumi, Y., and Matsufuji, N. (2011). Scintillation efficiency of inorganic scintillators for intermediate-energy charged particles. *Progress in NUCLEAR SCIENCE and TECHNOLOGY. Proceedings of the Fifth International Symposium on Radiation Safety and Detection Technology (ISORD-5)*, 1(1):218–221.

Kurnosova, L., Kolobyanina, T., Logachev, V., Razorenov, L., Sirotkin, I., and Fradkin, M. (1962). Discovery of radiation anomalies above the South Atlantic at heights of 310–340 km. *Planetary and Space Science*, 9(8):513–516.

Lanzerotti, L. J. (2017). Space Weather: Historical and Contemporary Perspectives. *Space Science Reviews*, 212(3-4):1253–1270.

Leroy, C. and Rancoita, P.-G. (2012). *Silicon Solid State Devices And Radiation Detection*. World Scientific Publishing Company, Singapore.

Levenberg, K. (1944). A method for the solution of certain non-linear problems in least squares. *Quarterly of Applied Mathematics*, 2(2):164–168.

Li, W. and Hudson, M. (2019). Earth's Van Allen Radiation Belts: From Discovery to the Van Allen Probes Era. *Journal of Geophysical Research: Space Physics*, 124(11):8319–8351.

Liddle, J. D., Holt, A. P., Jason, S. J., O'Donnell, K. A., and Stevens, E. J. (2020). Space science with CubeSats and nanosatellites. *Nature Astronomy*, 4(11):1026–1030.

Marquardt, D. W. (1963). An algorithm for least-squares estimation of nonlinear parameters. *Journal of the Society for Industrial and Applied Mathematics*, 11(2):431–441.

McIlwain, C. E. (1961). Coordinates for mapping the distribution of magnetically trapped particles. *Journal of Geophysical Research (1896-1977)*, 66(11):3681–3691.

McInnes, L., Healy, J., and Astels, S. (2017). hdbscan: Hierarchical density based clustering. *The Journal of Open Source Software*, 2(11).

Mewaldt, R. A., Leske, R. A., Stone, E. C., Barghouty, A. F., Labrador, A. W., Cohen, C. M. S., Cummings, A. C., Davis, A. J., von Rosenvinge, T. T., and Wiedenbeck, M. E. (2009). STEREO Observations of Energetic Neutral Hydrogen Atoms During the 2006 December 5 Solar Flare. *Astrophysical Journal Letters*, 693:L11–L15.

Milbrath, B., Peurrung, A., Bliss, M., and Weber, W. (2008). Radiation detector materials: An overview. *Journal of Materials Research*, 23(10):2561–2581.

Millan, R. M., Von Steiger, R., Ariel, M., Bartalev, S., Borgeaud, M., Campagnola, S., Castillo-Rogez, J. C., Fléron, R., Gass, V., Gregorio, A., and et al. (2019). Small satellites for space science. *Advances in Space Research*, 64(8):1466–1517.

Moszynski, M., Syntfeld-Kazuch, A., Swiderski, L., Sibczynski, P., Grodzicka, M., Szczesniak, T., Gektin, A. V., Schotanus, P., Shiran, N., Williams, R. T., and et al. (2016). Energy Resolution and Slow Components in Undoped CsI Crystals. *IEEE Transactions on Nuclear Science*, 63(2):459–466.

Mughal, M. R., Praks, J., Vainio, R., Janhunen, P., Envall, J., Näsilä, A., Oleynik, P., Niemelä, P., Slavinskis, A., Gieseler, J., Jovanovic, N., Riwanto, B., Toivanen, P., Leppinen, H., Tikka, T., Punkkinen, A., Punkkinen, R., Hedman, H.-P., Lill, J.-O., and Slotte, J. (2021). "Aalto-1, multi-payload CubeSat: In-orbit results and lessons learned". *Acta Astronautica*, 187:557–568.

Murray, R. B. and Meyer, A. (1961). Scintillation response of activated inorganic crystals to various charged particles. *Physical Review*, 122(3):815–826.

Ni, B., Shprits, Y., Hartinger, M., Angelopoulos, V., Gu, X., and Larson, D. (2011). Analysis of radiation belt energetic electron phase space density using THEMIS SST measurements: Cross-satellite calibration and a case study. *Journal of Geophysical Research: Atmospheres*, 116(A3):n/a–n/a.

Oleynik, P., Vainio, R., Hedman, H.-P., Punkkinen, A., Punkkinen, R., Salomaa, L., Säntti, T., Tuominen, J., Virtanen, P., Bosser, A., Janhunen, P., Kilpua, E., Palmroth, M., Praks, J., Slavinskis, A., Kakakhel, S. R., Peltonen, J., Plosila, J., Tammi, J., Tenhunen, H., and Westerlund, T. (2020). Particle Telescope aboard FORESAIL-1: simulated performance. *Advances in Space Research*, 66(1):29–41.

Oleynik, P., Vainio, R., Punkkinen, A., Dudnik, O., Gieseler, J., Hedman, H., Hietala, H., Hæggström, E., Niemelä, P., Peltonen, J., Praks, J., Punkkinen, R., Säntti, T., and Valtonen, E. (2020). Calibration of RADMON Radiation Monitor Onboard Aalto-1 CubeSat. *Advances in Space Research*, 66(1):42–51.

Owens, A. and Peacock, A. (2004). Compound semiconductor radiation detectors. *Nuclear Instruments and Methods in Physics Research Section A: Accelerators, Spectrometers, Detectors and Associated Equipment*, 531(1-2):18–37.

Palmroth, M., Praks, J., Vainio, R., Janhunen, P., Kilpua, E. K. J., Afanasiev, A., Ala-Lahti, M., Alho, A., Asikainen, T., Asvestari, E., Battarbee, M., Binios, A., Bosser, A., Brito, T., Dubart, M., Envall, J., Ganse, U., Ganushkina, N. Y., George, H., Gieseler, J., Good, S., Grandin, M., Haslam, S., Hedman, H.-P., Hietala, H., Jovanovic, N., Kakakhel, S., Kalliokoski, M., Kettunen, V. V., Koskela, T., Lumme, E., Meskanen, M., Morosan, D., Mughal, M. R., Niemelä, P., Nyman, S., Oleynik, P., Osmane, A., Palmerio, E., Peltonen, J., Pfau-Kempf, Y., Plosila, J., Polkko, J., Poluianov, S., Pomoell, J., Price, D., Punkkinen, A., Punkkinen, R., Riwanto, B., Salomaa, L., Slavinskis, A., Säntti, T., Tammi, J., Tenhunen, H., Toivanen, P., Tuominen, J., Turc, L., Valtonen, E., Virtanen, P., and Westerlund, T. (2019). FORESAIL-1 CubeSat Mission to Measure Radiation Belt Losses and Demonstrate Deorbiting. *Journal of Geophysical Research: Space Physics*, 124(7):5783–5799.

Papini, P., Grimani, C., and Stephens, S. A. (1996). An estimate of the secondary-proton spectrum at small atmospheric depths. *Il Nuovo Cimento C*, 19(3):367–387.

Peltonen, J., Hedman, H.-P., Ilmanen, A., Lindroos, M., Määttänen, M., Pesonen, J., Punkkinen, R., Punkkinen, A., Vainio, R., Valtonen, E., Säntti, T., Pentikäinen, J., and Hæggström, E. (2014). Electronics for the RADMON instrument on the Aalto-1 student satellite. In *10th Eur. Work. Microelectron. Educ. EWME 2014*.

Poghosyan, A. and Golkar, A. (2017). CubeSat evolution: Analyzing CubeSat capabilities for conducting science missions. *Progress in Aerospace Sciences*, 88:59–83.

Praks, J., Mughal, M. R., Vainio, R., Janhunen, P., Envall, J., Oleynik, P., Näsilä, A., Leppinen, H., Niemelä, P., Slavinskis, A., Gieseler, J., Toivanen, P., Tikka, T., Peltola, T., Bosser, A., Schwarzkopf, G., Jovanovic, N., Riwanto, B., Kestilä, A., Punkkinen, A., Punkkinen, R., Hedman, H.-P., Säntti, T., Lill, J.-O., Slotte, J., Kettunen, H., and Virtanen, A. (2021). Aalto-1, multi-payload cubesat: Design, integration and launch. *Acta Astronautica*, 187:370–383.

Prinzie, J., Steyaert, M., and Leroux, P. (2018). *Radiation Effects in CMOS Technology*, page 1–20. Analog Circuits and Signal Processing.

Reames, D. V. (1999). Particle Acceleration at the Sun and in the Heliosphere. *Space Science Reviews*, 90(3/4):413–491.

Reames, D. V. (2015). What Are the Sources of Solar Energetic Particles? Element Abundances and Source Plasma Temperatures. *Space Science Reviews*, 194(1-4):303–327.

Reeves, G. D., Mcadams, K. L., Friedel, R. H. W., and O'Brien, T. P. (2003). Acceleration and loss of relativistic electrons during geomagnetic storms. *Geophysical Research Letters*, 30(10):n/a–n/a.

Ripoll, J., Claudepierre, S. G., Ukhorskiy, A. Y., Colpitts, C., Li, X., Fennell, J. F., and Crabtree, C. (2020). Particle Dynamics in the Earth's Radiation Belts: Review of Current Research and Open Questions. *Journal of Geophysical Research: Space Physics*, 125(5).

Rothwell, P. and McIlwain, C. E. (1960). Magnetic storms and the Van Allen radiation belts—Observations from satellite 1958-Epsilon (Explorer IV). *Journal of Geophysical Research (1896-1977)*, 65(3):799–806.

Santin, G., Ivanchenko, V., Evans, H., Nieminen, P., and Daly, E. (2005). GRAS: a general-purpose 3-D Modular Simulation tool for space environment effects analysis. *IEEE Transactions on Nuclear Science*, 52(6):2294–2299.

Schiller, Q., Gerhardt, D., Blum, L., Li, X., and Palo, S. (2014). *Design and scientific return of a miniaturized particle telescope onboard the Colorado Student Space Weather Experiment (CSSWE) CubeSat*, pages 1–14. IEEE.

Schotanus, P. and Kamermans, R. (1990). Scintillation characteristics of pure and Tl-doped CsI crystals. *IEEE Transactions on Nuclear Science*, 37(2):177–182.

Selesnick, R. S. (2015). Measurement of inner radiation belt electrons with kinetic energy above 1 MeV. *Journal of Geophysical Research: Space Physics*, 120(10):8339–8349.

Selesnick, R. S. and Albert, J. M. (2019). Variability of the proton radiation belt. *Journal of Geophysical Research: Space Physics*, 124(7):5516–5527.

Selesnick, R. S., Looper, M. D., and Mewaldt, R. A. (2007). A theoretical model of the inner proton radiation belt. *Space Weather*, 5(4):n/a–n/a.

Seltzer, S. M. and Berger, M. J. (1982). Evaluation of the collision stopping power of elements and compounds for electrons and positrons. *The International Journal of Applied Radiation and Isotopes*, 33(11):1189–1218.

Seppälä, A., Clilverd, M. A., Beharrell, M. J., Rodger, C. J., Verronen, P. T., Andersson, M. E., and Newnham, D. A. (2015). Substorm-induced energetic electron precipitation: Impact on atmospheric chemistry. *Geophysical Research Letters*, 42(19):8172–8176.

Shepherd, S. G. (2014). Altitude-adjusted corrected geomagnetic coordinates: Definition and functional approximations. *Journal of Geophysical Research: Space Physics*, 119(9):7501–7521.

Singer, S. F. (1958). "Radiation Belt" and Trapped Cosmic-Ray Albedo. *Physical Review Letters*, 1(5):171–173.

Snyder, C. W. (1959). The Upper Boundary of the Van Allen Radiation Belts. *Nature*, 184(4684):439–440.

Sullivan, J. (1971). Geometric factor and directional response of single and multi-element particle telescopes. *Nuclear Instruments and Methods*, 95(1):5–11.

Thébault, E., Finlay, C. C., Beggan, C. D., Alken, P., Aubert, J., Barrois, O., Bertrand, F., Bondar, T., Boness, A., Brocco, L., and et al. (2015). International geomagnetic reference field: the 12th generation. *Earth, Planets and Space*, 67(1).

Tretyak, V. (2010). Semi-empirical calculation of quenching factors for ions in scintillators. *Astroparticle Physics*, 33(1):40–53.

Turunen, E., Kero, A., Verronen, P. T., Miyoshi, Y., Oyama, S.-I., and Saito, S. (2016). Mesospheric ozone destruction by high-energy electron precipitation associated with pulsating aurora. *Journal of Geophysical Research: Atmospheres*, 121(19):11, 852–11, 861.

Vainio, R., Desorgher, L., Heynderickx, D., Storini, M., Flückiger, E., Horne, R. B., Kovaltsov, G. A., Kudela, K., Laurenza, M., Mckenna-Lawlor, S., and et al. (2009). Dynamics of the Earth's Particle Radiation Environment. *Space Science Reviews*, 147(3-4):187–231.

Vainio, R., Gieseler, J., Alho, A., Bosser, A., Envall, J., Grandin, M., Haslam, S., Hedman, H.-P., Janhunen, P., Jovanovic, N., Kakakhel, S. R. U., Kilpua, E., Mughal, M. R., Niemelä, P., Nyman, S., Oleynik, P., Palmroth, M., Peltonen, J., Plosila, J., Praks, J., Punkkinen, A., Punkkinen, R., Riwanto, B., Salomaa, L., Säntti, T., Tammi, J., Tenhunen, H., Toivanen, P., Tuominen, J., Virtanen, P., and Westerlund, T. (2019). FORESAIL-1: Energetic particle and de-orbiting experiments with a CubeSat. In *EGU General Assembly Conference Abstracts*, EGU General Assembly Conference Abstracts, page 9892.

Valtonen, E., Peltonen, J., Dudnik, O. V., Kudin, A. M., Andersson, H., Borodenko, Y. A., Eronen, T., Huovelin, J., Kettunen, H., Kurbatov, E. V., and et al. (2009). Radiation Tolerance Tests of Small-Sized CsI(Tl) Scintillators Coupled to Photodiodes. *IEEE Transactions on Nuclear Science*, 56(4):2149–2154.

Vampola, A. (1998). *Measurement Techniques in Space Plasmas: Particles*, chapter Measuring Energetic Electrons – What Works and What Doesn't. American Geophysical Union (AGU), USA.

Van Allen, J. A. (1958). Observation of high intensity radiation by satellites 1958 alpha and gamma. *Journal of Jet Propulsion*, 28(9):588–592.

Van Allen, J. A., Baker, D. N., Randall, B. A., and Sentman, D. D. (1974). The magnetosphere of Jupiter as observed with Pioneer 10: 1. Instrument and principal findings. *Journal of Geophysical Research (1896-1977)*, 79(25):3559–3577.

Vernov, S. N. and Chudakov, A. E. (1960). Reviews of Topical Problems: Investigations of Cosmic Radiation and of the Terrestrial Corpuscular Radiation by Means of Rockets and Satellites. *Soviet Physics Uspekhi*, 3(2):230–250.

Weimer, D. R., Bowman, B. R., Sutton, E. K., and Tobiska, W. K. (2011). Predicting global average thermospheric temperature changes resulting from auroral heating. *Journal of Geophysical Research: Atmospheres*, 116(A1):n/a–n/a.

Yando, K., Millan, R. M., Green, J. C., and Evans, D. S. (2011). A Monte Carlo simulation of the NOAA POES Medium Energy Proton and Electron Detector instrument. *Journal of Geophysical Research: Atmospheres*, 116(A10):1–13.

TURUN
YLIOPISTO
UNIVERSITY
OF TURKU

Painosalama Oy, Turku, Finland 2021

ISBN 978-951-29-8704-7 (PRINT)
ISBN 978-951-29-8705-4 (PDF)
ISSN 0082-7002 (PRINT)
ISSN 2343-3175 (ONLINE)